The Dynamics of Atmospheric Blocking Across a Hierarchy of Climate Models

A Thesis Submitted in Partial Fulfilment of the Requirements for the Degree of Doctor of Philosophy in

Sustainable Development and Climate Change

Doctoral Programme of National Interest

In the Curriculum
EARTH SYSTEM AND ENVIRONMENT

by

Michele Filippucci

Supervisor: Prof. Simona Bordoni

Co-Supervisor: Prof. Stephen Thomson

February, 2026

ABSTRACT

Atmospheric blocking is a persistent disruption of the westerly progression of weather systems and often leads to prolonged temperature and precipitation extremes, such as summer heatwaves and heavy winter snowfall. Understanding the mechanisms that lead to atmospheric blocking, and accurately representing its frequency and characteristics in climate models, is crucial for assessing its future evolution under climate change. To this aim, we carried three research projects that address the study of blocking from different but complementary perspectives, reported in this Thesis in the form of research articles.

In the first research article, we investigate how a state-of-the-art climate model, EC-Earth, represents atmospheric blocking. We focus on the role of stochastic parameterizations and assess whether introducing stochastic schemes can improve the climatological frequency of blocking. We find small detrimental effects of the stochastic scheme on blocking representation and link this outcome to modifications of tropical cloud water content.

The second study focuses on Greenland blocking using reanalysis datasets and CMIP6 future projections. Given the observed increase in Greenland blocking in recent decades—and its important implications for continental ice melt—we examine whether this trend is driven by internal climate variability or by a forced response to global warming. We analyze Greenland blocking characteristics using a newly developed Lagrangian tracking algorithm. We find that blocking originating to the west of Greenland, which we name 'upstream blocks', are responsible for the recent blocking increase and that their internal variability is under-represented in CMIP6 models.

In the third research article, we design an idealized modeling experiment to explore how blocking responds to an Arctic amplification-like forcing. We conduct simulations in both zonally symmetric and asymmetric configurations and interpret the resulting changes in blocking frequency using the emerging Traffic Jam theory of blocking onset. Blocking uniformly increases in the symmetric simulations, whereas the maximum in blocking frequency is displaced upstream under Arctic amplification in the asymmetric experiment. By providing a physically consistent explanation of these changes, our results highlight the importance of mean circulation features, such as a localized storm track, in shaping the response of blocking to external forcing.

Overall, this Thesis adopts a hierarchy of modeling approaches to advance our understanding of atmospheric blocking. The results provide new insights into the

mechanisms controlling blocking onset, introduce novel methodologies based on recent theoretical advancements, highlight directions for future model development, and shed light on regional and global projections of future blocking frequency.

ACKNOWLEDGEMENTS

First of all, my deepest thanks go to Simona Bordoni, who has been my PhD supervisor during these three years at the University of Trento. I am deeply grateful for her support, both for the many scientific discussions and for her commitment to creating a working environment that fostered learning, exchange, and curiosity for research.

I would also like to thank Stephen Thomson, co-supervisor of my PhD, who kindly agreed to host me at the University of Exeter for my visiting period abroad. Thanks to him, I felt welcomed at Exeter. He respected and supported my needs during a period that, for personal reasons, was not easy. Moreover, Stephen greatly helped me develop the ideas behind the fourth Chapter of this Thesis and introduced me to Neil Lewis, to whom I am also sincerely grateful for the many scientific discussions and for his technical support in using the ISCA model.

I also thank Paolo Davini, my Master's thesis supervisor, who kindly continued collaborating with me during my first years of PhD and helped shape the second Chapter of this Thesis.

At the same time, I thank all my colleagues in Trento for the 11 a.m. and 4 p.m. coffee breaks, for the countless discussions and exchanges, and for the lessons on Alpine meteorology that I will carry with me after the PhD. I also thank the colleagues I met at conferences. In particular, I thank Jacob Maddison, who I met at a conference in Colorado, reconnected in Exeter, and who became co-author of the third Chapter of this Thesis. I also thank Andrea and Giada, who began this journey with me, even though in Turin – travel companions and partners in our first experiences presenting our work at international conferences.

I am also grateful to IUSS Pavia and the PHD-SDC team, who made this national doctoral experience possible. Thanks to this inter-university and interdisciplinary initiative, I was able to broaden my perspective on climate change and engage with researchers from different institutions and backgrounds.

I thank my family for supporting me throughout these PhD years, both in my travels and in my numerous house moving, making me feel I always had a place—a home—to go back to. I also thank the friends I found in Trento, both inside and outside the University. Over these years we have shared so much, and it is also thanks to them that I found in Trento a fertile place to work and grow. Finally, a big thanks go to Gio, with whom I have shared both the hardest and happiest moments of these past years, and who has always encouraged me to keep going with her contagious enthusiasm.

Table of Contents

List of Figures

List of Tables

Chapter 1

Introduction and thesis outline

1 INTRODUCTION AND THESIS OUTLINE

Weather extremes are among the most impactful, discussed, and studied features of Earth's climate. These events can lead to severe consequences for human health and infrastructure, frequently manifesting as compound events [1] that involve concurrent temperature, precipitation, and wind extremes.

Understanding how weather extremes will change with global warming is a critical area of research, both because of their significant economic and societal impacts and because of their role in shaping public opinion on mitigation policies. For instance, extreme events, such as heatwaves, have been shown to shift risk perception, ultimately influencing societal views on climate change policies [2, 3].

Consequently, improving our understanding of future extreme event trends and accurately attributing drivers of observed severe weather events remains a central outstanding research challenge. A more robust understanding can inform policymakers and the public, raise awareness about climate change impacts, and foster the implementation of effective adaptation strategies.

To illustrate the expected future evolution of extremes, it is informative to use temperature anomalies as a starting point to describe how the full temperature distribution might change in a warming climate. Temperature provides a natural starting point, as it is a fundamental thermodynamic variable and a key mediator of other atmospheric extremes.

While there is broad consensus that anthropogenic climate change will lead to an increase in global temperature, whether future extremes will correspond to larger or smaller deviations from the future mean—i.e. whether the variance of the temperature distribution will increase or decrease—remains a subject of active debate. Several complementary approaches have been proposed to quantify these changes on a global scale and to provide theoretical frameworks for their evolution. For instance, Schneider *et al.* [4] proposed that temperature variance in the midlatitudes scales linearly with the meridional potential temperature gradient, based on the argument that synoptic temperature variability is primarily generated by advection by synoptic-scale eddies. However, as the authors themselves acknowledge, this approximation can lead to relative errors of up to 10%. Additionally, changes in the meridional gradient of temperature with global warming remain uncertain [5, 6]. Moreover, Tamarin-Brodsky *et al.* [7] underscored the importance of changes of temperature distribution skewness alongside changes of variance to assess changes in future temperature extremes. Using a different perspective, Zhang & Boos [8] provides a constraint on the maximum temperature during a heatwave

based on convective instability arguments, but they do not provide insights into the frequency of heatwaves.

Temperature extremes are not only important in their own right, but they also provide a framework for estimating changes in precipitation and wind extremes. Given that these variables are coupled through fundamental thermodynamic and dynamical constraints, changes in the temperature distribution can be used to infer shifts in other hydrometeorological extremes. Specifically, according to the Clausius–Clapeyron relationship, a warmer atmosphere retains more moisture, potentially leading to more intense precipitation [9, e.g.]. More recently, analogous scaling arguments have been used to link increases in atmospheric moisture to stronger wind extremes in the midlatitudes [10].

Despite the appeal of these fundamental physics–based arguments, reasoning exclusively at the global scale can be incomplete. Observations show that the impacts of global warming strongly depend on location [11, 12]. This spatial heterogeneity points to the importance of regional dynamical processes that modulate how large-scale thermodynamic changes translate into local extremes. In this context, atmospheric blocking stands out as a large-scale yet regional phenomenon that acts as a primary driver of regional extremes in the Northern Hemisphere (NH) midlatitudes [13, 14]. Atmospheric blocking is the central focus of this thesis.

Atmospheric blocking consists of a persistent obstruction of the westerly progression of weather patterns in the midlatitudes [15]. While it occurs in both hemispheres, it is significantly more frequent in NH [16]. By diverting the zonal flow and disrupting synoptic weather systems, atmospheric blocking leads to quasi-stationary weather conditions, which cause prolonged positive or negative temperature extremes due to meridional air mass advection from low or high latitudes or to persistent radiative heating [17, e.g.].

Due to its regional and nonlinear nature, atmospheric blocking challenges the assumption of linearity central to most global theories of temperature variance trends, emerging as a key atmospheric feature shaping the tails of the temperature distribution. The nonlinear role of blocking arises from its dual nature: it is both a consequence of the mean atmospheric state and a driver of regional climate anomalies. While atmospheric blocking occurs on synoptic time scales (5–20 days), its frequency has a profound impact on the climate of vast regions, such as Greenland, Europe, the Bering Strait, the Urals, and North America [16–18]. At the same time, blocking arises in regions where the atmospheric mean state exhibits specific characteristics, most notably on the poleward flank of the jet stream and at the exit regions of the North Atlantic and North Pacific storm tracks, for reasons that will be clarified in the next sections. It follows that blocking acts both as a driver of temperature extremes in regions with specific mean-state characteristics and as a dynamic regime that, in turn, nonlinearly shapes the regional climate.

In the next sections, we further describe the phenomenology of atmospheric blocking, beginning with a review of observational evidence and classification methods in the existing literature (Section 1.1). We continue by describing several approaches used to quantitatively measure blocking frequency in climate datasets

(Section 1.2). Next, we present modern theories for blocking onset and maintenance (Section 1.3), and discuss the ability of current climate models to accurately represent its dynamics and assess future changes (Section 1.4). Ultimately, in Section 1.5, we identify the main research gaps that this thesis aims to address and outline how the collection of articles that make up this work addresses these issues by investigating novel research questions.

1.1 PHENOMENOLOGY OF ATMOSPHERIC BLOCKING

Before introducing the several definitions and the multifaceted impacts of atmospheric blocking, it is instructive to briefly review the history of its observations and classification methods.

Although atmospheric blocking was initially considered a phenomenon with limited and straightforward characteristics, its complex nature was increasingly recognized over time. The first investigations of atmospheric blocking date back to the beginning of the 20th century (e.g., Garriott [19]), when it was described as a prolonged interruption of the westerly progression of synoptic eddies, leading to extreme weather over Europe and the United States. Quantitative analyses began in the late 1940s, when the phenomenon was referred to as *blocking action* [20, 21] and the first theoretical explanations for its onset were proposed [15, 22]. Later, Rex [15] performed the first statistical analysis of blocking characteristics across a large set of events, identifying common features such as a disruption of the midlatitude westerlies associated with a large ridge folding over a cyclonic anomaly. These circulation features result in a splitting of the jet stream, which flows predominantly in the zonal direction upstream of the block and in the meridional direction downstream of it. Subsequently, Sumner [23] further classified midlatitude blocks into two main types: *diffluent blocks*, similar to those described by Rex [15], and *meridional blocks*, in which winds become predominantly meridional both upstream and downstream of the blocking anticyclone.

In the following decades, the scientific community did not converge on a unique definition of blocking, but instead adopted multiple blocking classes, broadly consistent with those introduced by Sumner [23]. These categories can be naturally illustrated within the potential vorticity (PV) framework, which effectively describes blocking dynamics through the evolution and interaction of conserved PV anomalies. A common feature among blocking systems is the presence of a persistent negative PV anomaly that is advected poleward, diverting the flow and inducing an anticyclonic circulation anomaly. In the simplest—albeit perhaps the most controversial—case, atmospheric blocking can form as a quasi-stationary Rossby wave with a near-zero phase speed, referred to as a *ridge block*. These patterns develop mainly in summer, and the debate on whether they should be classified as true blocking events remains open. An *omega block* arises when the negative PV anomaly reaches higher latitudes, assumes an elongated shape, and develops a locally isolated PV minimum. This class of blocks is named after the shape of the PV contours, which resembles the Greek capital letter Ω, and it corresponds to the

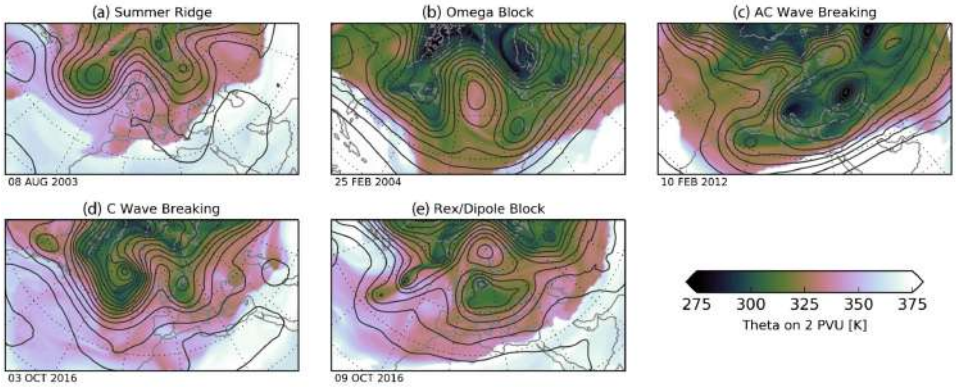

Figure 1.1: Figure adapted from Woollings* et al. *[17]. Examples of North Atlantic blocks. Snapshots of (colour shading) potential temperature θ on the dynamical tropopause (PV = 2 PVU) and (contour lines) geopotential height at 500 hPa (contour spacing 60 m) for the dates indicated. Data is from ERA-Interim.

meridional blocks identified by Sumner [23]. Other configurations involve Rossby wave breaking, in which negative PV anomalies fold cyclonically (anticlockwise) or anticyclonically (clockwise) over regions of higher PV, reversing the meridional PV gradient for several days. These correspond to the blocking systems described by Rex [15] and are therefore referred to as *Rex blocks*.

While early observations of blocking were mainly confined to Europe and the United States, this classification applies to phenomena occurring across different locations. Ridge blocks typically occur at low-to-mid latitudes, whereas Omega and Rex blocks preferentially occur at mid-to-high latitudes, reaching regions such as the Bering Strait and Greenland, often in association with Rossby wave breaking. Moreover, blocking occurs more frequently in the Northern Hemisphere than in the Southern Hemisphere, because of the larger continental area and stronger zonal asymmetries in surface temperature [16, e.g.]. Fig. 1.1 shows examples of the different blocking types, adapted from Woollings *et al.* [17].

As mentioned previously, atmospheric blocking is associated with severe temperature extremes and compound extremes. Within the anticyclonic anomaly, high surface pressure conditions can develop, favoring clear-sky conditions that enhance radiative heating in summer and promote the formation of temperature inversions in winter [15, 24, 25, e.g.]. In cases involving Rossby wave breaking, cold air masses and moisture are advected along the trough structure, resulting in cold spells and anomalous precipitation within the cyclonic anomaly [25, 26, e.g.]. Depending on the season, these conditions can produce persistent and intense heatwaves in summer or severe snowstorms in winter [27–29, e.g.]. Such events cause severe damage in densely populated regions and can also lead to extraordinary summer ice melt at high latitudes, with significant impacts on the mass balance of the Greenland Ice Sheet [30].

1.2 BLOCKING DETECTION

In order to study blocking, the scientific community has developed over time several *blocking indices*, that is, tools used to detect atmospheric blocking in atmospheric datasets and to analyze its climatological characteristics. The diversity of blocking definitions has led to a corresponding variety of detection algorithms in gridded climate datasets, each better suited to identifying a specific family of blocks. These indices are based on different physical variables, such as potential temperature [31], potential vorticity [32], or geopotential height [16, 33]. They are usually evaluated in the mid-to-high troposphere to capture large-scale synoptic weather systems in the free atmosphere. The indices can be further classified into departure indices and absolute indices, which are illustrated below.

On the one hand, departure indices identify blocking by computing anomalies of a given field—such as potential vorticity at the dynamical tropopause or geopotential height at 500 hPa—relative to their climatological mean. These indices detect features that satisfy predefined criteria such as a significant deviation from the mean, a minimum persistence, or a minimum spatial extent. An example is the index introduced by Dole & Gordon [33], who identify blocking systems by detecting persistent anomalous deviations in the 500-hPa geopotential height field. These indices are better suited for detecting omega or ridge blocks.

On the other hand, absolute indices aim to identify blocking directly from instantaneous snapshots of two-dimensional fields by searching for specific flow configurations. For example, Tibaldi & Molteni [34] analyzes the 500 hPa geopotential height field to identify Rossby wave breaking structures characterized by a reversal of the meridional geopotential height gradient around a central latitude. Davini *et al.* [16] later extends this index to other latitudes, providing a two-dimensional climatology of blocking particularly suited for Rex blocks.

A non-exhaustive list of other existing indices includes those introduced by Pelly & Hoskins [35] and later refined by Berrisford *et al.* [36] and Masato *et al.* [31], who identify blocking through reversals of the westerly flow by analyzing potential temperature at the dynamical tropopause. Schwierz *et al.* [32], in turn, detects blocking by identifying persistent negative anomalies in the column-averaged potential vorticity field. Other methods are hybrid, combining different detection approaches in order to reach a compromise that balances their respective strengths and limitations. An example is the index proposed by Dunn-Sigouin & Son [37], which combines elements of both Tibaldi & Molteni [34] and Dole & Gordon [33]. More recently, Barpanda & Nakamura [38] analyzed the Local Wave Activity (LWA) field—a physical quantity measuring jet stream waviness discussed in the next Section—to identify atmospheric blocking as persistent, long-lasting large-amplitude meanders of the jet stream as captured by significant LWA anomalies.

A conceptually different approach is based on weather regimes, which apply cluster analysis to meteorological fields such as the 500-hPa geopotential height, first introduced by Legras [39]. Atmospheric blocking emerges naturally as one

of the dominant weather regimes, together with other flow configurations. For instance, North Atlantic weather regimes are characterized by both phases of the North Atlantic Oscillation (NAO), the Azores ridge and Scandinavian blocking. While this method does not require the use of arbitrary thresholds, its main limitation is its inability to identify the precise location of blocking onset. Therefore, it can only be used to compute blocking frequencies over predefined geographical regions.

A climatology of NH blocking obtained using two different methods, namely the Davini (DAV) index [16], and the Geopotential Height Anomaly (GHA) index [17], similar to the method used by Dole & Gordon [33], is shown in Fig. 4.4. Panels (a) and (b) report blocking frequency during June, July, and August (JJA), while panels (c) and (d) show blocking frequency during December, January, and February (DJF). Although atmospheric blocking occurs throughout the year, both indices consistently capture a seasonal poleward shift of blocking activity. In winter, blocking maxima are located over Northern Europe, Greenland, and the Bering Strait, with secondary maxima over the western United States and the Urals. In summer, the distribution changes substantially. This is particularly evident for the GHA index, which shows a maximum developing over northern Siberia and a marked reduction of blocking frequency in the Atlantic sector. Similar seasonal characteristics are also found for the DAV index.

To summarize, atmospheric blocking is a multifaceted phenomenon, characterized by multiple definitions and a wide range of manifestations. Recent literature has increasingly acknowledged this diversity, emphasizing the need for its implications when conducting new research. We conclude this section by quoting a recent review on atmospheric blocking [17], which provides a compelling perspective on the utility of maintaining multiple detection indices:

"This diversity should be viewed as an opportunity rather than a limitation, since each approach provides different but complementary aspects of the same phenomenon. In this sense, the exploitation of an array of blocking indices is perhaps wiser than the search for a definitive blocking definition."

1.3 THEORIES OF BLOCKING ONSET AND MAINTENANCE

As systematic classifications provided a more robust characterization of blocking, research shifted toward elucidating the dynamical mechanisms responsible for its formation and maintenance. We begin by reviewing early seminal ideas that have shaped today's understanding of blocking, before progressing to modern, more comprehensive theories.

Initial conceptualizations on blocking dynamics arose from the observation that blocking frequency is highest near the ridges of midlatitude stationary waves. Consequently, blocking was originally interpreted as an amplification of pre-existing stationary waves. Both linear resonance mechanisms [40], involving resonance between stationary waves and Rossby waves with near-zero phase speed, and nonlinear mechanisms, which account for higher-order terms in the barotropic potential

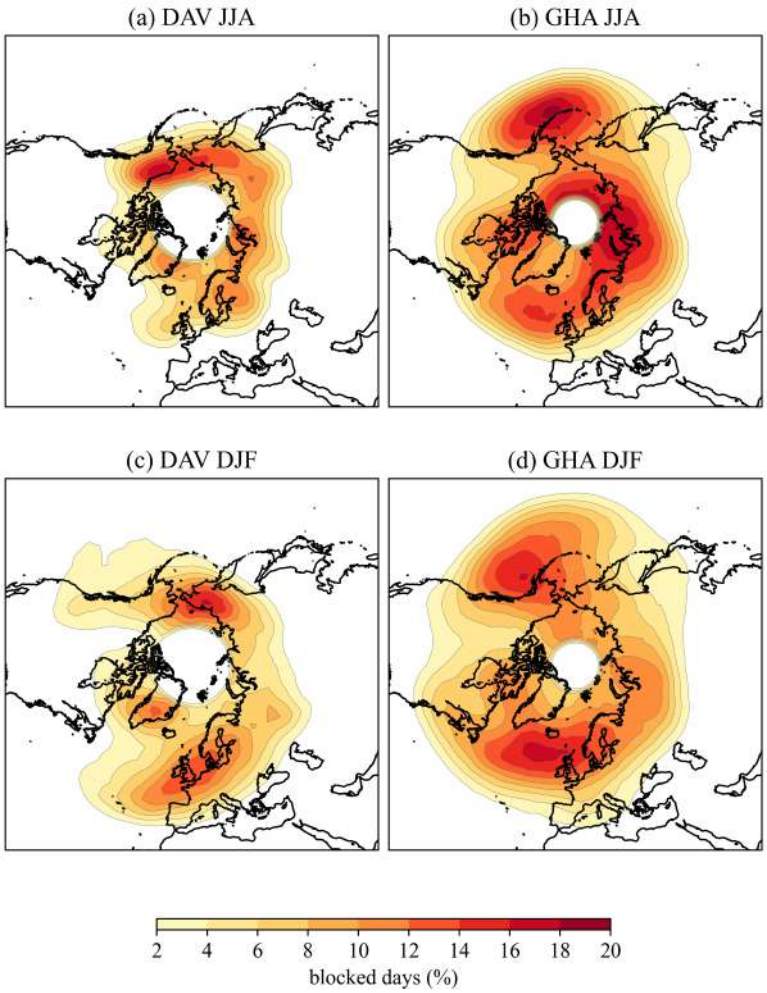

Figure 1.2: Northern Hemisphere blocking frequency, expressed as the percentage of days per season. Panels a and b show the summer (June, July and August) climatology, while panels c and d show the winter (December, January and February) climatology. Results are based on two indices: the DAV index (a,c) and the GHA index (b,d). See the main text for additional details.

vorticity equation [41], were investigated. However, these early theories proved too simplistic and failed to accurately describe blocking in more realistic atmospheric configurations.

Since orography is an important driver of midlatitude stationary waves [42], its role in blocking onset was also extensively examined, leading to one of the most influential early theories: the multiple equilibrium hypothesis. Charney & DeVore [43] showed that in a barotropic model with idealized sinusoidal orography, the atmospheric circulation exhibits two distinct regimes: a *zonal flow* regime and a

blocked flow regime. This finding suggested that blocking could be interpreted as a separate atmospheric regime associated with multiple equilibria of the flow. However, subsequent developments in general circulation models (GCMs) with higher resolution demonstrated that this result is largely an artifact of strong spectral truncation and is not reproduced in more realistic, higher-resolution models [44, 45].

During the same period, alternative theoretical interpretations emerged, including the description of blocking as solitary waves solutions of the quasi-geostrophic PV equation. Modons, introduced by McWilliams [46], are exact solutions that resemble Rex-type blocks. Despite their conceptual appeal, these solutions require unrealistically strong westerlies that are not observed in the real atmosphere and therefore lack empirical support. Similarly, Rizzoli [47] proposed soliton solutions, but convincing observational evidence for such structures has not been found.

With the rise of comprehensive and higher-resolution numerical weather prediction and climate models, attention shifted toward the interaction between synoptic-scale eddies and the large-scale flow. Early insights into this interaction were provided by Berggren *et al.* [22], who showed that transient eddies approaching a blocking anticyclone tend to shrink. Later, Green [48] suggested that the advection of eddies into the center of the anticyclone contributes to blocking maintenance, analyzing a specific event from 1976. These ideas were formalized by Shutts [49] through the eddy-straining mechanism: as synoptic eddies encounter a large-scale ridge, they are stretched meridionally, triggering an inverse energy cascade toward lower wavenumbers that reinforces the block against dissipation. Around the same time, Hoskins *et al.* [50] introduced the E-vector formalism, demonstrating that the elongation of upstream synoptic eddies leads to downstream deceleration of the jet, further supporting the eddy-straining mechanism.

Building on these insights, subsequent studies emphasized the role of large-scale circulation in blocking onset. Pelly & Hoskins [35] analyzed blocking at the dynamical tropopause and linked it to Rossby wave breaking. More generally, the potential vorticity framework [51, 52] provides a clear interpretation of blocking as the poleward extrusion of low-PV subtropical air. At higher latitudes, nonlinear terms of the quasi-geostrophic PV equation gain importance due to reduced meridional wind shear and increased Coriolis effects, leading to Rossby wave breaking. This mechanism is closely related to the eddy-straining process described by Shutts [49]. Within this framework, several studies Benedict *et al.* [53], Franzke *et al.* [54], and Woollings *et al.* [55] argued that phenomena such as Greenland blocking and the NAO can be understood as different manifestations of Rossby wave breaking.

More recently, a novel description of blocking onset has emerged based on the concept of *Local Wave Activity* (LWA) [56]. LWA is a measure of the jet stream's waviness derived directly from the PV field. In this framework, blocking is interpreted as a persistent local accumulation of LWA that obstructs the normal westerly progression of weather patterns and generates temperature anomalies [57]. This model is also known as the Traffic Jam theory, in analogy with Richards [58] model for highway congestion. In their seminal work, Nakamura & Huang [57] de-

fine a flow-dependent carrying capacity, which reaches a minimum downstream of the Pacific and North Atlantic storm tracks. When this capacity is exceeded, blocking onset occurs. The carrying capacity itself depends on mean flow characteristics, such as the position of stationary wave crests and the mean zonal wind. This framework provides a physically consistent explanation for why blocking preferentially occurs in stationary wave crest regions, and why atmospheric blocking frequency increases or decreases in response to weakening or strengthening midlatitude zonal winds. It also forms a core element of one of the research articles underlying this thesis and will be discussed in detail in the following chapters.

While recent literature represents substantial progress toward a comprehensive theory of the blocking life cycle, these modern frameworks require further validation through observational and modeling studies before they are universally adopted. This represents a double challenge: neither the theoretical understanding of blocking, spanning its onset, maintenance and decay, nor its representation in climate models is yet fully satisfying.

1.4 Blocking representation in climate models and future projections

Atmospheric blocking remains one of the most challenging features of the atmospheric circulation to represent in climate models, primarily due to its highly nonlinear nature. This long-standing model deficiency is a matter of considerable concern, as the accurate projection of blocking changes in a warming climate is crucial for assessing future weather extremes. Across several generations of climate models, systematic biases in blocking representation have been documented, with particularly pronouced biases over the Euro-Atlantic sector [17, 18, 59, 60].

Davini & d'Andrea [60] evaluated the evolution of these biases from the third to the sixth phase of the Coupled Model Intercomparison Project (CMIP) [61–63], noting that while newer generations show improvement, they do not yet fully capture blocking climatology. Specifically, in winter, they found a substantial reduction in biases over the Pacific sector, near-zero biases in Greenland blocking, and a large but reduced bias over Europe. In summer, despite noticeable improvements, larger biases remain, particularly over the Northern Pacific and North Eurasia. In some regions, biases still reach 30–40% relative error in terms of blocked-day frequency. While Davini & d'Andrea [60] used an absolute index for their analysis, Schiemann *et al.* [64] corroborated these findings using a departure index.

Recent generations of CMIP models feature improved physics parameterizations, higher horizontal and vertical atmospheric resolution, increased ocean model resolution, and numerous other refinements. However, determining which of these factors contributes most to improved blocking representation remains a subject of ongoing research, as it likely involves a complex interplay of factors. Schiemann *et al.* [64] specifically investigated the impact of increased resolution using the HighResMIP/PRIMAVERA simulations [65], which follow a CMIP-like protocol

but at higher resolution. They found that higher horizontal resolution leads to further improvement relative to the CMIP6 ensemble, consistent with earlier studies [66, 67]. However, the benefits of increased resolution appear to be region- and season-dependent, with larger improvements over the North Atlantic than the Pacific [68]. Similarly, Davini *et al.* [69] found that apparent improvements from higher resolution in EC-Earth can sometimes arise from compensating errors rather than improved physical representation.

Beyond horizontal resolution, enhanced vertical resolution is critical for better capturing the sharp potential vorticity gradients and atmospheric dynamics near the tropopause [70]. Additionally, the fidelity of ocean dynamics also plays a crucial role: reducing sea surface temperature biases and accurately simulating the path of the Gulf Stream are essential for a correct representation of the North Atlantic storm track and subsequent blocking climatology [71, 72]. More broadly, a faithful representation of the atmospheric mean state, particularly the position and strength of the jet stream, substantially reduces blocking biases [71]. Finally, recent studies have emphasized the role of moist processes, specifically the latent heat release and associated diabatic heating involved in blocking onset and amplification [73]. Accurate representation of moist dynamics, both at the resolved large scales and at the sub-grid scale parameterizations is therefore essential for advancing blocking modeling [74]. Improving blocking representation thus requires coordinated progress across multiple model components.

Despite these persistent challenges, robust signals regarding future blocking trends are emerging from climate projections. Davini & d'Andrea [60] show that the vast majority of models simulate a decrease in blocking frequency in both winter and summer, with notable exceptions for summer blocking over the Urals and winter blocking over western North America. Notably, models with smaller climatological biases tend to project larger decreases [60], a trend confirmed by studies using different indices [75, 76].

The physical drivers of these changes include projected shifts in the upper-level jet stream's strength and position [60]. Earlier studies suggested that accelerated NH polar warming could weaken midlatitude winds and make them more *wavy*, potentially enhancing blocking [77]. However, subsequent work has shown that these results are highly sensitive to the choice of metric [78, 79] and on the observational period considered [80]. Moreover, a tug-of-war exists between polar surface warming, which reduces the meridional temperature gradient, and near-equatorial upper-tropospheric warming, which increases it through enhanced latent heat release and moist adiabatic adjustment. Recent modeling and observational studies suggest that the latter mechanism dominates, strengthening upper-tropospheric winds [6, 81, 82] and reducing blocking frequency [60, 75], although the summer response remains more complex [6, 83, 84].

Atmospheric moisture is another important driver, as latent heat release in blocking centers can amplify the associated anticyclonic anomalies [73]. Steinfeld *et al.* [85] further highlight that increasing atmospheric moisture under global warming, following Clausius–Clapeyron scaling [4], may enhance both the size

and intensity of blocking events.

While most studies focus on hemispheric trends, regional analyses paint a multifaceted picture. For example, Greenland blocking has increased markedly over the past decade [30, 86], yet current climate models fail to reproduce this observed variability in either historical or future simulations [87, 88]. Additionally, the rising frequency of summer heatwaves in recent decades [89, 90] may be linked to increased stationarity of Rossby waves and blocking dynamics, though the causality behind this connection remains under investigation [91].

In summary, while multi-model studies suggest a general reduction in NH blocking, especially in winter [60, 75, 76], the regional and seasonal response is more complex, underscoring the need for further investigations.

1.5 THESIS OUTLINE AND RESEARCH AREAS

As described in the previous sections, the characterization, understanding, and modeling of atmospheric blocking have advanced substantially over the past half-century. Nevertheless, significant research gaps persist, as emphasized above, limiting our ability to provide robust assessments of blocking trends in a warming climate. This thesis consists of three research articles that address several of these outstanding questions. The knowledge gaps addressed here can be broadly categorized into three areas:

1. improving the representation of blocking in state-of-the-art climate models;
2. adopting a rigorous and effective theoretical framework for the analysis and interpretation of blocking;
3. identifying regional and global atmospheric blocking trends under anthropogenic global warming.

We will return to these categories in the Conclusions, where we discuss in detail how each is addressed in this work. The papers are hereafter presented in chronological order, reflecting the evolution of the research carried out, followed by a brief description of each study.

The first project, presented in Chapter 2, addresses blocking representation in the state-of-the-art EC-Earth climate model. Using the Climate SPHINX ensemble—a set of experiments featuring a range of different atmospheric horizontal resolutions—we assess the impact of two stochastic schemes on the model's ability to simulate blocking. While increasing resolution can improve blocking representation, the high computational cost often necessitates a trade-off between grid spacing and other priorities, such as ensemble size or the complexity of integrated Earth system components (e.g., cryosphere, vegetation). In this context, stochastic parameterizations offer a computationally efficient alternative by accounting for sub-grid scale variability without the need for resolving it explicitly in the model's dynamical core. Our study focuses on two specific schemes: Stochastically Perturbed

Parameterization Tendencies (SPPT) and Stochastic Kinetic Energy Backscatter (SKEB). The SKEB scheme reintroduces energy dissipated at sub-grid scales into the synoptic-scale flow by perturbing the large-scale streamfunction. SPPT, which typically exerts a more pronounced influence on the model output, perturbs the deterministic tendencies of temperature, specific humidity, and wind fields to represent unresolved sub-grid variability. This paper therefore contributes to ongoing efforts to improve climate model representation of atmospheric blocking and informs future model development. The article has already been published on Weather and Climate Dynamics.

The second project, reported in Chapter 3, investigates regional blocking trends over the last two decades. Summer Greenland blocking has increased since 2010 [30] at an unprecedented pace, with signs of decline after 2020 [87, 92]. While this trend may partially reflect internal variability, current climate models, including HIGHRESMIP [93], ECMWF seasonal forecasts [94], and CMIP6 simulations [87], fail to reproduce the observed variability. Our study provides new insights by analyzing this increase using an original Lagrangian tracking algorithm, the *blocktrack* tool [95]. Using ERA5 reanalysis data [96], we classify blocking trajectories into *upstream* and *retrograding* events, originating over northern Canada and the eastern North Atlantic, respectively [97, cf.]. We evaluate the characteristics of these events, including the moisture transport involved in blocking amplification and the temperature anomalies in the blocking high. By applying the same framework to a large ensemble of CMIP6 models, evaluate both the simulated historical internal variability and future projections. This work highlights regional and seasonal trends, identifying dynamical mechanisms that may significantly influence blocking frequency in a warmer world. The paper has been submitted for peer review on International Journal of Climatology.

The third project, presented in Chapter 4, examines the relationship between circulation changes driven by Arctic amplification, jet stream waviness, and blocking activity using the Traffic Jam theory [57]. Although previous studies have addressed individual responses to Arctic amplification, such as shifts in zonal jets and variations in transient kinetic energy, few provide a physically consistent framework that directly links changes in meridional temperature gradients to blocking changes. To address this gap, we designed a suite of idealized experiments using the ISCA modeling framework to compute the flow carrying capacity following the Traffic Jam theory and investigate how polar warming influences blocking onset. Our modeling approach includes zonally symmetric aquaplanet simulations, and simulations in which zonal asymmetries are introduced by prescribing an idealized localized midlatitude storm track. This study serves a dual purpose: (i) to clarify the processes by which Arctic amplification affects atmospheric blocking, and (ii) to test the diagnostic utility of the Traffic Jam theory in linking changes in blocking frequency to mean state variations. Our results suggest that this framework provides a robust physical basis for understanding blocking onset, supporting its wider adoption in climate change studies.. This work is currently being prepared for submission to a peer-reviewed journal.

Finally, in Chapter 5, we provide an overall summary, highlighting our most important results, placing them within the broader context of atmospheric blocking representation in climate models and future projections, and connecting our work back to the research gaps enumerated at the beginning of this Introduction.

REFERENCES

1. Zscheischler, J. *et al.* A typology of compound weather and climate events. *Nature reviews earth & environment* **1,** 333–347 (2020).
2. Konisky, D. M. *et al.* Extreme weather events and climate change concern. *Climatic change* **134,** 533–547. doi:https://doi.org/10.1007/s10584-015-1555-3 (2016).
3. Zanocco, C. *et al.* Comparing public and scientific extreme event attribution to climate change. *Climatic Change* **177,** 76. doi:https://doi.org/10.1007/s10584-024-03735-0 (2024).
4. Schneider, T. *et al.* Physics of changes in synoptic midlatitude temperature variability. *Journal of Climate* **28,** 2312–2331. doi:https://doi.org/10.1175/JCLI-D-14-00632.1 (2015).
5. Cohen, J. *et al.* Divergent consensuses on Arctic amplification influence on midlatitude severe winter weather. *Nature Climate Change* **10,** 20–29. doi:https://doi.org/10.1038/s41558-019-0662-y (2020).
6. Shaw, T. A. *et al.* Emerging climate change signals in atmospheric circulation. *AGU Advances* **5,** e2024AV001297. doi:https://doi.org/10.1029/2024AV001297 (2024).
7. Tamarin-Brodsky, T. *et al.* Changes in Northern Hemisphere temperature variability shaped by regional warming patterns. *Nature Geoscience* **13,** 414–421. doi:https://doi.org/10.1038/s41561-020-0576-3 (2020).
8. Zhang, Y. & Boos, W. R. An upper bound for extreme temperatures over midlatitude land. *Proceedings of the National Academy of Sciences* **120,** e2215278120. doi:https://doi.org/10.1073/pnas.2215278120 (2023).
9. Schneider, T. *et al.* Water vapor and the dynamics of climate changes. *Reviews of Geophysics* **48.** doi:https://doi.org/10.1029/2009RG000302 (2010).
10. Shaw, T. A. & Miyawaki, O. Fast upper-level jet stream winds get faster under climate change. *Nature Climate Change* **14,** 61–67. doi:https://doi.org/10.1038/s41558-023-01884-1 (2024).
11. IPCC. *Climate Change 2023: Synthesis Report. Contribution of Working Groups I, II and III to the Sixth Assessment Report of the Intergovernmental Panel on Climate Change* (eds Lee, H. & Romero, J.) 35–115. doi:10.59327/IPCC/AR6-9789291691647 (IPCC, Geneva, Switzerland, 2023).

12. Shaw, T. A. *et al.* Regional climate change: consensus, discrepancies, and ways forward. *Frontiers in climate* **6,** 1391634. doi:https://doi.org/10.3389/fclim.2024.1391634 (2024).

13. Pfahl, S. & Wernli, H. Quantifying the relevance of atmospheric blocking for co-located temperature extremes in the Northern Hemisphere on (sub-) daily time scales. *Geophysical Research Letters* **39.** doi:https://doi.org/10.1029/2012GL052261 (2012).

14. Jiménez-Esteve, B. & Domeisen, D. I. The role of atmospheric dynamics and large-scale topography in driving heatwaves. *Quarterly Journal of the Royal Meteorological Society* **148,** 2344–2367. doi:https://doi.org/10.1002/qj.4306 (2022).

15. Rex, D. F. Blocking action in the middle troposphere and its effect upon regional climate. *Tellus* **2,** 275–301. doi:https://doi.org/10.3402/tellusa.v2i4.8603 (1950).

16. Davini, P. *et al.* Bidimensional Diagnostics, Variability, and Trends of Northern Hemisphere Blocking. *Journal of Climate* **25,** 6496–6509. doi:10.1175/JCLI-D-12-00032.1 (19 Oct. 2012).

17. Woollings, T. *et al.* Blocking and its Response to Climate Change. *Current Climate Change Reports* **4,** 287–300. doi:10.1007/s40641-018-0108-z (3 2018).

18. Masato, G. *et al.* Wave-breaking characteristics of Northern Hemisphere winter blocking: A two-dimensional approach. *Journal of climate* **26,** 4535–4549. doi:https://doi.org/10.1175/JCLI-D-12-00240.1 (2013).

19. Garriott, E. B. *Long-range weather forecasts* **35** (US Government Printing Office, 1904).

20. Namias, J. Characteristics of the general circulation over the Northern Hemisphere during the abnormal winter 1946–47. *Monthly weather review* **75,** 145–152 (1947).

21. Elliott, R. D. & Smith, T. B. A study of the effects of large blocking highs on the general circulation in the northern-hemisphere westerlies. *Journal of Atmospheric Sciences* **6,** 68–85 (1949).

22. Berggren, R. *et al.* An aerological study of zonal motion, its perturbations and break-down. *Tellus* **1,** 14–37 (1949).

23. Sumner, E. A study of blocking in the Atlantic-European of the northern hemisphere. *Quarterly Journal of the Royal Meteorological Society* **80,** 402–416 (1954).

24. Trigo, R. *et al.* Climate impact of the European winter blocking episodes from the NCEP/NCAR Reanalyses. *Climate Dynamics* **23,** 17–28 (2004).

25. Sousa, P. M. *et al.* European temperature responses to blocking and ridge regional patterns. *Climate Dynamics* **50,** 457–477. doi:https://doi.org/10.1007/s00382-017-3620-2 (2018).

26. McIntyre, M. E. & Palmer, T. Breaking planetary waves in the stratosphere. *Nature* **305,** 593–600 (1983).

27. Buehler, T. *et al.* The relationship of winter season North Atlantic blocking frequencies to extreme cold or dry spells in the ERA-40. *Tellus A: Dynamic Meteorology and Oceanography* **63,** 174–187 (2011).

28. Perkins, S. E. A review on the scientific understanding of heatwaves—Their measurement, driving mechanisms, and changes at the global scale. *Atmospheric Research* **164,** 242–267 (2015).

29. Yao, Y. *et al.* The positive North Atlantic Oscillation with downstream blocking and Middle East snowstorms: Impacts of the North Atlantic jet. *Journal of Climate* **29,** 1853–1876 (2016).

30. Hanna, E. *et al.* The influence of North Atlantic atmospheric and oceanic forcing effects on 1900–2010 Greenland summer climate and ice melt/runoff. *Int. J. Climatol* **33,** 862–880. doi:DOI:10.1002/joc.3475 (2013).

31. Masato, G. *et al.* Wave-breaking characteristics of midlatitude blocking. *Quarterly Journal of the Royal Meteorological Society* **138,** 1285–1296. doi:https://doi.org/10.1002/qj.990 (2012).

32. Schwierz, C. *et al.* Perspicacious indicators of atmospheric blocking. *Geophysical research letters* **31** (2004).

33. Dole, R. M. & Gordon, N. D. Persistent anomalies of the extratropical Northern Hemisphere wintertime circulation: Geographical distribution and regional persistence characteristics. *Monthly Weather Review* **111,** 1567–1586. doi:https://doi.org/10.1175/1520-0493(1983)111<1567:PAOTEN>2.0.CO;2 (1983).

34. Tibaldi, S. & Molteni, F. On the operational predictability of blocking. *Tellus A* **42,** 343–365. doi:10.1034/j.1600-0870.1990.t01-2-00003.x (3 1990).

35. Pelly, J. L. & Hoskins, B. J. A new perspective on blocking. *Journal of the atmospheric sciences* **60,** 743–755 (2003).

36. Berrisford, P. *et al.* Blocking and Rossby wave breaking on the dynamical tropopause in the Southern Hemisphere. *Journal of the Atmospheric Sciences* **64,** 2881–2898. doi:https://doi.org/10.1175/JAS3984.1 (2007).

37. Dunn-Sigouin, E. & Son, S.-W. Northern Hemisphere blocking frequency and duration in the CMIP5 models. *Journal of Geophysical Research: Atmospheres* **118,** 1179–1188. doi:https://doi.org/10.1002/jgrd.50143 (2013).

38. Barpanda, P. & Nakamura, N. Local wave-activity analysis of atmospheric blocks in the Northern Hemisphere winter. *Journal of Climate.* doi:https://doi.org/10.1175/JCLI-D-24-0232.1 (2025).

39. Legras, B. *Cluster analysis and weather regimes.* in *Proc. Workshop on the Nature and Prediction of Extratropical Weather Systems Vol. 2.* (1987), 123–149.

40. Tung, K. & Lindzen, R. A theory of stationary long waves. Part I: A simple theory of blocking. *Monthly Weather Review* **107,** 714–734 (1979).

41. Egger, J. Dynamics of blocking highs. *Journal of Atmospheric sciences* **35,** 1788–1801 (1978).

42. Hoskins, B. J. & Karoly, D. J. The steady linear response of a spherical atmosphere to thermal and orographic forcing. *Journal of Atmospheric Sciences* **38,** 1179–1196 (1981).

43. Charney, J. G. & DeVore, J. G. Multiple flow equilibria in the atmosphere and blocking. *Journal of the atmospheric sciences* **36,** 1205–1216 (1979).

44. Tung, K. & Rosenthal, A. Theories of multiple equilibria—A critical reexamination. Part I: Barotropic models. *J. Atmos. Sci* **42,** 2804–2819 (1985).

45. Cehelsky, P. & Tung, K. K. Theories of multiple equilibria and weather regimes—A critical reexamination. Part II: Baroclinic two-layer models. *J. Atmos. Sci* **44,** 3282–3303 (1987).

46. McWilliams, J. C. An application of equivalent modons to atmospheric blocking. *Dynamics of Atmospheres and Oceans* **5,** 43–66 (1980).

47. Rizzoli, P. M. in *Advances in Geophysics* 147–224 (Elsevier, 1982).

48. Green, J. The weather during July 1976: Some dynamical considerations of the drought. *Weather* **32,** 120–126 (1977).

49. Shutts, G. The propagation of eddies in diffluent jetstreams: Eddy vorticity forcing of 'blocking' flow fields. *Quarterly Journal of the Royal Meteorological Society* **109,** 737–761 (1983).

50. Hoskins, B. J. *et al.* The shape, propagation and mean-flow interaction of large-scale weather systems. *Journal of Atmospheric Sciences* **40,** 1595–1612 (1983).

51. Hoskins, B. J. *et al.* On the use and significance of isentropic potential vorticity maps. *Quarterly Journal of the Royal Meteorological Society* **111,** 877–946 (1985).

52. Hoskins, B. J. & Sardeshmukh, P. D. A diagnostic study of the dynamics of the northern hemisphere winter of 1985-86. *Quarterly Journal of the Royal Meteorological Society* **113,** 759–778 (1987).

53. Benedict, J. J. *et al.* Synoptic view of the North Atlantic oscillation. *Journal of the Atmospheric Sciences* **61,** 121–144. doi:https://doi.org/10.1175/1520-0469(2004)061<0121:SVOTNA>2.0.CO;2 (2004).

54. Franzke, C. *et al.* Is the North Atlantic Oscillation a breaking wave? *Journal of the atmospheric sciences* **61,** 145–160. doi:https://doi.org/10.1175/1520-0469(2004)061<0145:ITNAOA>2.0.CO;2 (2004).

55. Woollings, T. *et al.* A new Rossby wave–breaking interpretation of the North Atlantic Oscillation. *Journal of the Atmospheric Sciences* **65,** 609–626. doi:https://doi.org/10.1175/2007JAS2347.1 (2008).

56. Huang, C. S. & Nakamura, N. Local finite-amplitude wave activity as a diagnostic of anomalous weather events. *Journal of the Atmospheric Sciences* **73,** 211–229. doi:https://doi.org/10.1175/JAS-D-15-0194.1 (2016).

57. Nakamura, N. & Huang, C. S. Atmospheric blocking as a traffic jam in the jet stream. *Science* **361,** 42–47. doi:10.1126/science.aat0721 (2018).

58. Richards, P. I. Shock waves on the highway. *Operations research* **4,** 42–51. doi:https://doi.org/10.1287/opre.4.1.42 (1956).

59. Davini, P. & D'Andrea, F. Northern Hemisphere atmospheric blocking representation in global climate models: twenty years of improvements? *Journal of Climate* **29,** 8823–8840. doi:https://doi.org/10.1175/JCLI-D-16-0242.1 (2016).

60. Davini, P. & d'Andrea, F. From CMIP3 to CMIP6: Northern Hemisphere atmospheric blocking simulation in present and future climate. *Journal of Climate* **33,** 10021–10038. doi:https://doi.org/10.1175/JCLI-D-19-0862.1 (2020).

61. Meehl, G. A. *et al.* The WCRP CMIP3 multimodel dataset: A new era in climate change research. *Bulletin of the American meteorological society* **88,** 1383–1394 (2007).

62. Taylor, K. E. *et al.* An overview of CMIP5 and the experiment design. *Bulletin of the American meteorological Society* **93,** 485–498 (2012).

63. Eyring, V. *et al.* Overview of the Coupled Model Intercomparison Project Phase 6 (CMIP6) experimental design and organization. *Geoscientific Model Development* **9,** 1937–1958. doi:https://doi.org/10.5194/gmd-9-1937-2016 (2016).

64. Schiemann, R. *et al.* Northern Hemisphere blocking simulation in current climate models: evaluating progress from the Climate Model Intercomparison Project Phase 5 to 6 and sensitivity to resolution. *Weather and Climate Dynamics* **1,** 277–292. doi:https://doi.org/10.5194/wcd-1-277-2020 (2020).

65. Moreno-Chamarro, E. *et al.* Impact of increased resolution on long-standing biases in HighResMIP-PRIMAVERA climate models. *Geoscientific Model Development Discussions* **2021,** 1–33. doi:https://doi.org/10.5194/gmd-15-269-2022 (2021).

66. Matsueda, M. Blocking predictability in operational medium-range ensemble forecasts. *Sola* **5,** 113–116 (2009).

67. Berckmans, J. *et al.* Atmospheric blocking in a high resolution climate model: influences of mean state, orography and eddy forcing. *Atmospheric Science Letters* **14,** 34–40. doi:https://doi.org/10.1002/asl2.412 (2013).

68. Schiemann, R. *et al.* The resolution sensitivity of Northern Hemisphere blocking in four 25-km atmospheric global circulation models. *Journal of Climate* **30,** 337–358. doi:https://doi.org/10.1175/JCLI-D-16-0100.1 (2017).

69. Davini, P. *et al.* Improved winter European atmospheric blocking frequencies in high-resolution global climate simulations. *Journal of Advances in Modeling Earth Systems* **9,** 2615–2634. doi:https://doi.org/10.1002/2017MS001082 (2017).

70. Anstey, J. A. *et al.* Multi-model analysis of Northern Hemisphere winter blocking: Model biases and the role of resolution. *Journal of Geophysical Research: Atmospheres* **118,** 3956–3971. doi:https://doi.org/10.1002/jgrd.50231 (2013).

71. Scaife, A. A. *et al.* Improved Atlantic winter blocking in a climate model. *Geophysical Research Letters* **38.** doi:https://doi.org/10.1029/2011GL049573 (2011).

72. O'Reilly, C. H. *et al.* The influence of the Gulf Stream on wintertime European blocking. *Climate Dynamics* **47,** 1545–1567. doi:https://doi.org/10.1007/s00382-015-2919-0 (2016).

73. Pfahl, S. *et al.* Importance of latent heat release in ascending air streams for atmospheric blocking. *Nature Geoscience* **8,** 610–614. doi:https://doi.org/10.1038/ngeo2487 (2015).

74. Dolores-Tesillos, E. *et al.* On the role of moist and dry processes in atmospheric blocking biases in the Euro-Atlantic region in CMIP6. *Weather and Climate Dynamics* **6,** 471–487. doi:https://doi.org/10.5194/wcd-6-471-2025 (2025).

75. Dorrington, J. *et al.* CMIP6 models trend toward less persistent European blocking regimes in a warming climate. *Geophysical Research Letters* **49,** e2022GL100811. doi:https://doi.org/10.1029/2022GL100811 (2022).

76. Lohmann, R. *et al.* Northern Hemisphere atmospheric blocking in CMIP6 climate projections using a hybrid index. *Journal of Climate* **37,** 6605–6625. doi:https://doi.org/10.1175/JCLI-D-23-0589.1 (2024).

77. Francis, J. A. & Vavrus, S. J. Evidence linking Arctic amplification to extreme weather in mid-latitudes. *Geophysical research letters* **39.** doi:https://doi.org/10.1029/2012GL051000 (2012).

78. Barnes, E. A. Revisiting the evidence linking Arctic amplification to extreme weather in midlatitudes. *Geophysical research letters* **40,** 4734–4739. doi:https://doi.org/10.1002/grl.50880 (2013).

79. Screen, J. A. & Simmonds, I. Exploring links between Arctic amplification and mid-latitude weather. *Geophysical Research Letters* **40,** 959–964. doi:https://doi.org/10.1002/grl.50174 (2013).

80. Blackport, R. & Screen, J. A. Insignificant effect of Arctic amplification on the amplitude of midlatitude atmospheric waves. *Science Advances* **6,** eaay2880. doi:10.1126/sciadv.aay2880 (2020).

81. Woollings, T. *et al.* Trends in the atmospheric jet streams are emerging in observations and could be linked to tropical warming. *Communications Earth & Environment* **4,** 125. doi:https://doi.org/10.1038/s43247-023-00792-8 (2023).

82. Franzke, C. L. & Harnik, N. Long-term trends of the atmospheric circulation and moist static energy budget in the JRA-55 reanalysis. *Journal of Climate* **36,** 2959–2984. doi:https://doi.org/10.1175/JCLI-D-21-0724.1 (2023).

83. Chemke, R. & Coumou, D. Human influence on the recent weakening of storm tracks in boreal summer. *npj Climate and Atmospheric Science* **7,** 86. doi:https://doi.org/10.1038/s41612-024-00640-2 (2024).

84. Kang, J. M. *et al.* Anthropogenic aerosols have significantly weakened the regional summertime circulation in the Northern Hemisphere during the satellite era. *Agu Advances* **5,** e2024AV001318. doi:https://doi.org/10.1029/2024AV001318 (2024).

85. Steinfeld, D. *et al.* Response of moist and dry processes in atmospheric blocking to climate change. *Environmental Research Letters* **17,** 084020. doi:10.1088/1748-9326/ac81af (2022).

86. Hanna, E. *et al.* Greenland Blocking Index 1851–2015: a regional climate change signal. *International Journal of Climatology* **36,** 4847–4861. doi:https://doi.org/10.1002/joc.4673 (2016).

87. Maddison, J. *et al.* Missing increase in summer Greenland blocking in climate models. *Geophysical Research Letters* **51,** e2024GL108505. doi:10.1029/2024GL108505 (2024).

88. Lee, S. H. & Polvani, L. M. Increasing frequency and persistence of the summertime Greenland High regime not captured by a seasonal prediction model very large ensemble. *Geophysical Research Letters* **53,** e2025GL119421. doi:https://doi.org/10.1029/2025GL119421 (2026).

89. Teng, H. *et al.* Warming pattern over the Northern Hemisphere midlatitudes in boreal summer 1979–2020. *Journal of Climate* **35,** 3479–3494. doi:https://doi.org/10.1175/JCLI-D-21-0437.1 (2022).

90. Sun, X. *et al.* Enhanced jet stream waviness induced by suppressed tropical Pacific convection during boreal summer. *Nature Communications* **13,** 1288. doi:https://doi.org/10.1038/s41467-022-28911-7 (2022).

91. Domeisen, D. I. *et al.* Prediction and projection of heatwaves. *Nature Reviews Earth & Environment* **4,** 36–50. doi:https://doi.org/10.1038/s43017-022-00371-z (2023).

92. Preece, J. R. *et al.* Summer atmospheric circulation over Greenland in response to Arctic amplification and diminished spring snow cover. *Nature Communications* **14,** 3759. doi:https://doi.org/10.1038/s41467-023-39466-6 (2023).

93. Luu, L. N. *et al.* Greenland Teubler2023drysummer blocking characteristics: an evaluation of a high-resolution multi-model ensemble. *Climate Dynamics* **62,** 10503–10523. doi:https://doi.org/10.1007/s00382-024-07453-2 (2024).

94. Beckmann, J. *et al.* Summer Greenland Blocking in observations and in SEAS5. 1 seasonal forecasts: robust trend or natural variability? *EGUsphere* **2025,** 1–34. doi:https://doi.org/10.5194/egusphere-2024-3998 (2025).

95. Filippucci, M. *Blocktrack* 2024. doi:10.5281/zenodo.13837897.

96. Hersbach, H. *et al.* The ERA5 global reanalysis. *Quarterly Journal of the Royal Meteorological Society* **146,** 1999–2049. doi:10.1002/qj.3803 (730 July 2020).

97. Hauser, S. *et al.* Life cycle dynamics of Greenland blocking from a potential vorticity perspective. *Weather and Climate Dynamics* **5,** 633–658. doi:10.5194/wcd-5-633-2024 (2024).

Chapter 2

Impact of stochastic physics on the representation of atmospheric blocking in EC-Earth3

This chapter is extensively based on the following publication:
Filippucci M., Simona Bordoni, Paolo Davini (2024) Impact of stochastic physics on the representation of atmospheric blocking in EC-Earth3; https://doi.org/10.5194/wcd-5-1207-2024

2 IMPACT OF STOCHASTIC PHYSICS ON THE REPRESENTATION OF ATMOSPHERIC BLOCKING IN EC-EARTH3

ABSTRACT

Atmospheric blocking is a synoptic-scale phenomenon that consists in an obstruction of the normal easterly progression of weather patterns in the midlatitudes, leading to persistent atmospheric conditions sometimes associated with extreme weather. State-of-the-art climate models systematically underestimate winter atmospheric blocking frequency, especially over Europe. This is often attributed to a poor representation of small-scale processes that are fundamental for the onset and maintenance of blocking events. Here, we explore how the implementation of two stochastic parameterizations, namely the Stochastically Perturbed Parameterization Tendencies (SPPT) and the Stochastic Kinetic Energy Backscatter (SKEB) schemes, influences the representation of Northern Hemisphere winter blocking in EC-Earth3.

We show that the activation of the two stochastic schemes has moderate detrimental effects on blocking representation, when assessed through a gradient reversal index. Using a zonal-blocked flow linear decomposition we attribute such modification to changes in the mean winter atmospheric circulation, primarily manifested in a strengthening of the midlatitude jet stream and an intensification of the Hadley Cell. Ultimately, an analysis of the meridional transport of zonal momentum by stationary and transient eddies reveals that these circulation differences arise from changes in tropical stationary eddy activity. Our findings reconnect with earlier literature on similar experiments and suggest that the activation of stochastic parameterizations may require a retuning of the model to account for the resulting significant changes in the mean atmospheric circulation.

2.1 INTRODUCTION

Atmospheric blocking is a synoptic-scale weather phenomenon characterized by a quasi-stationary high-pressure low-vorticity system, which disrupts the usual eastward progression of weather patterns [1, 2]. Blocking is observed in both hemispheres and in all seasons, although it is most frequent in the Northern Hemisphere (NH) in boreal winter and spring. The anomalous circulation induced by blocking

can last from several days up to a few weeks, with significant impacts on regional weather conditions. Atmospheric blocking can arise from different weather configurations and a unique theory on its formation, development and decay, as well as a unique definition, remain elusive [3–5]. Yet blocking events share some common characteristics, like a deflection of the normal midlatitude westerly flow, which can result in a reversal of the climatological winds in the southern flank of the blocked region. Depending on the season, atmospheric blocking can cause a temperature anomaly dipole on its upstream and downstream flanks, sometimes leading to heat waves, drought or exceptional snowfall conditions [6–8].

Another peculiar feature of blocking is related to its numerical simulation: current state-of-the-art General Circulation Models (GCMs) struggle to correctly represent important features of atmospheric blocking, systematically underestimating its frequency especially over the European region. Additionally, only moderate progress has been made in recent years compared to other aspects of climate modeling [9, 10]. The inadequate representation of atmospheric blocking by GCMs is likely due to its inherent nature, which involves highly nonlinear dry and moist processes, where scale interactions are of key importance [1, 11–13]. These nonlinear interactions are difficult to capture both analytically and numerically, as models cannot explicitly resolve the wide range of scales of atmospheric motions due to limitations in computing resources. As a result, GCMs feature biases in atmospheric blocking frequency, especially over Europe [5, 9, 10]. Numerical Weather Prediction (NWP) models also have similar struggles with representing atmospheric blocking onset, systematically overestimating the propagation distance of Rossby Wave packets [14].

There is evidence that increasing GCMs' resolution is beneficial for better representing atmospheric blocking frequency [15–17]. Yet, there are numerous other elements of numerical modeling that compete for the same resources: the need to produce large enough simulation ensembles, to integrate over longer time windows and to model other Earth system components [18]. It has, therefore, been necessary to find a trade-off between explicitly representing small spatial scales and making use of expensive computational resources that may be required for other purposes.

The Stochastically Perturbed Parameterization Tendencies (SPPT) and the Stochastic Kinetic Energy Backscatter (SKEB) schemes, developed at the European Center for Medium-Range Weather Forecast (ECMWF) and implemented in their Integrated Forecasting System (IFS) [19], were designed to address model uncertainty by introducing perturbations that represent the effect of unresolved sub-grid scale variability. This is done by accounting for the propagation of errors from small to macroscopic scales and the turbulent cascade characteristic of turbulent motion through stochastic perturbations within the parameterizations of the climate model physics.

At first, stochastic parameterizations were adopted for numerical weather forecasts and have enhanced the reliability of medium range and seasonal ensemble forecasts by improving the probabilistic representation of atmospheric variability [19, 20]. Later on, several studies demonstrated how the same parameterizations

can also be beneficial at climate scales [e.g., 21, 22], by reducing model biases in a number of atmospheric circulation features [23, 24]. Interestingly, such improvements appear to be similar to those due to increased horizontal resolution [25]. In fact, by representing the atmospheric variability that arises from unresolved scales of the atmospheric flow, stochastic parameterizations can be thought of as an alternative to increasing model resolution at a fraction of the computational cost.

Among other aspects, the SPPT scheme has been shown to have a strong influence on tropical precipitation. Vidale *et al.* [26] showed how SPPT is ameliorating the representation of tropical cyclones by both improving the number of cyclone seeds and by providing more suitable conditions for their transition into tropical cyclones. Pickl *et al.* [27] showed that SPPT increases the frequency of strong upward motions and modifies tropical precipitation rates. Strommen *et al.* [28] found that the SPPT scheme alters the cloud liquid water content in tropical clouds and evaporation from the Earth's surface, slightly modifying the atmosphere radiative budget and the overall tropical climate [28, 29]. Both Strommen *et al.* [28] and Pickl *et al.* [27] attribute the systematic changes in tropical climate to the fact that a symmetric zero-mean perturbation can lead to a unidirectional response when applied to a nonlinear system. Such an effect is more evident in the tropics, as the magnitude of the SPPT perturbations on average scales with the magnitude of the deterministic tendency, which is larger in the tropics than in the extratropics [30].

Impacts of stochastic parameterizations are, however, not limited to the tropical climate. Focusing on midlatitudes, Dawson & Palmer [18] investigated the impact of SPPT on the representation of North Atlantic weather regimes, which are recurring and quasi-stable patterns of regional weather conditions that characterize the North Atlantic midlatitude climate. In their study, they showed that the SPPT scheme is able to improve the representation of weather regimes similarly to what seen when model resolution is increased. A similar result was obtained by Christensen *et al.* [31] in an idealized experimental setup. Atmospheric blocking is highly correlated with some of the North Atlantic winter weather regimes, suggesting that the representation of atmospheric blocking may likewise benefit from stochastic parameterizations. Moreover, a systematic review of the representation of atmospheric blocking in the IFS seasonal forecasts has shown how SPPT is able to modify the distribution and frequency of blocking events [32], slightly increasing blocking activity in low latitudes and decreasing it in midlatitudes. However, both Dawson & Palmer [18] and Davini *et al.* [32] only reported on the impact of SPPT without exploring the dynamical reasons leading to such changes.

Building on this existing body of work, in this paper we explore the extent to which the implementation of the SPPT and SKEB schemes improves the representation of atmospheric blocking in a state-of-the-art GCM, namely EC-Earth, which has IFS as its atmospheric component. More specifically, we aim at shedding light on the dynamical mechanisms affecting the representation of atmospheric blocking when stochastic schemes are implemented, hence reconciling our results with earlier literature. This is done by making use of the Climate SPHINX (Stochastic Physics HIgh resolutioN eXperiments) experiment dataset [33], a set of simula-

tions where EC-Earth was run at multiple horizontal resolutions with and without stochastic parameterizations. While the experiment dates back to 2017, it still represents an outstanding set of simulations and a so-far unexplored opportunity to delve into the representation of atmospheric blocking in this context. Moreover, the extensive number of studies that used the same dataset [e.g., 24, 26, 29] enables us to compare and connect our results with earlier findings on different aspects of the atmospheric circulation.

With these goals in mind, the paper is structured as follows: first, in Section 2.2, we describe the Climate SPHINX experiment (2.2.1), the stochastic parameterizations (2.2.2), the diagnostic tools employed in our analyses (2.2.3) and the physical quantities used in this study (2.2.4). Then, in Section 2.3 we move to the description of how the activation of the stochastic parameterizations impacts the atmospheric blocking frequency (2.3.1) and the NH winter mean state (2.3.2). More process-oriented insight in these observed changes is provided in Section 2.4, through a novel linear blocked-zonal flow decomposition (2.4.1) and an analysis of the zonal momentum balance (2.4.2). Lastly, in Section 2.5, we summarize and discuss our results.

2.2 METHODS

2.2.1 Data

The dataset we use in this work is the Climate SPHINX experiment dataset, which is composed of multiple ensemble members categorized per resolution and per parameterization [33]. The experiment has been carried out using EC-Earth v3.1, which is based on IFS cy36r4 [34, 35], in atmosphere-only configuration at five different horizontal resolutions: TL159 ($\sim$ 125 km), TL255 ($\sim$ 80 km), TL511 ($\sim$ 40 km), TL799 ($\sim$ 25 km), TL1279 ($\sim$ 16 km). The abbreviation "TL-x" stands for linear truncation: IFS is a spectral model and "x" indicates the spectral harmonic at which the truncation occurs. All the simulations have 91 vertical levels. The Climate SPHINX simulations considered here cover the historical period from 1979 to 2008. Further details on the boundary and initial conditions can be found in Davini *et al.* [33].

Simulations have been produced using two different model configurations: the "baseline" version of EC-Earth 3.1 and the "stochastic" version of the same model, in which both the SPPT [19, 36] and the SKEB [37, 38] schemes are used. For each of the two model setups, with and without the stochastic parameterizations, simulations have been run with different resolutions ranging from 125 km to 16 km, with decreasing ensemble size for increasing resolution. Available simulations are summarized in Table 2.1. As reference observational dataset, we use the ECMWF ERA5 reanalysis [39]. Both datasets have been regridded to a resolution of $2.5°\times2.5°$, which represents a good trade-off between resolution and a computationally light-weight analysis.

The analysis presented in this article focuses on the extended winter period

from December through March (DJFM). This choice is motivated by the fact that the winter period corresponds to the transient activity maximum, an aspect of the atmospheric circulation that is expected to be better represented through the adoption of stochastic parameterizations [18, 25, 33]. Indeed, most models struggle with representing wave-breaking atmospheric blocking events in the European sector [9, 10] which are most frequent in boreal winter and spring and whose frequency is influenced by transient eddy activity in the Northern Atlantic [40, 41].

The model tuning has been performed at TL255 resolution (the default EC-Earth3 configuration) in the deterministic configuration and the parameters are kept constant for all other simulations. This choice allows for a direct comparison between the various runs, with resolution and stochastic parameterizations being the only possible reasons for observed changes in simulated climate. A downside of this tuning strategy is that untuned resolutions can produce unrealistic behavior, as some of the parameterizations, even if mostly scale aware in IFS, might operate differently when smaller scales are dynamically resolved. For this reason, we exclude from our analysis the TL1279 resolution, for which, additionally, only a single ensemble member is available.

For the purpose of this analysis we performed an arithmetic non-weighted average over all ensemble members, which considers all members as of equal importance regardless of resolution. It is important to note how this procedure gives a larger weight to the lower-resolution experiments than to the higher-resolution ones, as the former's ensembles are larger in size. The averaging is performed only after nonlinear computations—such as atmospheric blocking frequency and other nonlinear variables—are performed. The choice to ignore the ensemble member resolution may seem counterintuitive, since it could be expected that the impact of the stochastic parameterization would decrease as resolution increases. Both the SPPT and SKEB parameterizations have been developed within a seamless prediction framework so that their impact on model physics is planned to decrease as resolution increases, making the parameterization suitable for both NWP resolutions and coarser GCM resolutions [36]. That said, our choice is motivated by the fact that an analysis of the differences between baseline and stochastic simulations grouped by resolution did not reveal significant differences, highlighting a systematic effect of the parameterizations that is almost independent of resolution (see Figures S2.1-S2.4 in the Supplementary Material). Additionally, averaging all available ensembles—composed of 29 members—allows us to obtain results that are statistically more robust. Statistical significance has been assessed through a Student's t-test. The variance of each variable has been calculated as the statistical variance among the ensemble members. The significance of the anomalies has been computed using the following formula:

$$T_s = \frac{< x_1 > - < x_2 >}{\sqrt{\sigma_1^2 + \sigma_2^2}} \tag{2.1}$$

Where T_s is the student T value, x_1 and x_2 are the ensemble means of the analyzed fields and σ_1^2 and σ_2^2 are their standard deviations. The T_s value has been therefore

Table 2.1: Number of ensemble members per resolution and experimental setup. Rows refer to the two experimental setup, the baseline and stochastic experiments, respectively, as described in Section 2.2.1. Columns refer to the available resolutions defined by their linear spectral truncation.

	TL159 ($\sim$ 125 km)	TL255 ($\sim$ 80 km)	TL511 ($\sim$ 40 km)	TL799 ($\sim$ 25 km)
baseline	10	10	6	3
stochastic	10	10	6	3

compared with a reference value for the 98% confidence interval chosen considering the size of the ensemble. Given the large number of ensemble members and simulated years, in all figures anomalies shown are significant at this confidence level.

2.2.2 SPPT and SKEB schemes

The SKEB and SPPT schemes have been developed at ECMWF specifically for the IFS model, which is the atmospheric component of EC-Earth. The SKEB scheme has been developed in order to represent the effect of the turbulent kinetic energy cascade [37, 38]: The energy that is dissipated at smaller scales is not lost by the system but is randomly distributed at larger scales through a perturbation of the deterministic streamfunction tendency. Being $\dot{\psi}(\phi, \lambda, z, t)$ the streamfunction tendency, $\dot{\psi}_{det}(\phi, \lambda, z, t)$ the deterministic tendency and $f(\phi, \lambda, z, t)$ a random perturbation of the streamfunction, the stochastic scheme operates so that

$$\dot{\psi}(\phi, \lambda, z, t) = \dot{\psi}_{det}(\phi, \lambda, z, t) + f(\phi, \lambda, z, t) \tag{2.2}$$

Even though the SKEB scheme accounts for variability that is not represented in the deterministic version of the model, its impact on the simulated climate is negligible [33].

The major impact on the representation of atmospheric variability comes from the SPPT scheme, which has been developed in order to represent the influence of sub-grid variability on the large-scale dynamics [19, 36]. SPPT introduces variability by perturbing the deterministic parameterization tendencies of the temperature, specific humidity and wind fields as follows:

$$\frac{\partial X}{\partial t} = D + K + (1 + \mu e) \sum_i P_i \tag{2.3}$$

where X is the total tendency of each of the physical quantities above, D is the dynamical tendency, K the horizontal diffusion and P_i is the tendency coming from the ith parameterization scheme (radiation, turbulence and gravity wave drag, non-orographic gravity wave drag, convection, and large-scale water processes). The term in the parenthesis e is a zero-mean perturbation and μ is a parameter that sets the perturbation to zero at the surface and top atmospheric boundary. The perturbation e is generated as the sum of three independent patterns that are spatially

correlated at 500 km, 1000 km and 2000 km and have temporal decorrelation of 6 hours, 3 days and 30 days, representing the different scales of sub-grid variability that can be influenced by sub-grid scale processes.

2.2.3 Atmospheric blocking detection method

A plethora of blocking detection methods exist, and both the pattern and the magnitude of the resulting atmospheric blocking frequency can vary considerably depending on the chosen method [5]. These methods can be classified into two broad classes: absolute indices, which look for a specific wind pattern in the synoptic flow and anomaly indices, which look for field departures from the time mean. In the following, we adopt a two-dimensional absolute index based on the geopotential height gradient reversal, first developed by Tibaldi & Molteni [42] for a single latitudinal coordinate (60°N) and then extended to other latitudes (from 30°N to 75°N) by Scherrer *et al.* [43] and Davini *et al.* [44]. We also tested a simple implementation of an anomaly-based index similar to the one adopted by Woollings *et al.* [5] and we found that our results slightly change depending on the index used, even though our main conclusions remain unchanged. In particular, the anomaly index shows smaller sensitivity to the implementation of stochastic parameterizations compared to the gradient reversal one.

We opted for the gradient reversal index as absolute indices are suited for detecting atmospheric blocking originating from a Rossby wave-breaking event [5]. This is convenient as they look for a particular synoptic pattern rather than a geopotential height anomaly, which may be caused by a number of concurrent phenomena, making a process-based understanding more difficult to achieve. In addition to this, Rossby wave-breaking blocking is a crucial area of study as it impacts the midlatitudes during winter and its frequency is systematically underestimated by current state-of-the-art GCMs, especially over Europe [9, 10]. The additional analysis carried through the anomaly index can be found in the Supplementary Material (Figure S2.8).

The gradient reversal method operates as follows. For each grid-point we evaluate the northward ($GHGN$) and southward gradient ($GHGS$) of the geopotential height at 500 hPa, z_{500}:

$$GHGN(\phi_0, \lambda_0) = \frac{z_{500}(\lambda_0, \phi_N) - z_{500}(\lambda_0, \phi_0)}{\phi_N - \phi_0} \tag{2.4}$$

$$GHGS(\phi_0, \lambda_0) = \frac{z_{500}(\lambda_0, \phi_0) - z_{500}(\lambda_0, \phi_S)}{\phi_0 - \phi_S} \tag{2.5}$$

in which λ_0 and ϕ_0 represent the grid point longitude and latitude, respectively; ϕ_0 ranges from 30° to 75°N and λ_0 ranges from 0 to 360°; $\phi_s = \phi_0 - 15$ lat and $\phi_N = \phi_0 + 15$ lat. For a grid point of coordinates (λ_0, ϕ_0), an instantaneous blocking is identified if:

$$GHGS(\phi_0, \lambda_0) > 0;\ GHGN(\phi_0, \lambda_0) < -10\ \mathrm{m\,lat^{-1}} \tag{2.6}$$

We hence obtain a diagnostic matrix with temporal, latitudinal and longitudinal dimensions, where a boolean value indicates the occurrence of instantaneous blocking.

It is important to note, that albeit widely used in literature, gradient reversal indices as the one adopted here tend to occasionally identify tropical air masses as blocks, leading to an overestimation of blocking at low latitudes [45]. More stringent criteria have therefore been introduced for the low-latitude region [44], for instance, requiring that the meridional gradient of the geopotential height between 15° and 30° south of the blocked grid point be negative. Yet, in this study we opt not to apply such a filter as the lower latitudes are significantly affected by the stochastic parameterizations and the associated anomalies can inform us on systematic mean circulation biases.

On top of the instantaneous blocking detection, we implemented a tracking algorithm that can detect blocking events through a connected component analysis of the diagnostic matrix. Reconstructing the blocking trajectories can bring several advantages and helpful metrics, such as the atmospheric blocking events duration, area and center-of-mass displacement. However, in the context of the present analyses, the event detection has been exploited exclusively to apply persistence and area filters to blocking events. Atmospheric blocking events whose duration is shorter than five days have been rejected, as well as those events whose area is smaller than 500.000 km^2. By applying these filters we select blocking events that interest the synoptic scale and are quasi persistent, coherently with usual blocking definitions. More details on the tracking algorithm can be found in the Appendix.

In Section 2.3.1 atmospheric blocking frequency is calculated as the fraction of days (in percentage) for which a grid point is identified as blocked. In Section 2.4.1 we compute the frequency of blocking for a given area by selecting those days when at least 10% of the selected area is affected by blocking. The 10% threshold has been selected in order to have a blocking frequency magnitude of the same order of the grid point blocking frequency computed in Section 2.3.1. Our results, however, show little sensitivity to the chosen threshold (not shown).

2.2.4 Mean state analysis

To characterize the mean atmospheric circulation we calculate the transient kinetic energy (TKE) and the Eady Growth Rate (EGR). TKE is obtained by applying a fast Fourier transform temporal filter to the 250-hPa daily zonal and meridional velocity that selects wave activity on timescales shorter than six days. The highpass filter is hence equivalent to a $2-6$ day band pass. We then computed kinetic energy as:

$$TKE = \frac{u_{hp}^2 + v_{hp}^2}{2} \tag{2.7}$$

where the subscript hp denotes highpass-filtered data. The Eady growth rate at 850 hPa, a commonly used measure of baroclinic instability [46–48] and, hence,

of transient eddy activity, is computed as

$$\sigma = 0.31 \frac{f}{N} \frac{\partial u}{\partial z} \tag{2.8}$$

where f is the Coriolis parameter, N is the Brunt-Väisälä frequency, representing the stability of a parcel of air to vertical displacements, and z is the vertical coordinate.

2.3 IMPACT OF STOCHASTIC PARAMETERIZATIONS

2.3.1 Blocking representation

We start by assessing wintertime atmospheric blocking frequency in EC-Earth3, both in its baseline configuration and with stochastic parameterizations, compared against ERA5 (Fig. 2.1).

In its default baseline configuration (Fig. 2.1a), the model overestimates blocking at low latitudes, particularly in the equatorial central Pacific region, while it underestimates it in the midlatitudes over Europe, as commonly seen in several other GCMs [10]. On top of this, the model significantly underestimates blocking at high latitudes in the Bering Strait region. Depending on the specific focus region, relative biases in blocking frequency can be as high as $20 - 30\%$.

Moving to the stochastic configuration, Fig. 2.1b shows how the SPPT and SKEB parameterizations do not improve the represented atmospheric blocking frequency. If anything, blocking representation moderately deteriorates over Europe. The only area where some improvements can be seen is over Greenland and in the northernmost regions of the American continent, presumably because of less frequent intrusions of polar cold air masses.

The influence of the implementation of the stochastic paramaterizations on atmospheric blocking is more clearly highlighted in Fig. 2.1c, which shows the difference between the stochastic and baseline model versions. The most evident changes are an increased and decreased frequency at low and higher latitudes, respectively, particularly evident over the Euro-Atlantic region. This will therefore be the main focus area for the remainder of this paper. While a zonally oriented dipole is also evident over the Pacific, in this region the response to the stochastic parameterizations is weaker. The fact that the anomaly is larger at low latitudes and that the impact of stochastic parameterizations is independent of resolution (see Section 2.2.1 and Supplementary Material Figures S2.1-S2.4) suggests that the two stochastic schemes introduce a systematic change in the model mean state that is particularly evident at lower latitudes. Yet, to identify the origin of such differences a careful analysis of the entire NH winter mean circulation is necessary.

2.3.2 Mean winter climate and transient eddy activity

To investigate the reasons behind the deterioration of the Euro-Atlantic wintertime atmospheric blocking when stochastic parameterizations are implemented in EC-

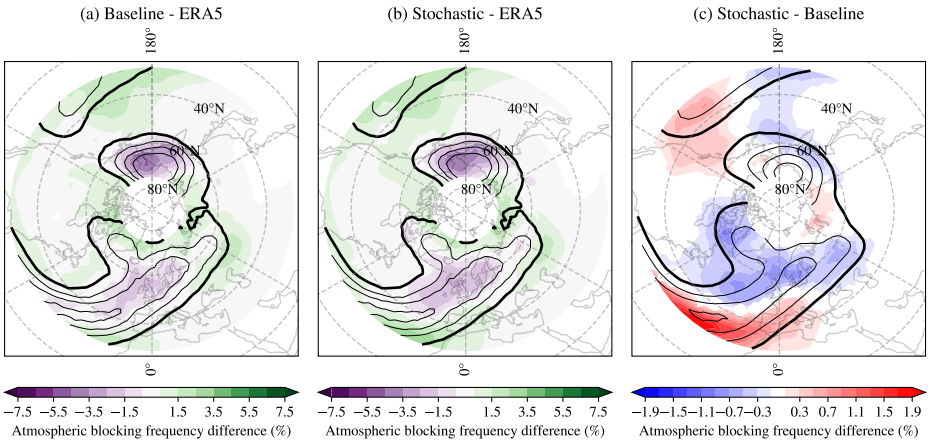

Figure 2.1: Ensemble mean DJFM climatology (1979-2008) of atmospheric blocking frequency given as percentage of blocked days: a) difference between the baseline version of the model and ERA5; b) difference between the stochastic version of the model and ERA5; c) difference between the stochastic and baseline versions of the model. In panels a) and b), shading shows differences in atmospheric blocking frequency, while black contours indicate blocking frequency in ERA5. In c), shading shows the difference in blocking frequency between the two model versions, while the black contours show blocking frequency from baseline ensemble. The thick contour refers to a frequency of 3% of days and contours are plotted every 3%.

Earth, we proceed by analyzing the NH winter mean climate and the transient eddy activity as represented by the stochastic and deterministic versions of the model.

Basic features of the mean atmospheric circulation are shown in Fig. 2.2, whose panel a) shows the zonally and seasonally (DJFM) averaged zonal wind on the meridional plane. The stochastic parametrizations result in a strengthening of the upper-tropospheric winds. This is evident for both the northern and southern hemispheres, even though they are in different solsticial conditions. The observed increase in zonal wind primarily affects the northernmost segments of the jet streams and goes together with the wind speed, i.e. the stronger the wind intensity, the larger the increase. Similar plots have been produced for the Euro-Atlantic sector only (see Supplementary Material Figure S2.5), where it is easier to discern a split-jet structure with a clear separation between the eddy-driven and the thermally driven jets. It appears that both jet components are reinforced, even though the eddy-driven jet features a slightly larger increase.

Fig. 2.2b shows the DJFM zonally averaged streamfunction, which identifies the mean meridional circulation. Focusing on the tropics, the Hadley cell extent remains relatively unchanged, in agreement with an earlier study by Strommen *et al.* [28] using the same model and parameterization. However, the streamfunction features positive anomalies, indicative of a strengthening, in the stochastic simulation in the ascending and the descending branches of the NH winter cell. The strengthening is more pronounced in the ascending branch, revealing how the stochastic parameterization preferentially enhances upward motions, leading to a relative change of 5–10% of the climatological streamfunction and a consequent enhanced meridional gradient.

In addition to changes in the climatological winds, we investigate the impact of the stochastic parameterization on the high-frequency atmospheric variability by analysing two mean-state diagnostics. First, we analyze the NH transient eddy activity in DJFM by computing the 250-hPa TKE. Fig. 2.3a reveals that the stochastic parameterization significantly increases TKE in both hemispheres. While the increase is more pronounced in the winter hemisphere, noteworthy changes are also present in the summer hemisphere. Differences peak at $5-10\%$ in the regions of maximum mean TKE values, i.e., in the storm-track regions. An increase in TKE might be associated with multiple changes: an increase in the amount of transient eddies, an increase in their spatial scale, and/or an increase in their intensity (e.g., vorticity anomaly). In the midlatitudes, an increase in TKE might be due to an increase in the overall atmospheric baroclinicity, by which baroclinic instability and transient eddy formation are promoted in the storm tracks. However, note how TKE is observed to increase also in the tropics.

To explore the possible connection between TKE and baroclinic eddy activity, in Fig. 2.3b we show the influence of the stochastic parameterization on the Eady growth rate (EGR). It is evident how EGR increases in regions where EGR itself is maximum, indicating larger instability for areas of high baroclinicity (again, the storm tracks). Such finding supports the hypothesis of an increased number of transient eddies, but does not provide information on the possibility of stronger

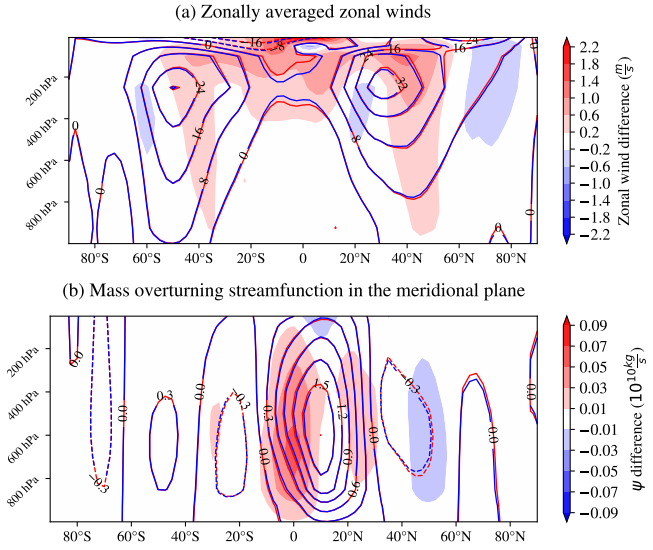

Figure 2.2: a) DJFM zonally averaged zonal winds $[m\,s^{-1}]$***. b) DJFM Mass overturning streamfunction in the meridional plane*** $[10^{10}\,kgs^{-1}]$***. In each plot, the black contours represent the baseline version of the model, while shading shows the difference between the stochastic and baseline versions.***

vorticity anomalies or larger eddy length scale.

Overall, the picture that emerges from the mean-state analysis (Figs. 2.2 and 2.3) is one of a more vigorous Hadley circulation that results in an enhanced meridional transport of zonal momentum and a strengthened thermally driven jet. The enhanced wind shear and the resulting thermal-wind balanced meridional temperature gradient are in turn coherent with increased EGR and TKE (Fig. 2.2a and Fig.2.3a) in the midlatitudes and a strengthened eddy-driven jet. The TKE increase in the tropics is compatible with the study of Vidale *et al.* [26], who highlighted how stochastic parameterizations are increasing the number of tropical cyclone seeds, but other sources of tropical transient eddies may also be implicated in the observed changes. While pointing to an influence of the tropical atmospheric circulation on the midlatitude winds in the chain of contributing causes highlighted above, our analyses are not sufficient to attribute causal relationships. In particular, the direction of causality between the strengthened zonal winds and the decreased blocking frequency cannot be unambiguously assessed. On the one hand, a strengthened jet stream leads to midlatitude dynamics in which nonlinear processes, such as blocking, occur less frequently [5, 41]. On the other hand, an increased blocking frequency can lead to a more frequent wind reversal that ultimately results in a weakening of the climatological wind speed. The nontrivial causal relationship between the two will be the object of the next Section.

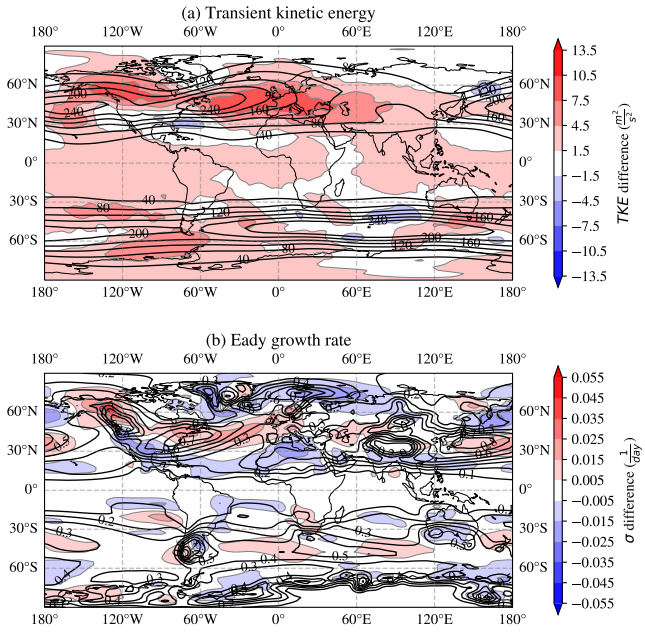

Figure 2.3: a) DJFM Transient kinetic energy (TKE, [$m^2\ s^{-2}$]) at 250 hPa and b) DJFM Eady growth rate (EGR, [day^{-1}]) at 850 hPa computed for the baseline and stochastic versions of EC-Earth model. In each plot, the black contours represent the baseline version of the model, while shading shows the difference between the stochastic and baseline versions.

2.4 MECHANISMS OF OBSERVED CHANGES

2.4.1 Blocked-Zonal flow decomposition

Atmospheric blocking onset and maintenance is highly dependent on the mean atmospheric state and transient variability, both of which have been shown to be affected by the stochastic parameterizations. Mean-state biases in models have been argued to be an important source of bias in the representation of atmospheric blocking [49, 50] and transient eddies have been linked to atmospheric blocking onset [41] and its maintenance [40]. In turn, the frequency of atmospheric blocking clearly influences the mean state, causing long-lasting geopotential height, zonal wind and temperature anomalies.

Therefore, it is not clear to what extent changes in atmospheric blocking frequency can be attributed to systematic changes in the mean atmospheric circulation, or, conversely, whether the atmospheric circulation is modified by a different atmospheric blocking representation primarily in lower latitudes. In other words: is it the mean atmospheric circulation that shapes the atmospheric blocking frequency or vice-versa?

In order to shed light on this causal relationship, here we propose a linear blocked-zonal flow decomposition. The linear decomposition is applied to a specific area, here chosen to be the portion of the northern Euro-Atlantic sector that spans from 60°W to 60°E and from 40°N to 70°N, corresponding both to the mid-latitude maximum of atmospheric blocking frequency as represented by the baseline version of the model (see Fig. 2.1) and to one of the regions where larger differences are observed when the stochastic parameterizations are activated. Specifically, the area in question features a lower blocking frequency in the stochastic simulations. We first express the climatological geopotential height as the sum of the climatological values during blocked and non-blocked days (the method used to identify the chosen area as blocked or non-blocked was described in Section 2.2.3). The difference in the climatological geopotential height in the stochastic version relative to baseline can hence be expressed as:

$$z - \hat{z} = [f z_b + (1 - f) z_z] - [\hat{f}\hat{z}_b + (1 - \hat{f})\hat{z}_z] \tag{2.9}$$

where z is the climatological geopotential height, f is the blocking frequency, and $(\,\cdot\,)_b$ and $(\,\cdot\,)_z$ refer to the average over "blocked" and "zonal" days, respectively, over the chosen area. Moreover, the hat symbol denotes fields from the baseline model version, whereas symbols without the hat denote fields from the stochastic version. After some simple algebra, Eq. 2.9 becomes:

$$z - \hat{z} = \underbrace{(f - \hat{f})(z_b - z_z)}_{\text{i}} + \underbrace{\hat{f}[(z_b - \hat{z}_b) - (z_z - \hat{z}_z)]}_{\text{ii}} + \underbrace{z_z - \hat{z}_z}_{\text{iii}} \tag{2.10}$$

where the stochastic–baseline height anomaly is partitioned into three contributions arising from differences between the two model versions in: (i) blocking

frequency; (ii) blocking pattern during blocked days; (iii) mean state during non-blocked days.

Height anomalies and the three terms contributing to the linear decomposition described above are shown in Fig. 2.4. Panel 2.4a—reporting the left hand side of Eq. 2.10—illustrates how the stochastic parameterization modifies the mean geopotential height within the considered region. Notably, the spatial patterns of these differences resemble the pattern found in Fig. 2.1c, depicting the atmospheric blocking frequency differences between the stochastic and baseline runs: a dipole structure, with positive (negative) anomaly in the lower (higher) latitudes over the Atlantic. This is not surprising, as atmospheric blocking is highly dependent on mean-state biases and is expected to occur in regions where stationary anticyclonic zonal anomalies are found (the stationary waves crests, [5]). That said, an increased atmospheric blocking frequency can also influence the mean geopotential height field. In the latter case, we would expect the geopotential height anomaly to be present only in days when blocking occurs.

By examining the other three panels (Fig. 2.4b, 2.4c, 2.4d), which correspond to the various terms of the decomposition, it becomes clear that the geopotential height differences arise primarily from changes during days when atmospheric blocking is not occurring. Since changes in the geopotential height field are not linked to alterations in blocking frequency or atmospheric blocking patterns, then it is the mean-state change that influences the overall positioning of stationary waves and the locations of blocking events. To answer the question posed at the beginning of this Section—is it the mean atmospheric circulation that shapes the atmospheric blocking frequency or vice-versa—it is thus likely that the stochastic parameterization has little effect on the representation of blocking dynamics, so that we cannot distinguish any improvement in the represented frequency due to the background change caused by the modified atmospheric circulation.

Moreover, the geopotential height differences depicted in the top right panel and in the bottom left panel reveal that the changed atmospheric circulation is producing less frequent blocking, that is, on average, producing larger geopotential height positive anomalies. The same result was obtained producing atmospheric blocking composites over the Scandinavian and Greenland regions (not shown). Yet we do not interpret these features as a direct effect of the stochastic parameterizations on atmospheric blocking, but rather as an indirect effect due to the changed atmospheric circulation.

2.4.2 Mean meridional momentum transport

Our analyses so far have shown how the use of the SPPT and SKEB stochastic parameterizations causes changes in the winter mean atmospheric circulation that deteriorate the representation of the frequency of atmospheric blocking. Here we attempt to explain differences in the wintertime mean circulation and to reconcile our results with existing literature on the same stochastic parameterizations.

To this aim, we analyze the winter zonally averaged meridional transport of

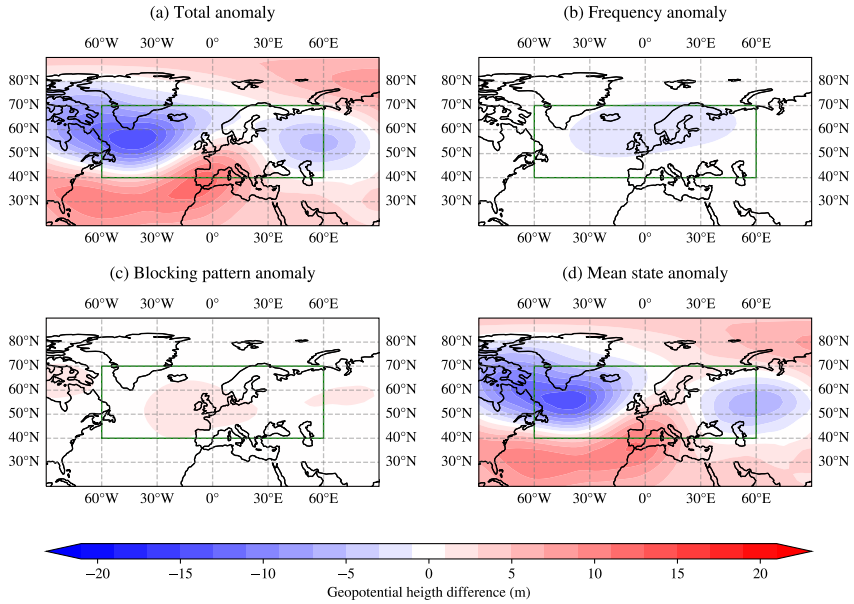

Figure 2.4: Linear Blocked-zonal flow decomposition in the focus area highlighted by the green rectangle. a) Geopotential height $[m]$ climatological difference between the stochastic and baseline model versions and contributions to this anomaly arising from: (b) differences in blocking frequency; (c) differences in blocking patterns; (d) differences in the mean state during the non-blocked days. See the text for more details.

westerly momentum in the midlatitudes and in the tropics, in order to understand why in the stochastic model version the upper-level zonally averaged zonal winds are strengthened. We further decompose this term into contributions by the mean meridional circulation, and contributions by transient and stationary eddies [e.g., 51], as:

$$[\overline{vM}] = [\overline{v(\Omega a\cos\theta + u)ua\cos\theta}] = \underbrace{[\overline{v}](\Omega a\cos\theta + [\overline{u}])a\cos\theta}_{\text{i}} + \underbrace{[\overline{v'u'}]a\cos\theta}_{\text{ii}} + \underbrace{[\overline{v}^*\overline{u}^*]a\cos\theta}_{\text{iii}} \tag{2.11}$$

with angular momentum about the Earth's spin axis $M = (\Omega a\cos\theta + u)a\cos\theta$, Earth's rotation rate Ω and Earth's radius a. Using standard notation, $[\,\cdot\,]$ denotes a zonal mean, $\overline{(\,\cdot\,)}$ denotes a temporal mean, and $(\,\cdot\,)'$ and $(\,\cdot\,)^*$ denote deviations from the temporal and zonal mean, respectively. With this decomposition, the three terms on the right-hand side represent contributions by: (i) the mean meridional circulation, (ii) the transient eddies, (iii) the stationary eddies.

Fig. 2.5 shows these terms for DJFM, with the baseline run confirming the well-known fact that in the midlatitudes westerly momentum transport is primarily accomplished by transient eddies, with some contributions from stationary waves in the NH, while in the tropics transport is primarily effected by the mean meridional circulation and the stationary eddies [52].

Moving to the differences between the stochastic and deterministic runs, we find that the activation of the stochastic parameterizations causes an increased southward momentum transfer at low latitudes and an increased northward momentum transport in the NH midlatitudes (Fig. 2.5a). Changes are primarily confined to the higher troposphere, except for a latitudinal band at $\sim 50^o N$, coinciding with the winter storm-track region, where anomalies in momentum transport reach the lower levels. When looking at contributions by the different components, we find that the main difference is in the stationary-eddy term in the equatorial region (Fig. 2.5d). The stationary eddies in the tropics are transporting more zonal momentum southward in the stochastic runs than in the baseline runs. Conversely, the stationary eddies in the midlatitudes are transporting more momentum northward. Yet, the differences in the midlatitudes are small compared to the equatorial region, the latter being twice as big as the former. The mean meridional circulation, namely the Hadley circulation, contributes to the strengthening of zonal winds in the midlatitudes by transporting more zonal momentum northward in the stochastic runs (Fig. 2.5b), confirming results from Fig. 2.2. The transient eddy momentum transport differences are modest, especially in the tropical regions, where their change is 50% smaller than the change in stationary wave transport (Fig. 2.5c). Still, that changes in these two terms have similar patterns suggests a common mechanism altering both the stationary and transient eddy transport.

To address our initial question, the modified NH winter circulation, which is causing a different winter atmospheric blocking frequency, is likely to arise from modified stationary waves in the tropics, whose momentum transport is the most affected by the stochastic parameterizations. A possible explanation to such dif-

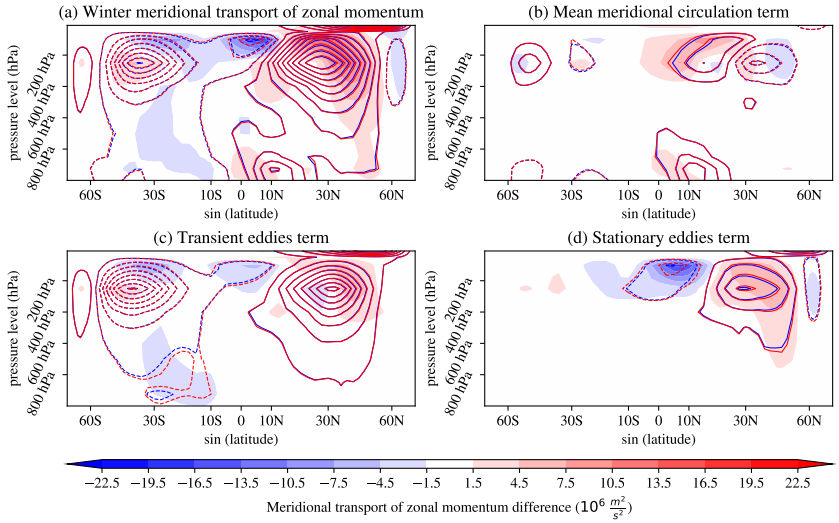

Figure 2.5: DJFM meridional transport of zonal momentum. Blue contours represent the baseline runs, red contours the stochastic runs and the shading the difference between the two (stochastic − baseline). (a) Total transport; (b) meridional transport of mean zonal momentum by the mean meridional circulation; (c) contribution by transient eddies; (d) contribution by stationary eddies . The contours are plotted with a spacing of 0.4×10^8 ***m^2 s^{-2} from*** 0.2×10^8 ***and*** -0.2×10^8 ***m^2 s^{-2}. Thick contours are positive and dashed contours are negative. Units for the shadings colorbar are*** $[m^2 s^{-2} 10^6]$***. Please see text for additional information.***

ferences is the development of stronger Gill-Matsuno waves that originate from enhanced diabatic heating in the warm pool region, involving equatorial Rossby and Kelvin waves [53, 54]. Rossby waves converge westerly momentum in their source region, producing the equatorward zonal momentum flux evident in the large modifications in the equatorial zonal momentum transport. At the same time, the enhanced diabatic heating, and associated upper-tropospheric divergence, acts as a wave source for extratropical Rossby waves, altering the midlatitude wave activity and stationary waves pattern [55–57]. Given the magnitude of the tropical anomalies compared to those in the midlatitudes, it is plausible that differences in the midlatitudes emerge mainly as a response to changes in the tropics. Moreover, the mean meridional circulation adjusts to the modified tropical stationary eddy activity in a way similar to what is described in the study from Dima *et al.* [51]. In particular, the Hadley cell intensifies to balance the increased stationary eddy meridional momentum transport (Fig. 2.2) and the associated meridional transport of westerly momentum further intensifies the jet stream. In a chain of contributing causes, the strengthened jet stream and the modified midlatitude stationary waves reduce blocking activity along the midlatitudes, particularly over the North Atlantic (Fig. 2.1)

The modified diabatic heating in the tropical region may be originating from altered condensation and precipitation processes, as discussed by previous literature on the SPPT scheme [26–28]. This mechanism will be further discussed in the Section 2.5 with concluding remarks.

In Fig. 2.6 we report the geopotential height contours in the tropical region, comparing the stochastic simulations with the baseline simulations. It is possible to identify the Gill-Matsuno pattern over the western Pacific, with Rossby wave spreading to the west of the warm pool and the Kelvin wave to the east, for both the stochastic and baseline ensembles. It is clear how anomalies in the geopotential height field at 250 hPa are small in midlatitudes, while those in the tropics considerably modify the tropical circulation.

In order to further confirm the relationship between the large-scale mean circulation changes and a modified tropical circulation, we compute the top-of-atmosphere (TOA) energy balance. We find differences that peak at $\sim$ 4 W m^{-2} at tropical latitudes (Supplementary Material Fig. S2.6). These changes are not found in clear-sky conditions, indicating a role of clouds and convection in perturbing the TOA energy balance and further reconciling our work with previous findings from Vidale *et al.* [26], Pickl *et al.* [27], and Strommen *et al.* [28, 29]. To determine underlying mechanisms would require further analyses that are beyond the scope of this paper, but additional details can be found in earlier studies that delved into this particular subject mentioned above.

2.5 CONCLUSIONS

In the present work we show how the activation of the SPPT and SKEB stochastic parameterizations in EC-Earth results in a deterioration of the representation of bo-

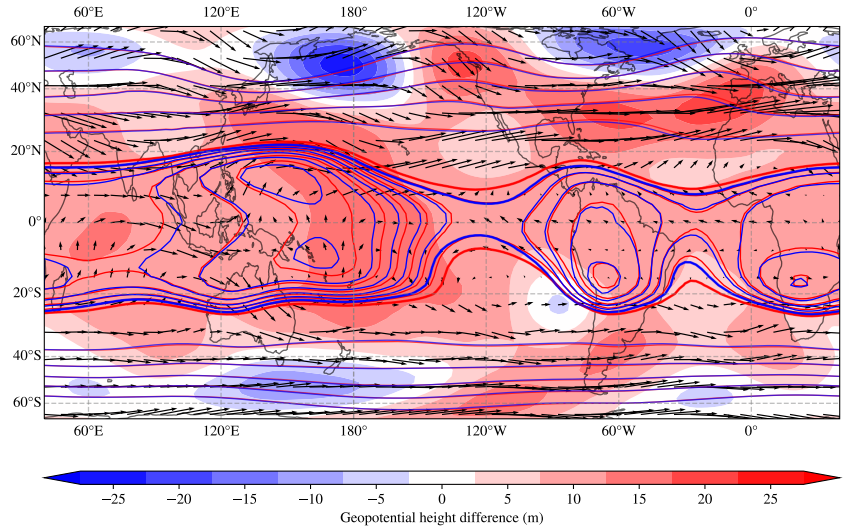

Figure 2.6: DJFM geopotential field at 250 hPa $[m]$ for baseline (stochastic) simulations in blue (red) line contours and difference between the two in shading. Contours are plotted every 10 m (200 m) for levels higher (lower) than 10900 m (thick contour). Note that a Lambert Cylindrical projection has been used, highlighting the equatorial region. The displayed vectors represent the climatological wind at 250 hPa averaged for all the baseline simulations.

real winter atmospheric blocking assessed through a gradient reversal index. Particularly, focusing on the European region, stochastic parameterizations not only do not improve the common underestimation of blocking frequency by climate models, but in fact, lead to larger biases in blocking frequency, with an increase in low-latitude and a decrease in midlatitude blocking.

To pinpoint mechanisms responsible for these changes in atmospheric blocking frequency, we analyse changes in NH winter mean circulation and transient eddy activity. Our analyses show how jet streams in both hemispheres, especially in their northern flanks, intensify, as does the ascending branch of the NH winter Hadley cell. These mean-state changes are accompanied by an increase in the energy associated with transient eddy activity consistent with both enhanced baroclinicity in the storm-track regions and the strengthened jet stream.

To investigate the causal relationship between changes in the NH winter mean circulation and changes in atmospheric blocking, we perform a decomposition of the 500-hPa geopotential height difference between the stochastic and deterministic simulations over the northern Euro-Atlantic sector. We find that the mean geopotential height is not significantly affected by a change in atmospheric blocking patterns or frequency. Rather, the changed blocking frequency reflects a changed mean state, with a modification coherent with a jet stream strengthening. To further highlight involved mechanisms, we perform a decomposition of the meridional transport of westerly momentum and we show that changes in the mean circulation can be attributed to modified stationary wave momentum fluxes in the tropics. Building on previous work using the same modeling framework, we speculate that such a modification arises from the tropical stationary wave response to enhanced diabatic heating due to modified condensation and precipitation processes in the tropics.

Therefore, our study gives rise to two distinct outcomes. The first one concerns the implemented stochastic parameterizations, in particular SPPT, which has the largest impact on the atmospheric circulation [33]. Even though the SPPT scheme has been originally developed to better represent sub-grid variability and achieve a nondeterministic representation of climate, we show that it has a systematic impact on the mean atmospheric circulation, regardless of model resolution. In particular, Strommen *et al.* [28] found that cloud liquid water content in tropical clouds is increasing when SPPT is implemented. The difference was attributed to an asymmetrical process of water condensation: while a stochastic perturbation of humidity in an air parcel can lead to condensation, the evaporation of condensed water into water vapour is not directly affected by the parameterization. It is important to note that, in order to overcome this imbalance, a fix to the SPPT scheme has been implemented [58], namely a 'super-saturation limiter', which sets the perturbation to zero when it would lead to condensation. However, a stochastic perturbation may still bring an air parcel closer to condensation, whereby the model dynamics trigger the process at the successive temporal step. The condensation process therefore remains asymmetric through the combined effect of the model dynamics and the stochastic physics. Similar asymmetric responses to zero-mean perturbations fol-

lowing the activation of SPPT are described by Pickl *et al.* [27], who found that the stochastic scheme is increasing the occurrence frequency of rapid ascending motions in the tropical region. The authors argue that such modifications affect ascending motions and not descending motions because of the dynamical characteristics of the system; while ascending motions can become unstable, the same argument does not hold for descending motions. In this sense, zero-mean stochastic perturbations can lead to an asymmetric circulation response. The same mechanism has been observed by Deinhard & Grams [59] for a new stochastic scheme, the Stochastically Perturbed Parameterization (SPP), which directly represents parameter uncertainty in parameterizations within the IFS model. Such phenomena are coherent with what was found by Vidale *et al.* [26] while studying the impact of SPPT on tropical cyclones; the authors found that when SPPT is implemented the ascending motions associated with the cyclones onset, the 'cyclone seeds', are more frequent.

As made evident by the study from Vidale *et al.* [26], such modifications do not necessarily lead to biases in the representation of the tropical climate. Indeed, the cyclone seed number found by Vidale *et al.* [26] for stochastic simulations is actually closer to observations than that obtained with the deterministic model. Moreover, the asymmetric response to a zero-mean perturbation described by Pickl *et al.* [27] is a common feature of dynamical systems applicable to several natural processes. Yet, it is necessary to underline that these modifications lead to changes to the model mean state. Specifically, in light of the significant atmospheric circulation changes, a retuning of the model when the SPPT scheme is activated seems necessary.

Once a retuning of the model is performed, it would then be possible to assess whether stochastic parameterizations are leading to improvements of atmospheric blocking representation that are now offset by significant mean state modifications. If these improvements were to be present, however, they would likely be small compared to the EC-Earth bias. Otherwise they should have been observable despite the impact of the stochastic parameterizations on the mean state, which itself is small compared to the model bias (see Fig. 2.1).

The second outcome directly concerns the representation of atmospheric blocking in GCMs. The blocked-zonal flow decomposition highlights how the modified blocking frequency has little impact on the mean circulation, while modifications of atmospheric blocking frequency closely resemble mean circulation differences. The emergence of atmospheric blocking frequency biases from mean circulation biases is a well-established concept in the existing literature. Indeed, Scaife *et al.* [49] already showed how absolute indices used for blocking detection are sensitive to mean-state modifications. More specifically, even a slight alteration in the zonal wind climatological pattern can lead to significant changes in atmospheric blocking behavior, a finding that was corroborated by a later study [50]. Along the same lines, Davini *et al.* [60] show how increased model resolution can affect blocking representation by better resolving land orography and enhancing the representation of midlatitudes stationary waves. Similarly, here we show how remote

changes in the tropical wave activity have a greater impact on the dynamics of blocking than the local impact of the stochastic parameterizations, strongly modifying atmospheric blocking frequency through modifications of the overall meridional zonal momentum transfer. This is particularly evident when an absolute index is adopted, as in our main analysis, but we found similar modifications of blocking climatological frequency through an anomaly based index (see Supplementary Material, Fig. S2.8).

This result implies that, when studying blocking in climate models, great attention should be given to the underlying mean state, as its representation can have a strong impact on blocking onset region and frequency. Even though our findings do not pinpoint the cause for the underestimation of blocking frequency over the European region by EC-Earth, they highlight how improved understanding of sources of biases in atmospheric blocking requires consideration of different features of the atmospheric circulation and their interactions. Our results stress once again how a wide-perspective approach is necessary to understand the long-standing deficit of climate models in the representation of blocking.

2.6 APPENDIX

2.6.1 Lagrangian tracking algorithm

In this study we adopt an atmospheric blocking detection method based on the 2D index of the geopotential height gradient reversal first introduced by Scherrer *et al.* [43] and later described and further developed by Davini *et al.* [44]. The gradient reversal criteria described in Section 2.2.3 is used to identify instantaneous blocking. On top of it, it is expedient to apply a series of filters to assure that the detected events share common blocking characteristics.

Davini *et al.* [44] apply filtering from an Eulerian perspective: each grid point is analyzed to investigate whether the instantaneous blocking condition is satisfied for more than 5 consecutive days. Moreover, a spatial filtering that selects only blocked areas larger than 500.000 km^2 is applied.

In this study we adopt a different perspective by performing a Lagrangian tracking: we identify each blocking event as a set of blocked areas corresponding to different days and we inspect its characteristics, computing the area, the duration, the center of mass and its displacement. Only the events that satisfy a specified set of conditions are retained, namely a minimum area for each blocked day, minimum persistence and a day-by-day overlap criterion. The latter defines the fraction of the grid-cells that a blocked area must share with the blocked area of the following day to be assigned to the same blocking event. Threshold values for the three criteria are coherent with those identified by Davini *et al.* [44]: 500.000 km^2 area, 5 days persistence and 50% overlap. A flow chart of the algorithm is shown in Fig. A2.1.

Identifying blocking events rather than blocked grid points brings several advantages. As an example, it is possible to study the trajectory of the blocking center of mass by analyzing the path of blocking events that interest a certain area and

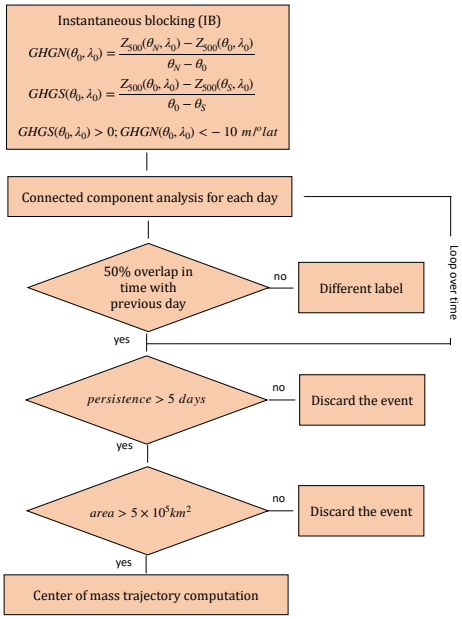

Figure A2.1: Simple flow chart of the Lagrangian Tracking algorithm.

achieving a better understanding of blocking behavior. Moreover, inspecting the blocking characteristics such as average area, displacement and duration is made rather simple, both for individual events and for specified regions and time periods.

In this article we do not exploit the full potential of the algorithm, as a Lagrangian investigation is not necessary for the narrative of the paper. The full characteristics and features of the algorithm will be exploited and shown in more details in future studies. However, for completeness, blocking climatology plots showing the impact of the applied thresholds can be found in the Supplementary Material (Figure S2.7). The full code of the Lagrangian Tracking Algorithm (named "blocktrack") can be found on the Github repository https://github.com/michele-filippucci/blocktrack.

2.7 SUPPLEMENTARY MATERIAL

2.7.1 The dependence of the climatological blocking frequency on model resolution

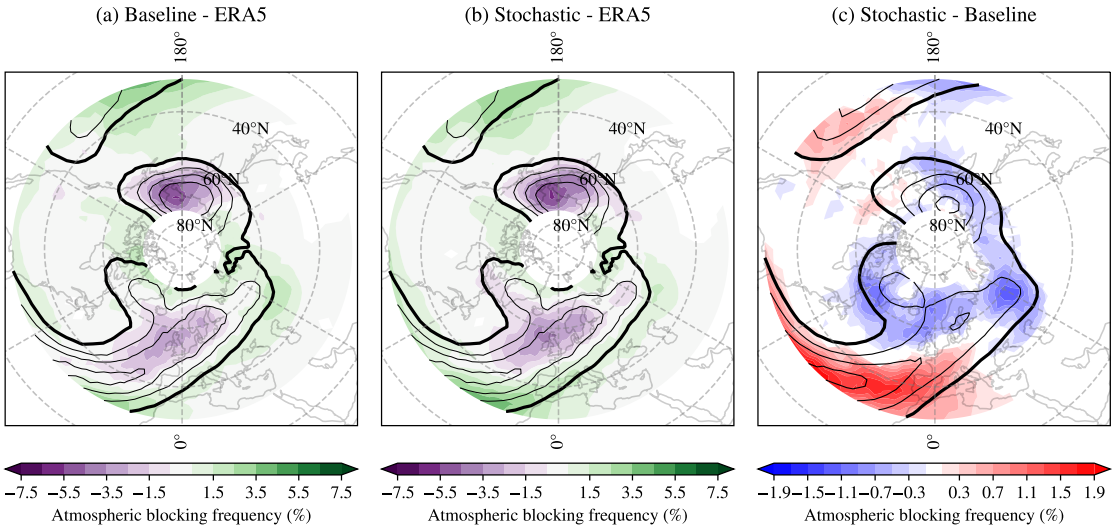

Figure S2.1: Climatological blocking frequency for December, January, February and March (DJFM) for TL159 (∼ 125 km) model resolution given as percentage of blocked days: a) difference between the baseline version of the model and ERA5; b) difference between the stochastic version of the model and ERA5; c) difference between the stochastic and baseline versions of the model. In panels a) and b), shading shows differences in atmospheric blocking frequency, while black contours indicate blocking frequency in ERA5. In c), shading shows the difference in blocking frequency between the two model versions, while the black contours show blocking frequency from baseline ensemble. The thick contour refers to a frequency of 3% of days and contours are plotted every 3%

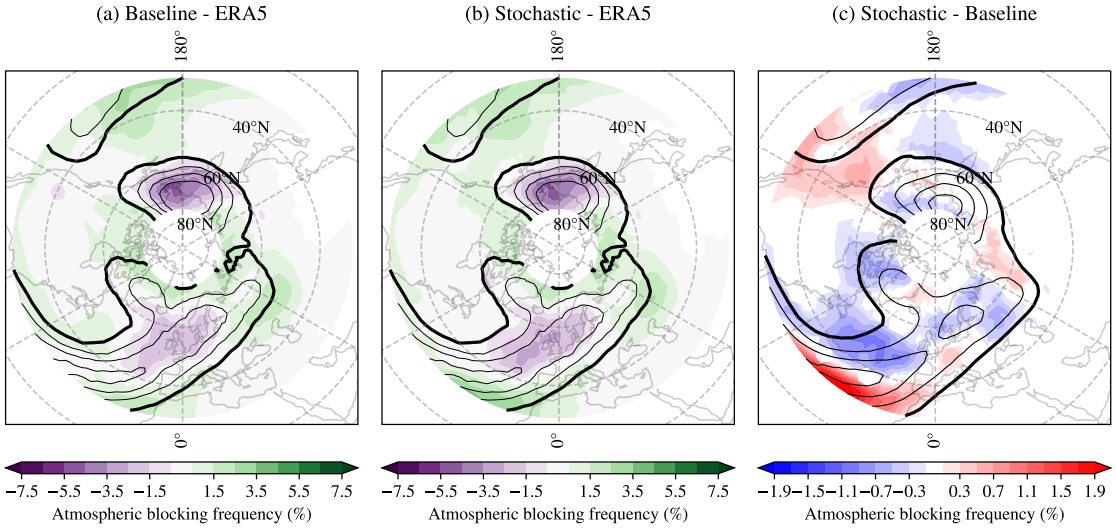

Figure S2.2: Climatological blocking frequency for December, January, February and March (DJFM) for TL255 (∼ 80 km) model resolution. Plot description as in Figure S1.

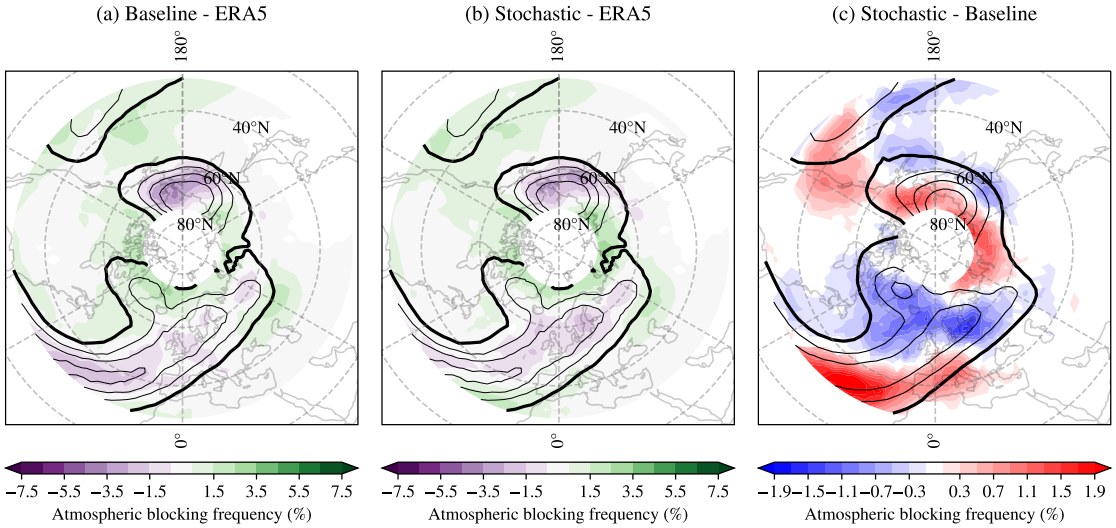

Figure S2.3: Climatological blocking frequency for December, January, February and March (DJFM) for TL511 (∼ 40 km) model resolution. Plot description as in Figure S1.

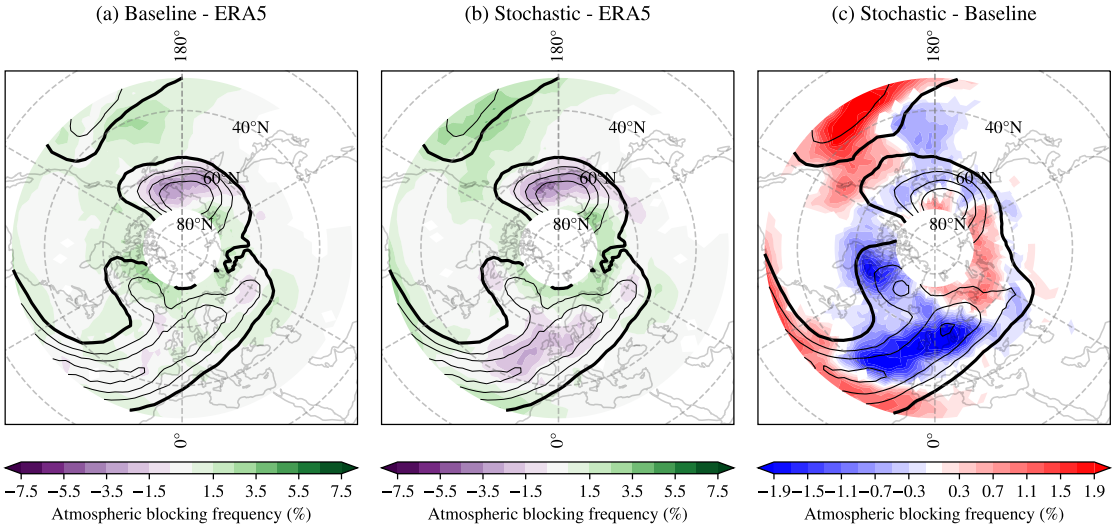

Figure S2.4: Climatological blocking frequency for December, January, February and March (DJFM) for TL799 (∼ 25 km) model resolution. Plot description as in Figure S1.

2.7.2 Zonal wind in the meridional plane over the Atlantic sector

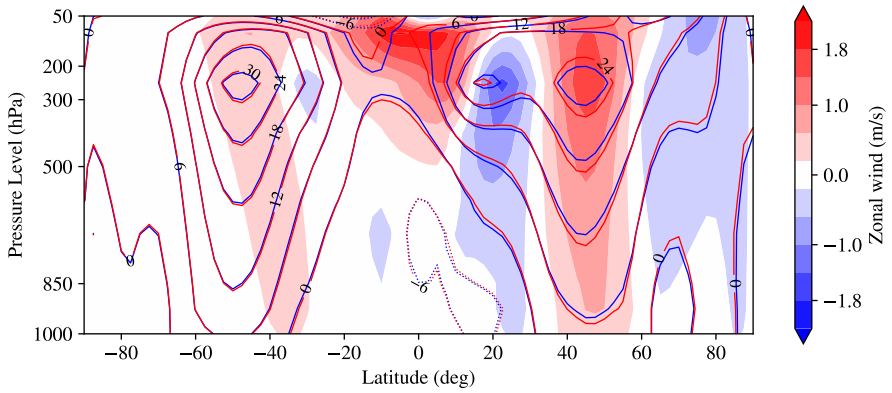

Figure S2.5: Zonal wind $[\frac{m}{s}]$ averaged over the Atlantic sector (65W,5W). Red (blue) contours indicate the stochastic (baseline) ensemble average, while shading represents the difference between the stochastic and baseline runs.

2.7.3 Top of the atmosphere radiative budget

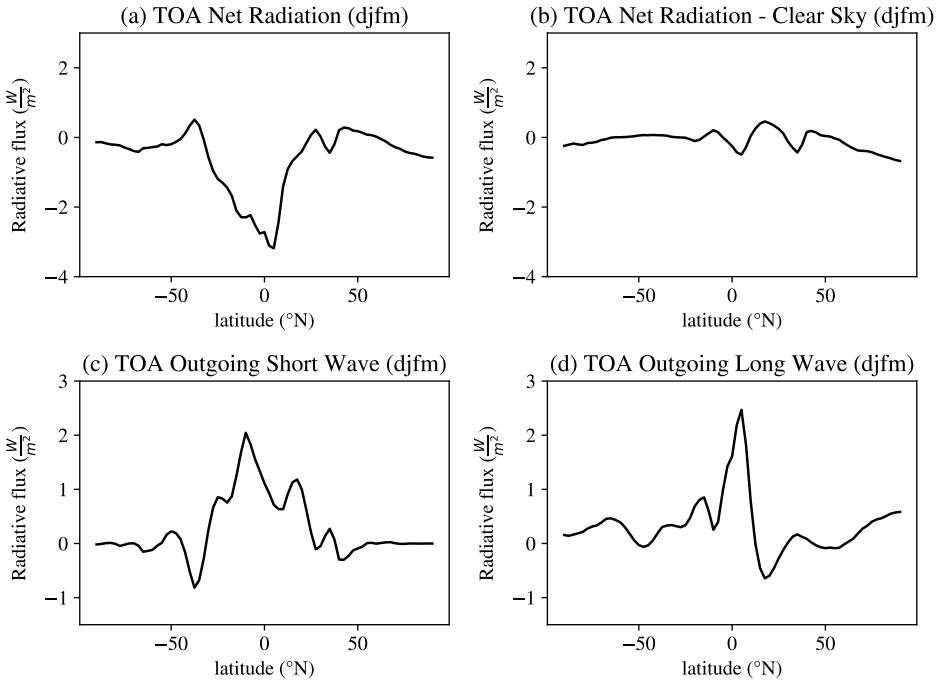

Figure S2.6: Differences in top-of-atmosphere (TOA) radiative fluxes [$\frac{W}{m^2}$] between the stochastic and baseline runs for the following quantities: a) TOA net radiative fluxes (Incoming shortwave - Outgoing shortwave - Outgoing longwave); b) Clear-sky TOA net radiative fluxes; c) TOA net shortwave radiation; d) TOA outgoing longwave radiation.

2.7.4 Impact of the chosen thresholds on the Lagrangian tracking algorithm for blocking detection

Figure S2.7: Climatological winter (djfm) atmospheric blocking frequency computed over ERA5 dataset 1979/2019. The frequency is given as percentage of blocked days and it has been calculated through the Lagrangian Tracking Algorithm based on the geopotential height gradient reversal index. Every plot corresponds to a set of chosen thresholds.

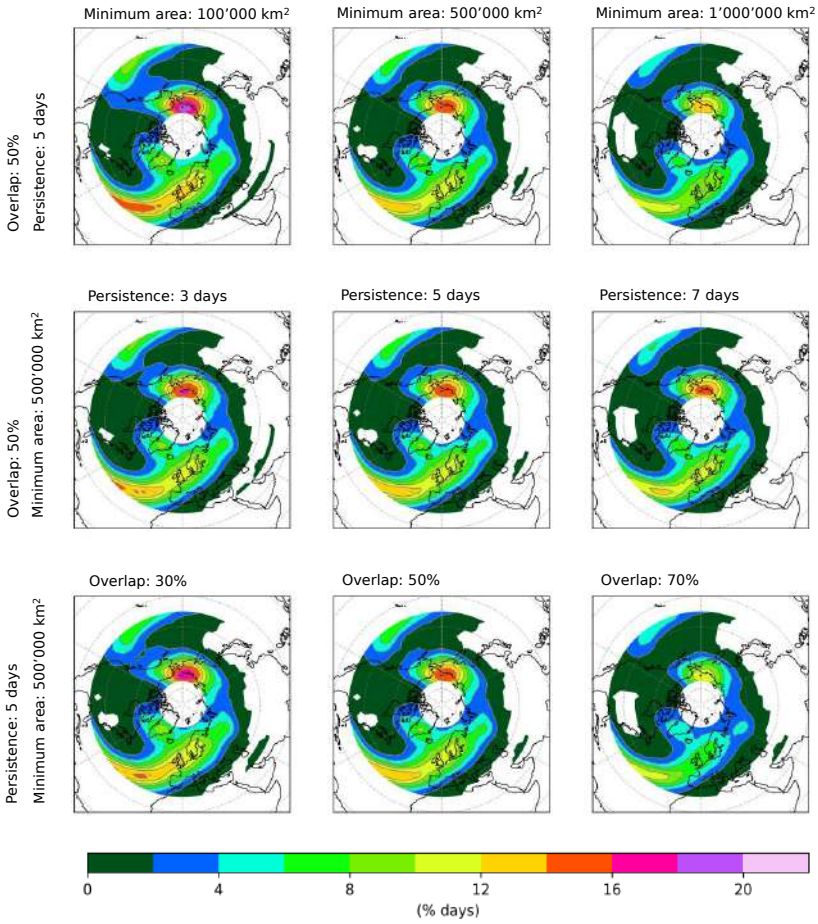

2.7.5 Climatological blocking frequency assessed through an anomaly based index for blocking detection

The GHA algorithm

We implemented a simple version of a Geopotential Height Anomaly (GHA) index based on [5]. The algorithm works as follows:

- The daily geopotential height at 500hPa is used as input data. We use a grid of 2.5°lat x 2.5° lon and we select the extended winter months (DJFM).

- We compute the daily geopotential height anomaly (Z') for each grid point of the input data. This is done by comparing the value of the geopotential height at each day and grid point with its mean value over a 90 days time window centered on the same day.

- We compute the standard deviation of the geopotential height anomaly over a longitude-latitude box [180°W,180°E], [40°N,80°N].

- We then identify the grid points where $Z' > M\sigma$. We set M to 1.26 in order to select values outside the 90% percentile of a normal distribution.

- Ultimately, we apply the Lagrangian tracking algorithm applying a persistence filter of 5 $days$ and a minimum area filter of $2 \cdot 10^6$ km^2 . The chosen thresholds are coherent with what we found in [5].

Results discussion

Figure S2.8a shows EC-Earth atmospheric blocking frequency assessed through the GHA index described above. The baseline version of EC-Earth underestimates blocking in the North Atlantic, except from higher latitudes, where blocking frequency seems to be slightly overestimated. Similarly, blocking frequency is underestimated in the Pacific at low latitudes and overestimated at high latitudes.

Moving to Figure S2.8b is is possible to observe how stochastic parameterizations have a little impact on blocking representation, with small improvements observed in eastern Siberia and over the Bering strait.

Changes introduced by the stochastic parameterizations are more clearly shown in Figure S2.8c, where it is possible to see how stochastic parameterization are displacing atmospheric blocking climatological frequency eastward.

The changes depicted by the GHA index differ from the ones assessed through the gradient reversal (GR) index in the main text. While the latter shows a deterioration of blocking representation over Europe, the former shows a slight improvement when stochastic parameterizations are implemented over the Pacific and no notable change in the Atlantic. However, the changes observed through the GHA index are again coherent with our mean state analysis as the frequency maxima displacement can be again attributed to a more vigorous and zonal jet stream that displaces the Northern Hemisphere stationary waves crests and blocking further east. The two indices detect features of the flow that, despite having different characteristics, still meet the definition of blocking. The GHA index is able to identify geopotential height anomalies, including persistent ridges, while the GR index looks for wind reversal and breaking Rossby waves ([5]). Hence, the results depicted here and in the main paper are not in contrast. Moreover, the fact that the differences depicted by the GR index are larger than those depicted by the GHA

index highlights how the former is more sensitive to mean state changes, a fact that was already noted in an earlier study by [49].

Figure S2.8: Ensemble mean DJFM climatology (1979-2008) of atmospheric blocking frequency given as percentage of blocked days computed through an anomaly based index (GHA): a) difference between the baseline version of the model and ERA5; b) difference between the stochastic version of the model and ERA5; c) difference between the stochastic and baseline versions of the model. In panels a) and b), shading shows differences in atmospheric blocking frequency, while black contours indicate blocking frequency in ERA5. In c), shading shows the difference in blocking frequency between the two model versions, while the black contours show blocking frequency from baseline. The thick contour refers to a frequency of 3% of days and contours are plotted every 3%.

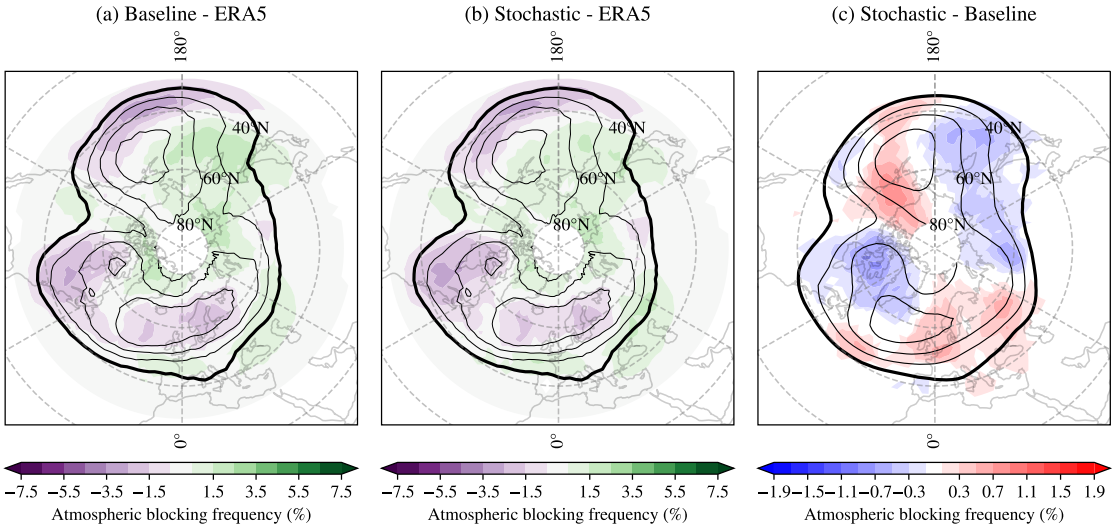

REFERENCES

1. Charney, J. G. & DeVore, J. G. Multiple flow equilibria in the atmosphere and blocking. *Journal of the atmospheric sciences* **36,** 1205–1216 (1979).
2. Hoskins, B. J. *et al.* On the use and significance of isentropic potential vorticity maps. *Quarterly Journal of the Royal Meteorological Society* **111,** 877–946 (1985).
3. Masato, G. *et al.* Wave-breaking characteristics of midlatitude blocking. *Quarterly Journal of the Royal Meteorological Society* **138,** 1285–1296. doi:`https://doi.org/10.1002/qj.990` (2012).

4. Barnes, E. A. *et al.* A methodology for the comparison of blocking climatologies across indices, models and climate scenarios. *Climate dynamics* **38,** 2467–2481. doi:https://doi.org/10.1007/s00382-011-1243-6 (2012).

5. Woollings, T. *et al.* Blocking and its response to climate change. *Current climate change reports* **4,** 287–300 (2018).

6. Rex, D. F. Blocking action in the middle troposphere and its effect upon regional climate. *Tellus* **2,** 275–301. doi:https://doi.org/10.3402/tellusa.v2i4.8603 (1950).

7. Buehler, T. *et al.* The relationship of winter season North Atlantic blocking frequencies to extreme cold or dry spells in the ERA-40. *Tellus A: Dynamic Meteorology and Oceanography* **63,** 174–187 (2011).

8. Sousa, P. M. *et al.* European temperature responses to blocking and ridge regional patterns. *Climate Dynamics* **50,** 457–477. doi:https://doi.org/10.1007/s00382-017-3620-2 (2018).

9. Masato, G. *et al.* Winter and summer Northern Hemisphere blocking in CMIP5 models. *Journal of Climate* **26,** 7044–7059 (2013).

10. Davini, P. & d'Andrea, F. From CMIP3 to CMIP6: Northern Hemisphere atmospheric blocking simulation in present and future climate. *Journal of Climate* **33,** 10021–10038 (2020).

11. Reinhold, B. B. & Pierrehumbert, R. T. Dynamics of weather regimes: Quasi-stationary waves and blocking. *Monthly Weather Review* **110,** 1105–1145 (1982).

12. Faranda, D. *et al.* The switching between zonal and blocked mid-latitude atmospheric circulation: a dynamical system perspective. *Climate Dynamics* **47,** 1587–1599 (2016).

13. Steinfeld, D. & Pfahl, S. The role of latent heating in atmospheric blocking dynamics: a global climatology. *Climate Dynamics* **53,** 6159–6180 (2019).

14. Quinting, J. & Vitart, F. *Representation of Synoptic-Scale Rossby Wave Packets and Blocking in the S2S Prediction Project Database, 430 Geophysical Research Letters, 46, 1070–1078* 2019.

15. Berckmans, J. *et al.* Atmospheric blocking in a high resolution climate model: influences of mean state, orography and eddy forcing. *Atmospheric Science Letters* **14,** 34–40. doi:https://doi.org/10.1002/asl2.412 (2013).

16. Schiemann, R. *et al.* The resolution sensitivity of Northern Hemisphere blocking in four 25-km atmospheric global circulation models. *Journal of Climate* **30,** 337–358. doi:https://doi.org/10.1175/JCLI-D-16-0100.1 (2017).

17. Davini, P. *et al.* Improved winter European atmospheric blocking frequencies in high-resolution global climate simulations. *Journal of Advances in Modeling Earth Systems* **9,** 2615–2634 (2017).

18. Dawson, A. & Palmer, T. Simulating weather regimes: Impact of model resolution and stochastic parameterization. *Climate Dynamics* **44,** 2177–2193 (2015).

19. Buizza, R. *et al.* Stochastic representation of model uncertainties in the ECMWF ensemble prediction system. *Quarterly Journal of the Royal Meteorological Society* **125,** 2887–2908 (1999).

20. Palmer, T. N. A nonlinear dynamical perspective on model error: A proposal for non-local stochastic-dynamic parametrization in weather and climate prediction models. *Quarterly Journal of the Royal Meteorological Society* **127,** 279–304 (2001).

21. Lin, J. W.-B. & Neelin, J. D. Toward stochastic deep convective parameterization in general circulation models. *Geophysical research letters* **30** (2003).

22. Arnold, H. *et al.* Stochastic parametrizations and model uncertainty in the Lorenz'96 system. *Philosophical Transactions of the Royal Society A: Mathematical, Physical and Engineering Sciences* **371,** 20110479 (2013).

23. Weisheimer, A. *et al.* Addressing model error through atmospheric stochastic physical parametrizations: Impact on the coupled ECMWF seasonal forecasting system. *Philosophical Transactions of the Royal Society A: Mathematical, Physical and Engineering Sciences* **372,** 20130290 (2014).

24. Yang, C. *et al.* The impact of stochastic physics on the El Niño Southern Oscillation in the EC-Earth coupled model. *Climate Dynamics* **53,** 2843–2859 (2019).

25. Berner, J. *et al.* Systematic model error: The impact of increased horizontal resolution versus improved stochastic and deterministic parameterizations. *Journal of Climate* **25,** 4946–4962 (2012).

26. Vidale, P. L. *et al.* Impact of stochastic physics and model resolution on the simulation of tropical cyclones in climate GCMs. *Journal of Climate* **34,** 4315–4341 (2021).

27. Pickl, M. *et al.* The effect of stochastically perturbed parametrisation tendencies (SPPT) on rapidly ascending air streams. *Quarterly Journal of the Royal Meteorological Society* **148,** 1242–1261 (2022).

28. Strommen, K. *et al.* Progress towards a probabilistic Earth system model: examining the impact of stochasticity in the atmosphere and land component of EC-Earth v3. 2. *Geoscientific Model Development* **12,** 3099–3118 (2019).

29. Strommen, K. *et al.* The impact of a stochastic parameterization scheme on climate sensitivity in EC-Earth. *Journal of Geophysical Research: Atmospheres* **124,** 12726–12740 (2019).

30. Leutbecher, M. *et al.* Stochastic representations of model uncertainties at ECMWF: State of the art and future vision. *Quarterly Journal of the Royal Meteorological Society* **143,** 2315–2339 (2017).

31. Christensen, H. *et al.* Simulating weather regimes: Impact of stochastic and perturbed parameter schemes in a simple atmospheric model. *Climate Dynamics* **44,** 2195–2214 (2015).

32. Davini, P. *et al.* The representation of winter Northern Hemisphere atmospheric blocking in ECMWF seasonal prediction systems. *Quarterly Journal of the Royal Meteorological Society* **147,** 1344–1363 (2021).

33. Davini, P. *et al.* Climate SPHINX: evaluating the impact of resolution and stochastic physics parameterisations in the EC-Earth global climate model. *Geoscientific Model Development* **10,** 1383–1402 (2017).

34. Donners, J. *et al.* Performance analysis of EC-EARTH 3.1. *Partnership for Advanced Computing in Europe White Paper, 26pp* (2012).

35. Döscher, R. *et al.* The EC-earth3 Earth system model for the climate model intercomparison project 6. *Geoscientific Model Development Discussions* **2021,** 1–90 (2021).

36. Palmer, T. N. *et al.* Stochastic parametrization and model uncertainty (2009).

37. Berner, J. *et al.* A spectral stochastic kinetic energy backscatter scheme and its impact on flow-dependent predictability in the ECMWF ensemble prediction system. *Journal of the Atmospheric Sciences* **66,** 603–626 (2009).

38. Shutts, G. A stochastic convective backscatter scheme for use in ensemble prediction systems. *Quarterly Journal of the Royal Meteorological Society* **141,** 2602–2616 (2015).

39. Hersbach, H. *et al.* The ERA5 global reanalysis. *Quarterly journal of the royal meteorological society* **146,** 1999–2049. doi:https://doi.org/10.1002/qj.3803 (2020).

40. Shutts, G. The propagation of eddies in diffluent jetstreams: Eddy vorticity forcing of 'blocking' flow fields. *Quarterly Journal of the Royal Meteorological Society* **109,** 737–761 (1983).

41. Nakamura, N. & Huang, C. S. Atmospheric blocking as a traffic jam in the jet stream. *Science* **361,** 42–47 (2018).

42. Tibaldi, S. & Molteni, F. On the operational predictability of blocking. *Tellus A* **42,** 343–365. doi:https://doi.org/10.1034/j.1600-0870.1990.t01-2-00003.x (1990).

43. Scherrer, S. C. *et al.* Two-dimensional indices of atmospheric blocking and their statistical relationship with winter climate patterns in the Euro-Atlantic region. *International journal of climatology* **26,** 233–250. doi:10.1002/joc.1250 (2006).

44. Davini, P. *et al.* Bidimensional diagnostics, variability, and trends of Northern Hemisphere blocking. *Journal of Climate* **25,** 6496–6509 (2012).

45. Barriopedro, D. *et al.* Application of blocking diagnosis methods to general circulation models. Part I: A novel detection scheme. *Climate dynamics* **35,** 1373–1391 (2010).

46. Lindzen, R. & Farrell, B. A simple approximate result for the maximum growth rate of baroclinic instabilities. *Journal of the atmospheric sciences* **37,** 1648–1654 (1980).

47. Paciorek, C. J. *et al.* Multiple indices of Northern Hemisphere cyclone activity, winters 1949–99. *Journal of Climate* **15,** 1573–1590 (2002).

48. Novak, L. *et al.* The life cycle of the North Atlantic storm track. *Journal of the Atmospheric Sciences* **72,** 821–833 (2015).

49. Scaife, A. A. *et al.* Atmospheric blocking and mean biases in climate models. *Journal of Climate* **23,** 6143–6152 (2010).

50. Scaife, A. A. *et al.* Improved Atlantic winter blocking in a climate model. *Geophysical Research Letters* **38** (2011).

51. Dima, I. M. *et al.* Tropical zonal momentum balance in the NCEP reanalyses. *Journal of the atmospheric sciences* **62,** 2499–2513 (2005).

52. Hartmann, D. L. *Global physical climatology* (Newnes, 2015).

53. Matsuno, T. Quasi-geostrophic motions in the equatorial area. *Journal of the Meteorological Society of Japan. Ser. II* **44,** 25–43 (1966).

54. Gill, A. E. Some simple solutions for heat-induced tropical circulation. *Quarterly Journal of the Royal Meteorological Society* **106,** 447–462 (1980).

55. Hoskins, B. J. & Karoly, D. J. The steady linear response of a spherical atmosphere to thermal and orographic forcing. *Journal of Atmospheric Sciences* **38,** 1179–1196 (1981).

56. Simmons, A. J. Tropical influences on stationary wave motion in middle and high latitudes. *Roy. Neth. Meteorol. Inst. On the Theory and Appl. of Simple Climate Models to the Probl. of Long Range Weather Prediction p 31-47(SEE N 83-18175 08-47)* (1982).

57. Jin, F. & Hoskins, B. J. The direct response to tropical heating in a baroclinic atmosphere. *Journal of the atmospheric sciences* **52,** 307–319 (1995).

58. Palmer, T. Towards the probabilistic Earth-system simulator: A vision for the future of climate and weather prediction. *Quarterly Journal of the Royal Meteorological Society* **138,** 841–861 (2012).

59. Deinhard, M. & Grams, C. M. Towards a process-oriented understanding of the impact of stochastic perturbations on the model climate. *EGUsphere* **2023,** 1–29 (2023).

60. Davini, P. *et al.* Orographic resolution driving the improvements associated with horizontal resolution increase in the Northern Hemisphere winter mid-latitudes. *Weather and Climate Dynamics* **3,** 535–553 (2022).

Chapter 3

Tracking summer Greenland blocking: the upstream pathway shapes historical extremes and future change

This research article has been submitted to a peer-reviewed journal. A pre-print is available at: https://arxiv.org/abs/2601.02032. The work has been conducted together with Jacob Maddison (University of Exeter) and Simona Bordoni (University of Trento).

3 TRACKING SUMMER GREENLAND BLOCKING: THE UPSTREAM PATHWAY SHAPES HISTORICAL EXTREMES AND FUTURE CHANGE

ABSTRACT

The representation and future evolution of summer Greenland atmospheric blocking is here investigated from a Lagrangian perspective using a novel python package *blocktrack*. By applying the blocktrack algorithm to ERA5 reanalysis and a CMIP6 model ensemble, we identify and track blocking events over Greenland, and obtain their trajectories, intensities, durations and wave-breaking characteristics. Two types of Greenland Blocking (GB) are identified in ERA5 via the Wave Breaking Index, respectively characterized by anticyclonic and cyclonic wave breaking. These correspond to the previously identified upstream and retrograding GBs. Upstream blocks, which originate in Northern Canada, exhibit stronger moisture transport before and during the blocking onset and higher temperature anomalies than retrograding blocks, which follow a east-to-west trajectory and originate in the Northern Atlantic. Our analyses show how the recent observed increase in the frequency of GB, particularly in 2012, is primarily driven by upstream blocks. CMIP6 models generally fail to capture the increase seen in observations and underestimate GB variability. Future projections under the SSP370 scenario show a decline in retrograding blocks but a possible increase in upstream blocks, depending on the detection index used. We discuss possible drivers of these changes, which include jet stream position shifts, increased frequency of high moisture transport events to the high latitudes and foehn wind events. By analyzing block trajectories, this study demonstrates how Lagrangian diagnostics can provide novel insights into the dynamics of blocking events over Greenland.

3.1 INTRODUCTION

The climate of Greenland and the dynamics of its ice sheet are of critical importance in the context of global warming due to their significant contribution to sea level rise and their role in the Atlantic Meridional Overturning Circulation (AMOC). If the Greenland ice sheet were to become unstable and initiate irreversible melting, the ocean level would rise by up to 7 meters over the next millennium [1], with severe impacts on coastal regions worldwide. Freshwater input into

the North Atlantic ocean would also alter high-latitude salinity, potentially disrupting the AMOC and the associated heat transport from low to high latitudes [2, 3]. Such disruption would have major consequences on Northern Hemisphere (NH) climate, particularly northern Europe [4, 5]. Between 2010 and 2020, Greenland has experienced exceptional episodes of surface melt and runoff, culminating in record-breaking melt years in 2012 and 2019 [6]. These extreme melt events occur predominantly during the summer months, when solar radiation is highest and surface energy input drives peak ice sheet melt. Understanding the atmospheric drivers of these anomalies is essential for improving projections of ice sheet mass balance and circulation responses to global warming.

Extreme temperatures and record ice melt in Greenland are strongly influenced by Greenland Blocking (GB) [7]. In general terms, atmospheric blocking refers to quasi stationary high-pressure systems that disrupt the typical zonal flow of the mid-latitude jet stream, especially in the NH [8, 9]. GB, specifically, is characterized by persistent high-pressure anomalies over or near Greenland [10] and plays a key role in modulating both the local weather of Greenland and the larger-scale circulation patterns across the North Atlantic region. In fact, GB variability is strongly anticorrelated with the North Atlantic Oscillation (NAO), the most prominent pattern of climate variability in the extratropical North Atlantic region [11–13].

The frequency of GB has been observed to increase during the first two decades of the 21st century, with very large anomalies around 2012 and 2019 coinciding with major melt years [14–16] and a decrease after 2020 [17, 18]. This suggests a link between the occurrence of blocking and anomalous heating and increased melting. Suggested mechanisms behind the observed increase include hemispheric-scale teleconnection patterns manifesting as a stationary Rossby wave with a zonal wave number-3 pattern [19], reductions in North American snow cover linked to Arctic Amplification [17], and sea surface temperature (SST) anomalies, particularly in association with the Atlantic Multidecadal Oscillation (AMO) [20]. Ultimately, these different mechanisms are believed to alter the climatological geopotential height west of Greenland, creating a stationary wave that promotes blocking over the region. Previous studies have also explored the role of precursor cyclones in advecting warm air over Greenland and amplifying blocking anticyclones leading to extreme blocking events [21]. Additionally, moisture advection into the Greenland region has been identified as an amplifier of blocking-induced ice melt by increasing rainfall onto the ice sheet [22, 23]. The co-occurrence of atmospheric rivers and foehn events over north-east Greenland have also been identified as precursor of extreme melt episodes by Mattingly *et al.* [24]. Finally, recent work by Maddison *et al.* [18] and Luu *et al.* [25] has shown that neither the CMIP6 large-ensemble simulations nor HIGHRESMIP models are able to reproduce the observed recent increase in GB frequency, suggesting that current models are missing an important factor governing GB variability. Despite extensive research on this topic, we still lack a definitive explanation for both the recent increase in GB events and the inability of climate models to capture it.

Some of the difficulties encountered in interpreting the recent summer blocking increase can be a consequence of the existing gaps in our understanding of GB. To address this issue, in a recent work Hauser *et al.* [26] have adopted a Lagrangian PV perspective to understand the contribution of barotropic dynamics, nonlinear wave-eddy interactions and of moist processes to GB onset and persistence. More specifically, moisture was shown to influence both the initiation and maintenance of GB through radiative effects and latent heat release, possibly explaining its longevity relative to blocking in other regions of the North Atlantic [26–28]. Beside investigating onset and maintenance mechanisms, Hauser *et al.* [26] have also classified GB into upstream and retrograding blocking regimes, two classes of blocks that differ in terms of onset pathway. The former originates upstream of Greenland while the latter follows a retrograding trajectory with respect to the flow. Given that moist diabatic processes act throughout the whole GB trajectory, they are often underestimated using Eulerian frameworks focusing only on local, rather than remote, processes [e.g., 29], motivating a greater reliance on Lagrangian approaches when studying GB dynamics.

Given the limitations associated with conventional Eulerian blocking definitions [26] and the recent GB observations, in this study we analyze the recent summer GB increase through a Lagrangian tracking algorithm, trying to understand whether the backtracking of geopotential height anomalies—and the inclusion and consideration of remote influences on blocking onset—can provide additional insights on the extreme ice-sheet melting that occurred in the past decades. Moreover, following the approach of Hauser *et al.* [26], we separately examine trends in upstream and retrograding blocks to assess whether either type is driving the recent increase in summer blocking frequency. We provide additional insights on the features of these two families of blocking by developing an original classification method based on the wave breaking characteristics.

The Lagrangian tracking framework used in this study is a python-based algorithm called "blocktrack", already illustrated and used in Filippucci *et al.* [30]. Thanks to its design, blocktrack enables detailed analyses of blocking trajectories duration, spatial extent, intensity and wave-breaking characteristics. Here, we first apply this algorithm to the ERA5 reanalysis dataset (1940–2024) and subsequently to a set of CMIP6 simulations, both for the historical and future periods. By analyzing the historical CMIP6 simulations we build on the previous work by Maddison *et al.* [18], who analyzed a similar ensemble, highlighting how CMIP6 and HIGHRESMIP models fail to capture the recent increase in summer Greenland blocking, as well as its variability. In this study we repeat a similar analysis integrating the separation into upstream and retrograding blocks. Moreover, we expand upon Maddison *et al.* [18] by analyzing future projections and interpreting projected blocking trends within the framework developed in this manuscript.

The paper is structured as follows: in Section 3.2 we present the data used, the methods adopted and we provide a detailed description of the Lagrangian tracking algorithm, in Section 3.3 we analyze ERA5 reanalysis data and in Section 3.4 we present the CMIP6 analysis, for both the historical and future runs. Lastly, in

Section 3.5, we discuss our main results.

3.2 METHODS

3.2.1 Data

The analyses presented in this paper are based on the ERA5 reanalysis [31] and an ensemble of models from the Coupled Model Intercomparison Project Phase 6 (CMIP6) [32].

ERA5 is used as an observationally constrained estimate of historical atmospheric blocking activity over Greenland from 1940 to 2023 during NH summer (June, July and August, hereafter JJA), using daily data at horizontal resolution of 2.5° × 2.5°. The geopotential height at 500 hPa and the 2-meter temperature are retrieved at a single level, while the meridional wind component and specific humidity are retrieved across nine pressure levels.

To evaluate how current climate models represent atmospheric blocking over Greenland, we use a large multi-model ensemble of historical coupled model simulations from CMIP6. Specifically, we analyze the geopotential height at 500hPa retrieved from 70 ensemble members derived from 10 different models, each run in multiple configurations. All ensemble members are weighted equally, so models with more members–such as UKESM–have a proportionally greater influence on the results.

For future projections, we rely on a smaller ensemble from the same set of 10 CMIP6 models, totaling 29 ensemble members. While a large ensemble is essential for quantifying internal variability in the historical period, a smaller ensemble size is sufficient to estimate future forced trends. The future scenario considered here is the SSP3-7.0, a high emission Shared Socioeconomic Pathway leading to a radiative forcing of about 7 W/m^2 by 2100. A detailed list of the models used and the corresponding number of ensemble members is provided in Appendix A2.

3.2.2 Blocktrack

The analysis presented in this paper uses the novel Lagrangian tracking algorithm "blocktrack" first presented in Filippucci *et al.* [30] and released on Github as Filippucci [33]. This tracking algorithm is a flexible framework that allows for the detection of blocks through multiple blocking indices, the computation and characterisation of block trajectories and the application of non-destructive filters to subsample detected blocking events according to user-defined criteria. A detailed description of each aspect of the algorithm is provided below.

The first step is atmospheric blocking detection, which identifies blocked grid points in a gridded dataset through the analysis of daily geopotential height at 500hPa (Z500). Two indices—hereafter referred to as instantaneous blocking indices (IBI)—are adopted in this study: the geopotential height gradient reversal index (DAV), based on Davini *et al.* [34], and the geopotential height anomaly

index (GHA), adapted from Woollings *et al.* [35], in turn similar to index introduced by Dole & Gordon [36]. The use of multiple indices reflects the diverse manifestations of GB, which can appear as persistent omega-shaped ridges or as high-amplitude Rossby waves breaking in a clockwise (anticyclonic) or anticlockwise (cyclonic) direction. As different indices are sensitive to different blocking structures or stages, combining complementary approaches has become standard practice to ensure robust detection and interpretation [35].

In contrast with the work by Hauser *et al.* [26], who adopted a PV-based index, here we use geopotential height-based indices. While this choice is primarily motivated by the availability of the variable in our datasets, it also provides an opportunity to assess whether different blocking indices yield a consistent separation between upstream and retrograding blocks.

The DAV index identifies grid points where a reversal of the meridional geopotential height gradient occurs, making it particularly effective for detecting Rossby wave breaking events. More specifically, for each grid-point the northward ($GHGN$) and southward Z500 gradient ($GHGS$) are computed as:

$$GHGN(\phi_0, \lambda_0) = \frac{Z500(\phi_N, \lambda_0) - Z500(\phi_0, \lambda_0)}{\phi_N - \phi_0} \tag{3.1}$$

$$GHGS(\phi_0, \lambda_0) = \frac{Z500(\phi_0, \lambda_0) - Z500(\phi_S, \lambda_0)}{\phi_0 - \phi_S} \tag{3.2}$$

where λ_0 and ϕ_0 represent the grid point longitude and latitude, respectively; ϕ_0 and λ_0 range from 30° to 75°N and 0 to 360°E, respectively; $\phi_s = \phi_0 - 15$ lat and $\phi_N = \phi_0 + 15$ lat. A grid point of coordinates (λ_0, ϕ_0) is flagged as blocked if:

$$GHGS(\phi_0, \lambda_0) > 0;\ GHGN(\phi_0, \lambda_0) < -10\ \mathrm{m\,lat^{-1}} \tag{3.3}$$

We adopt the correction of Tyrlis *et al.* [37] that relaxes the northward gradient threshold to:

$$GHGN(\phi_0, \lambda_0) < 0\ \mathrm{m\,lat^{-1}} \tag{3.4}$$

This modification is more appropriate for high-latitude blocking events, where a strong jet on the poleward side of the block is less common.

In contrast, the GHA index identifies blocked grid points where daily Z500 anomalies, computed relative to a 90-day running mean, are larger than 1.26σ of the Z500 anomaly distribution. The threshold has been chosen as the 90th percentile of a normal distribution. This probability distribution is calculated over the latitudinal band from 45°N to 80°N, and the resulting threshold—evolving in time following the 90-day window—is applied uniformly to all grid points. As a result, the index is well suited for detecting amplified Rossby waves, ridges, and omega blocks.

Regardless of the IBI used, the output is a 3D (time, latitude, longitude) diagnostic matrix where each grid point is flagged "blocked" or "not blocked". Blocking events are then tracked over time in two steps: (i) blocked areas are identified

independently for each day, and (ii) blocked areas on consecutive days are considered part of the same event if they share at least 50% of grid points with the previous day's area.

During event tracking, several characteristics are computed for each blocking event: area (in km^2) of the block on each day, center-of-mass trajectory, center-of-mass daily displacement, intensity, wave-breaking index (hereafter WBI) and duration. The intensity is calculated as the Z500 anomaly relative to a 90-day mean centered on the block day and averaged over the blocked area. The WBI, following Davini *et al.* [34], is defined as:

$$WBI(\lambda_0, \phi_0) = \frac{Z_{500}(\lambda_W, \phi_S + 7.5) - Z_{500}(\lambda_E, \phi_S + 7.5)}{\lambda_W - \lambda_E} \tag{3.5}$$

where ϕ_S is defined as in the blocking index and $\lambda_W = \lambda_0 - 7.5$ and $\lambda_E = \lambda_0 + 7.5$. Negative (positive) WBI values identify anticyclonic (cyclonic) wave breaking. The WBI index is then averaged over the blocked area and a single value is assigned to each blocked day. Note that in the case of a ridge or an omega block, WBI values lie close to zero. As a result, a tracked diagnostic matrix is produced in which each blocked grid point is labeled according to a unique blocking event. Moreover, a python dictionary stores all block characteristics, providing a flexible dataset for analysis.

The final step is filtering events. Depending on the chosen IBI, several filters can be applied to retain only events on the synoptic scale that persist for several days. In this study we use the following filters: (i) for DAV, a minimum average area of 5×10^5 km^2 and a minimum persistence of 5 days; (ii) for GHA, a minimum area of 2×10^6 km^2 and a minimum persistence of 5 days. The thresholds were selected to ensure consistency with previous studies [18, 34, 35] and reflect the tendency of the GHA index to detect larger blocked areas than the DAV index. These filters are applied non-destructively: a new diagnostic matrix is created in which events failing the criteria are excluded, without recomputing the tracking. This approach allows multiple filtering options to be tested easily and facilitates sensitivity analyses. We also verified that moderate threshold changes do not significantly affect the results.

The algorithm is computationally efficient, requiring approximately fifteen minutes to track all blocking events in the ERA5 dataset (84 years, daily, 2.5°x2.5° horizontal spatial resolution) on a regular laptop (Apple M2 processor). Lastly, we mention that other indices are implemented in the "blocktrack" algorithm and are available in the Github repository even though they are not used in this study.

3.2.3 Frequency and composites analysis

Once the blocking events are detected, we isolate those occurring over Greenland. To do so we define a box around Greenland, ranging from 70W–20W and 60N–80N, and select the events that have at least one grid point within this region for at least 3 consecutive days. This generates a list of GB events, along with their

center-of-mass trajectories, WBI, average spatial extent, and other characteristics. For each blocking event, a single representative value of WBI and area is obtained by averaging over the event's full life cycle.

The blocking composites are computed in a block-centered reference frame, i.e. they are Lagrangian composites. More specifically, for each blocking event, we extract the 2D field of interest (e.g., 2-m temperature T2m, integrated vapor transport IVT and Z500) within a box centered 10 degrees south of the event's center of mass and spanning 50 degrees of latitude and 90 degrees of longitude. The southward offset of the composite has been introduced to better highlight the equatorward features of the blocking system, otherwise not included in the composite. The average of these event-centered fields defines the Lagrangian composite. This approach allows us to capture the characteristics and spatial pattern of blocks, even when events occur at different geographical locations. We also compute composites across the different stages of the blocking life cycle. For days preceding the identified blocking onset, the daily composite field is computed by centering the box on the initial center-of-mass position of the block trajectory.

In the following sections we present composites of Z500, T2m and IVT, defined as in Barrett *et al.* [23]:

$$\text{IVT} = \frac{1}{g}\int_{1000\text{ hPa}}^{200\text{ hPa}} qv\,dp \tag{3.6}$$

where g is the gravitational acceleration on Earth, q is the specific humidity, v the meridional component of wind and p is the vertical pressure coordinate. The meridional velocity and the specific humidity are available at daily temporal spacing and on nine pressure levels. When plotting the composites of IVT we show its standardized anomaly $[IVT^*]^b_\sigma$ computed as

$$[IVT^*]^b_\sigma = \frac{[IVT^*]^b}{\sigma_{IVT}} \tag{3.7}$$

where $[IVT^*]^b$ is the composite anomaly obtained by averaging the IVT anomaly over blocking days and σ_{IVT} is the standard deviation of the IVT field. The standardized anomaly is useful for highlighting regions where IVT anomalies exceed typical variability.

Lastly, the blocking frequency time series presented below are computed by inspecting the box centered over Greenland (70W–20W and 60N–75N). For each day, we define the blocking frequency as:

$$F_d = N_{blocked}/N_{tot} \tag{3.8}$$

where F_d is the daily frequency, $N_{blocked}$ and N_{tot} are, respectively, the number of blocked grid points belonging to the previously identified set of Greenland blocks and the total number of grid points contained in the inspected area. To obtain a time series we compute the monthly mean of the daily frequency and its standardized anomaly, defined as:

$$A_\sigma = \frac{F_m - < F_m >}{\sigma_{F_m}} \tag{3.9}$$

where F_m is the monthly blocking frequency, and $< F_m >$ and σ_{F_m} are, respectively, the climatological mean and standard deviation of the monthly values for the period 1950–2000. When analyzing CMIP6 future projections, the mean and standard deviation are computed over the entire available period (2015–2100). We therefore refer to this quantity as 'normalized blocking frequency' rather than 'standardized anomaly'. Both the standardized anomaly and the normalized blocking frequency are useful for comparing model variability while removing model biases in climatological blocking frequency, which can vary considerably among models [38]. Finally, we smooth the time series by applying a 10 year running average.

3.3 CHARACTERISTICS OF SUMMER GREENLAND BLOCKING IN REANALYSIS

3.3.1 Blocking events trajectories

Fig. 3.1 shows the center-of-mass positions of the blocking events crossing Greenland in ERA5 for JJA. The two panels present the center of mass derived using the DAV and GHA indices and tracked throughout the blocking life cycle, including days prior to the blocks' arrival over Greenland.

The DAV index is detecting more blocking events compared to the GHA index, meaning that not all the reversal of the meridional gradient of geopotential height are associated to a large and persistent geopotential height anomaly. The events detected through the DAV index are more localized over Greenland throughout their life cycle (Fig. 3.1a), whereas those detected using the GHA index can travel longer distances (note that the map projection exaggerates distances at higher latitudes) and tend to form two clusters: one over northern Europe and one over northeastern Canada (Fig. 3.1b). This difference reflects the design of the two indices: GHA tends to detect earlier stages of blocking onset compared to DAV, since the ridge typically develops before Rossby wave breaking [39]. Moreover, the GHA index detects larger blocked areas as individual blocking systems, increasing the likelihood of event merging and splitting.

As shown in Fig. 3.2, events detected using the GHA index are, on average, about twice as large in area and tend to last longer than those detected using the DAV index. These characteristics are consistent with the broader center-of-mass distribution observed in Figure 3.1. Greenland blocking events are associated with both positive and negative values of the WBI index (Fig 3.2d), indicating that wave breaking during GB events can be both cyclonic and anticyclonic. This holds true for both indices.

Moreover, the two hotspots of block trajectory frequency, one east and one west of Greenland, identified by the GHA index confirm the finding from Hauser *et al.* [26] that GB events can originate from two preferred locations. Hereafter we

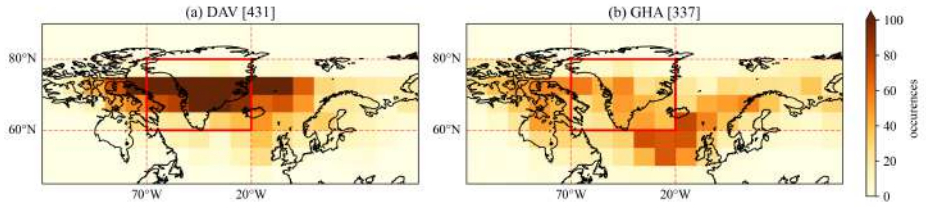

Figure 3.1: GB events center-of-mass bidimensional distribution from ERA5 renalaysis (JJA). The two-dimensional histograms use 10°lon × 5°lat bins, and the value in each bin indicates how many times the center of mass of a GB event falls within that area. Panel a refers to the DAV index while panel b refers to the GHA index. The number of detected events crossing Greenland is shown in square brackets in each panel title.

adopt their same nomenclature, referring to blocking events following a east-to-west trajectory as ”retrograding" blocks and those originating west of Greenland as ”upstream" blocks.

3.3.2 Composite analysis

We now separate the GB events into upstream and retrograding types and analyze their respective characteristics. In order to effectively separate blocking events in the two classes for both indices, we need to find an alternative method compared to Hauser *et al.* [26], as in the DAV index case we do not find a clear separation into two geographical clusters. We therefore need to rely on the wave breaking characteristics of blocks, which we find to be linked to the onset region.

The first column of Fig. S3.7 shows the center-of-mass density histograms of GB events for these two categories, with blocks labeled based on the sign of their WBI. In Fig. S3.7b, based on the GHA index, it is evident that the WBI effectively distinguishes the two clusters of blocking events mentioned in the previous section: upstream blocks, originating west of Greenland, are associated with WBI< 0 (anticyclonic breaking), whereas retrograding blocks, originating east of Greenland, are associated with WBI> 0 (cyclonic breaking). We therefore adopt the same nomenclature for the blocking events detected through the DAV index, even though the spatial separation is less pronounced, because the WBI provides a consistent physical basis for classification. As stated in the previous sections, the GHA index captures earlier stages of the blocking life-cycle as expected, leading to a clearer separation into retrograding and upstream clusters. Lastly, a small secondary cluster of upstream GB centers of mass, identified by the GHA index

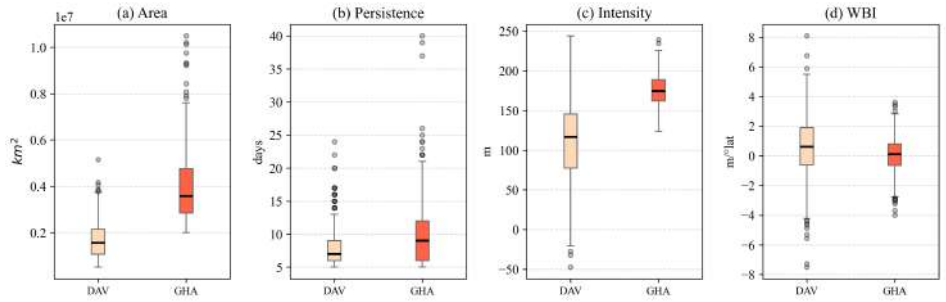

Figure 3.2: Box plots of Greenland blocking event characteristics in ERA5 reanalysis (JJA). Panel a) shows event area [km^2], panel b) shows event persistence [days], panel c) shows event intensity [m] and panel d) shows event WBI [m/lat]. Orange and light orange indicate blocking events detected with GHA index and the DAV index, respectively. Black circles are outlier events.

in Figure S3.7b, is located in the North West Atlantic near the British Isles. These events likely correspond to anticyclonic Rossby wave breaking in northwestern Europe, which subsequently propagate over Greenland and are therefore dynamically distinct from the main upstream GB cluster. We excluded these events by reducing the size of the detection box (not shown), but this had little impact on the results of the present study. Since the detection box reduction implies the exclusion of both this secondary cluster and a large fraction of the upstream blocks cluster, for the final analysis, we retained the larger box to enhance the statistical significance of our findings.

The second column of Fig. S3.7 (both panels a and b) shows the 2m-temperature and 500hPa-geopotential height composites of the-so identified blocking clusters. The Z500 contours clearly depict the Rossby wave breaking pattern associated with each block type in both panels a and b. As expected, for $WBI < 0$ ($WBI > 0$) Rossby wave breaking occurs anticyclonically (cyclonically). For blocking events detected with the DAV index (Panel a) the 2m temperature anomalies exhibit a dipole pattern, with warm anomalies on the northern flank and cold anomalies on the southern flank, consistent with the ridge-trough circulation of the block. These anomalies arise from a combination of meridional advection of warm/cold air and radiative effects. In contrast, for blocks detected using the GHA index (Fig. S3.7b) the dipole pattern is weaker, if not absent, and positive temperature anomalies are larger than in Fig. S3.7a. These differences reflect the design of the indices: GHA captures positive geopotential height anomalies and earlier stages of block development, while DAV does not require strong positive geopotential height anomalies and is often linked to weaker anticyclonic circulation. This distinction is also consistent with the differences in mean intensity shown in Fig. 3.2.

Moisture transport plays a key role in the radiative and advective processes associated with blocking onset and impacts [22, 26, 28, 40]. To highlight this effect,

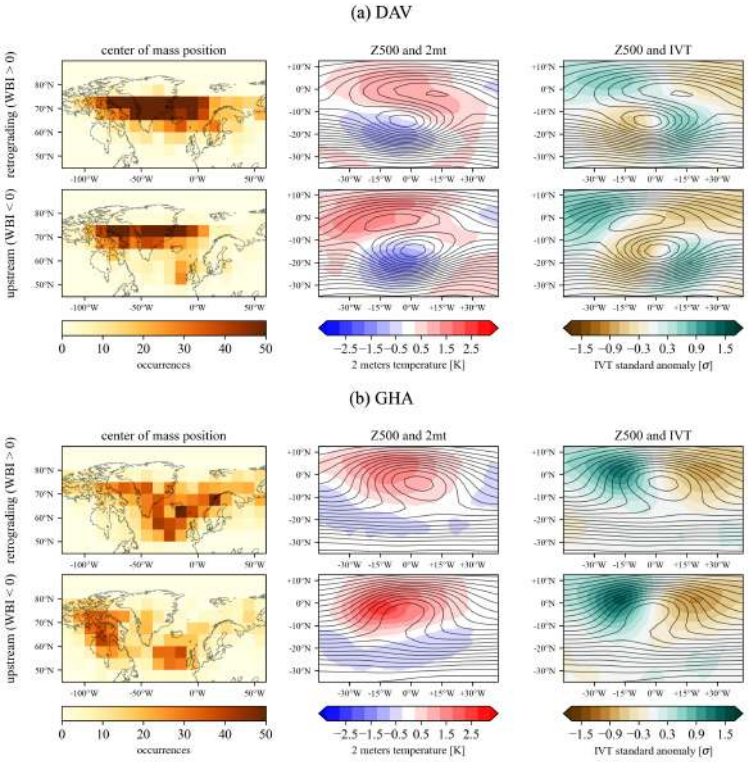

Figure 3.3: Composites and center of mass positions of retrograding and upstream blocking events over Greenland from ERA5 reanalysis (JJA). The center-of-mass position plots are 2D histograms with 10°lon × 5°lat bins, showing how often the center of mass of an upstream or retrograding block falls within each bin. Composite plots are plotted in the reference system of the block's center of mass (e.g. x axis represents relative longitude). Black contours represent the 500hPa geopotential height composite (Z500). Contours are plotted every $40m$***. Shadings refer to the composite anomaly of temperature above the surface (2 meters temperature - or 2mt [K]) and to the composite standard anomaly of IVT (see methods for further details). Anomalies have been computed with respect to the seasonal mean. A Student's t-test was performed to assess the significance of the plotted anomalies, with all shaded contours significant at the 95% confidence level. Panel a) showcases blocking events detected through the DAV index and panel b) showcases blocking events detected through the GHA index.***

we plot composites of the IVT standardized anomaly (see the Methods section for further details). In both DAV (panel A) and GHA (panel B) composites, the IVT standard anomaly closely follows the meridional wind pattern, with negative anomalies upstream and positive anomalies downstream of the block. This pattern is consistent with the geostrophic approximation, where Z500 contours represent the streamfunction of the horizontal flow. Comparing the two families of blocking we find that the IVT standard anomaly is generally stronger for upstream blocks than for retrograding blocks in both panels a and b. Moreover, anomalies are particularly large northeast of the block, an area identified by previous work as crucial for blocking intensification due to moisture advection [22]. However, moisture advection alone is not sufficient to drive blocking amplification — latent heat release by ascending air streams must also occur. As a proxy for this process, we examine precipitation composites during blocked days, presented in the Supplementary material (Figure S7), which reveals enhanced precipitation to the northwest of upstream blocks, consistent with the increased meridional water vapour transport identified above. Notably, the synoptic circulation associated with upstream blocks intensifies the advection of moisture toward north-east, a configuration compatible with the development of foehn winds north east of Greenland ice-sheet, a phenomenon that Mattingly *et al.* [24] associated to extreme ice melt. We will return on this point in the Conclusions.

We further evaluated if upstream and retrograding blocks differ systematically in area, persistence, or intensity, for both indices (not shown). No statistically significant differences were found, likely because the variability within each block type is large relative to the differences between types (see the boxplot in Fig. 3.2).

3.3.3 Time evolution of Greenland blocking

In Fig. 3.4 we show composites of upstream and retrograding blocks over Greenland during different stages of their life cycles, as detected by the GHA index. See Supplementary Material for a similar analysis based on the DAV index showing similar features. Again, we see that temperature anomalies are larger for the upstream blocks. In both cases, the rise in temperatures starts before the blocking when the ridge structure starts developing. This feature is particularly evident for the upstream blocks. IVT standard anomalies are again larger for upstream blocks than retrograding blocks, especially before and during the blocking onset. This fact suggests a link between the fast temperature rise and the moisture advection, which likely plays a role in the blocking onset.

Seasonal analyses reveal pronounced variations in the relative frequency of upstream and retrograding blocks. Upstream blocks are less frequent in winter, reflected in a shift of the WBI distribution toward positive values (see Appendix and Fig. A3.1 for a more detailed analysis). This suggests a strong seasonal dependence in the underlying blocking dynamics, likely linked to the poleward migration of the polar jet stream in summer and its equatorward shift in winter [41], as well as to differences in insolation and the considerably different ocean surface energy

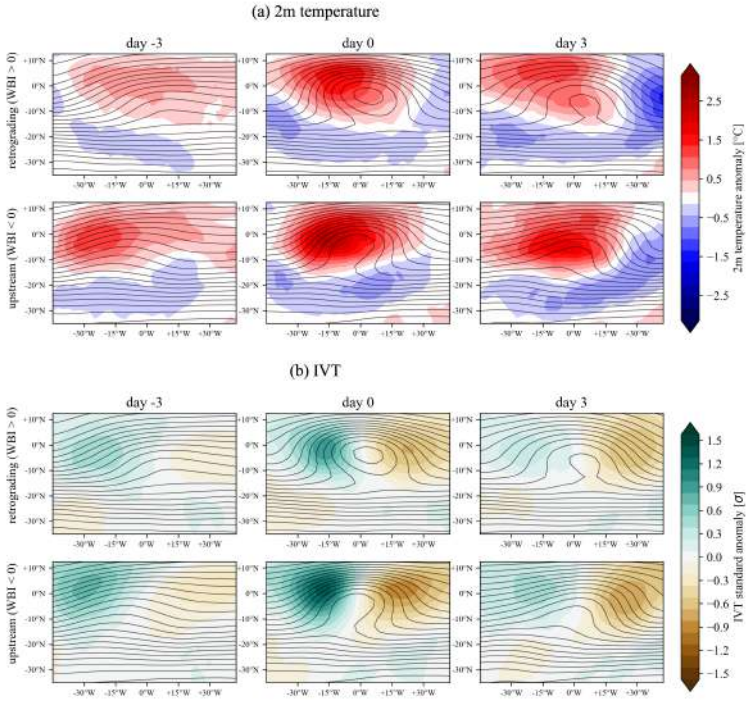

Figure 3.4: Composites of the time evolution of retrograding and upstream blocking events over Greenland from ERA5 reanalysis (JJA) detected through the GHA index. Composite plots are plotted in the reference system of the block's center of mass. Black contours represent the 500hPa geopotential height composite (Z500). Contours are plotted every $40m$***. Shadings refer to the composite anomaly of temperature above the surface (2 meters temperature - or 2mt*** $[K]$***) (panel A) and to the composite standard anomaly of IVT (see methods for further details) (panel B). Anomalies have been computed with respect to the seasonal mean. A Student's t-test was performed to assess the significance of the plotted anomalies, with all shaded contours significant at the 95% confidence level.***

balance around Greenland during summer. It has been shown that the position and strength of upper-level winds and their interaction with orography is crucial for setting the frequency and location of blocking onset [42–44]. The seasonal migration of the polar jet stream toward Greenland's latitudes together with the fact that the Greenland ice dome can reach altitudes of 3200 m [45] is therefore likely responsible (or partially responsible) for the seasonal variations of Greenland blocking. Moreover, the separation into upstream and retrograding blocks may be facilitated by Greenland orography, that may interact with the low level flow by altering the evolution of the synoptic flow (for example, via latent heat release by ascending air motion or lee cyclogenesis). Regarding this latter mechanism, the presence (or lack thereof) of sea ice over the waters around Greenland may play a crucial role, influencing the moisture exchange between atmosphere and ocean. We will return to this point in the Conclusions section.

To summarize, we find that Greenland blocking tends to occur via two distinct pathways, termed upstream and retrograding following Hauser *et al.* [26], which feature distinct characteristics. Upstream blocks, originating in Northern Canada and associated with anticyclonic Rossby wave breaking, are linked to stronger temperature anomalies compared to retrograding blocks, originating in Northern Europe and associated with cyclonic Rossby wave breaking. Importantly, upstream blocks are accompanied by stronger meridional moisture fluxes, which have been argued by previous work to play an important contribution to both blocking onset and amplification.

3.4 TRENDS IN REANALYSIS AND CMIP6 MODELS

3.4.1 ERA5 and CMIP6 historical runs

The timeseries of summer blocking frequency anomaly from ERA5 and from an ensemble of CMIP6 models is shown in Fig.3.5. The anomaly is computed by taking the monthly blocking frequency for each model/reanalysis product, subtracting the mean, dividing by its standard deviation and ultimately performing a 10-years running mean (for further details see the Methods section).

Both DAV and GHA identify an increase in GB frequency in the first two decades of the 21st century in ERA5 (Fig.3.5a-d), with a peak in August 2012 for DAV and June 2013 for GHA (not shown). Even though some simulations reach a similar or even higher blocking anomaly, it is evident how the ERA5 maximum sits at the upper margin of the anomaly distribution of the model ensemble for both indices, as previously identified by Hanna *et al.* [15] and Maddison *et al.* [18]. We now construct similar time series for upstream and retrograding blocking separately (Fig. 3.5b-f). This separation highlights an important and so far unreported result: the largest contribution to the recent summer blocking frequency increase comes from upstream blocks, with the largest increase occurring in the second decade of the 21st century (Fig. 3.5c, f). While true for both indices, this trend is more evident in the DAV index-based time series.

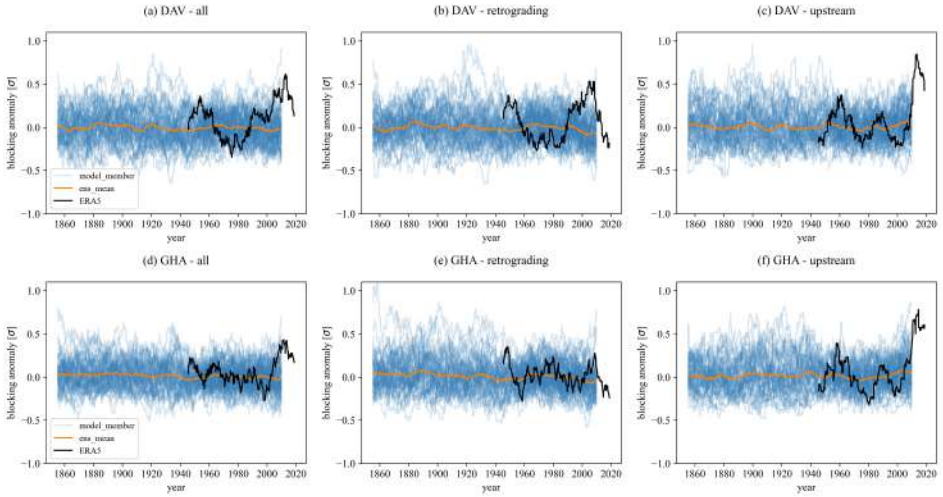

Figure 3.5: Summer (JJA) blocking standard anomaly time series (see the Methods section for further details on its definition). In all panels black lines refer to ERA5 reanalysis dataset, blue lines refer to CMIP6 ensemble members and orange lines refer to the ensemble average. The top row (a–c) shows blocking anomalies detected through the DAV index, while the bottom row (d–f) shows anomalies detected through the GHA index. The left column (a,d) refers to all blocking events crossing Greenland, the center column (b,e) refers to retrograding blocks and the right column (c,f) refers to upstream blocks.

In Fig.3.5 we analyze standardized anomalies to highlight trends and variability. However, because the mean is subtracted in this process, this figure does not reveal whether the climatological partitioning of upstream versus retrograding blocks is well represented by the CMIP6 models. A separate analysis performed through the absolute frequency rather than blocking anomaly reveals that CMIP6 models do capture well the separation into upstream and retrograding summer blocks in the 1950-2000 reference period (see the Supplementary Material). Approximately one third of the blocks are classified as 'upstream' and two thirds as 'retrograding' for both CMIP6 models and reanalysis, even though the absolute frequency is slightly underestimated by the CMIP6 models.

To quantify the magnitude of the recent observed peak, we compare the maximum blocking frequency anomaly in ERA5 against the distribution of maxima from the CMIP6 ensemble.

To obtain the CMIP6 distribution of maxima, for each of the 108 simulations we extract the maximum anomaly occurring within an 84-year time window (1930–2014), a time span chosen to match the ERA5 record length (1940–2024). This is done independently for the total, retrograding, and upstream blocking time series, with the resulting distributions of model maxima based on both DAV and GHA indices plotted in Fig. 3.6.

For the total blocking frequency (Fig. 3.6a,d), the recent ERA5 maximum lies above the median (50th percentile) of the CMIP6 distribution, indicating that the reanalysis exhibits larger blocking anomalies than most models. This is especially evident for the DAV index (91.4th percentile), and holds true for the GHA index (67.1th percentile), confirming Maddison *et al.* [18] results.

We then analyze the composition of the recent ERA5 blocking anomaly maximum, separating the contributions from upstream and retrograding blocks (Fig. 3.6b,e,c,f). This is done by inspecting the upstream and retrograding blocking frequency time series in the same month of the observed blocking frequency maximum (August 2012 for the DAV index and June 2013 for the GHA index). Note that the monthly time series is smoothed by applying a 10-years running mean (for further details see the Methods section). Crucially, while retrograding blocks do not exhibit notable anomalies during the observed ERA5 peak, which falls well below the typical model maxima, a very high value of upstream block frequency anomaly is observed for both the DAV and GHA indices. For the DAV index, the ERA5 upstream blocking anomaly is overcome by just 1 of the 70 simulations composing the CMIP6 ensemble (98.6th percentile), implying that CMIP6 models likely underestimate the variability of upstream blocking. Results are consistent for the GHA index, where the percentile value remains high (90th percentile), confirming that the recent increase in GB is indeed driven by a period of extreme upstream blocking frequency.

Finally, we assess whether the physical characteristics of upstream and retrograding blocks are correctly captured by CMIP6 models. By comparing the distributions of center-of-mass position, area, persistence, WBI, and intensity between the CMIP6 ensemble and ERA5, we find that the models reproduce the observed blocking features with high fidelity (not shown). This is especially true for the DAV index, for which no appreciable differences are found. For the GHA index, however, the models slightly underestimate the persistence and intensity of both block types. A complete set of characteristics histograms is provided in the Supplementary Material.

We do not present composite plots of upstream and retrograding blocks for the CMIP6 ensemble, as a detailed model-by-model composite analysis is impractical for the large ensemble size and falls outside the scope of this paper. However, the fact that the blocking characteristics are well captured gives us confidence that the fundamental processes driving the onset and maintenance of both upstream and retrograding blocks are well represented. This conclusions is further supported by results in Luu *et al.* [25], who analyzed a smaller subset of CMIP6 and HIGHRESMIP models. They found that while models fail to capture the recent increase in frequency, they reproduce the spatial structure and features of blocking reasonably well.

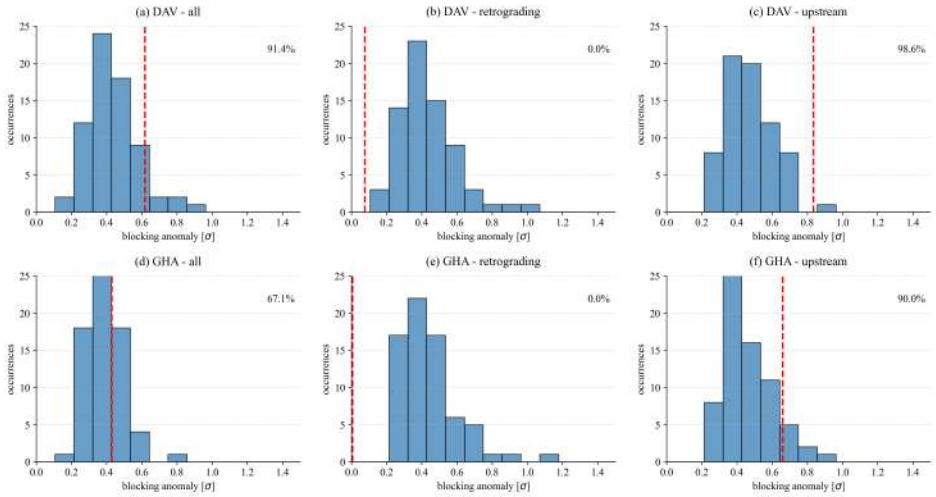

Figure 3.6: Distributions of frequency maxima in the CMIP6 models ensemble and comparison with the recent Greenland blocking increase in ERA5. The blue histograms show the distribution of the all-time maximum anomaly found in each model's 84-year window. The vertical red line represents the recent ERA5 summer Greenland blocking maximum. For the upstream and retrograding panels, the ERA5 line represents the anomaly value observed during the month of the total blocking maximum. In the bottom right of each plot we show the percentile corresponding to the ERA5 frequency value. Note that the distribution maxima and the ERA5 maximum have been computed taking into account the frequency time-series smoothed through a 10 years rolling mean. Top row (a–c) shows the analysis conducted with the DAV index, while the bottom row (d–f) shows the analysis based on the GHA index. The left column (a,d) refers to all blocking events crossing Greenland, the center column (b,e) refers to retrograding blocks and the right column (c,f) refers to upstream blocks

3.4.2 CMIP6 future projections

In Fig. 3.7, we present projected future trends in normalized summer GB frequency. The normalized blocking frequency is calculated similarly to the blocking anomaly, except that the standard deviation and mean are derived over the entire simulation period (2015–2100) (see Methods for details).

Fig. 3.7(a,d) show the projected evolution of total normalized blocking frequency over Greenland in summer, as computed using the DAV and GHA indices. A clear decreasing trend emerges when using the DAV index (Fig. 3.7a); the GHA index (Fig. 3.7d) instead does not exhibit any significant change over time. The trend significance is evaluated by comparing the slope of the least squares linear regression with its associated error; we consider it significant when the slope's magnitude exceeds twice the standard error (i.e., lies outside the 2σ range). These projections provide a useful comparison to Delhasse *et al.* [46] (hereafter D21), who analyzed future projections of summer Greenland blocking in a CMIP6 model ensemble. Our analysis diverges from D21 in two key aspects: first, we employ the SSP3-7.0 scenario (versus SSP5-8.5 in D21); second, while D21 used a GBI based on average Z500, we analyze trends using both the DAV and the GHA indices.

Discriminating the total blocking signal into upstream and retrograding components reveals distinct and so-far unreported dynamical trends. The projected decline in total GB frequency is driven primarily by a significant reduction in retrograding blocks (Fig. 3.7b,e). While this reduction is captured by both indices, it is most pronounced in the DAV index (Fig. 3.7b). In contrast, projections for upstream blocking differ between the two definitions (Fig. 3.7c,f). The GHA index indicates a marked increase in upstream blocking–consistent with recent anomalies in reanalysis–whereas the DAV index shows no significant trend. This explains why the total GHA frequency remains steady: the projected rise in upstream blocks effectively compensates for the reduction in retrograding blocks. Such compensation is not seen in the DAV index.

In summary, we find another important and so-far unreported result: the projected decrease of atmospheric blocking frequency (already identified by D21) can be attributed to retrograding blocks, while upstream blocks remain constant or increase, depending on the index used.

Lastly, we compare the features of GB events (persistence, area, WBI and intensity) between historical simulations and future projections (not shown). For both indices we find a small shift of the WBI distribution toward negative values in the future projections, coherent with a decrease of retrograding blocks and an increase of upstream blocks. Other characteristics remain relatively unchanged. Please see the associated histograms in the Supplementary Material.

3.5 CONCLUSIONS

In this study, we have analyzed the characteristics, historical trends, and future projections of summer GB using a novel Lagrangian framework applied to the

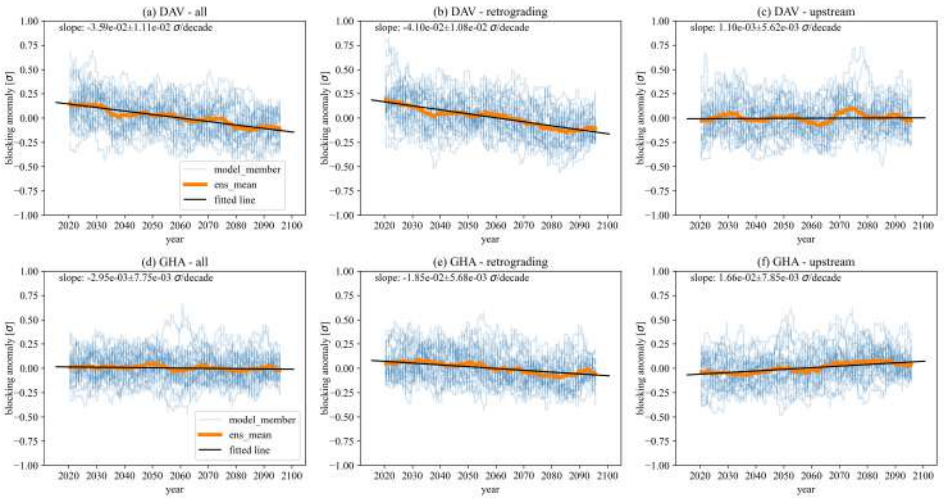

Figure 3.7: Future blocking standard anomaly time-series (see the Methods section for further details on its definition). In all panels blue lines refer to CMIP6 ensemble members, orange lines refer to the ensemble average and the black lines refer to the linear regression of the ensemble average. On top of each plot we report the linear regression parameters. Row (a–c) shows blocking anomalies detected through the DAV index, while row (d–f) shows anomalies detected through the GHA index. Column (a,d) refers to all the blocking events crossing Greenland, column (b,e) refers to retrograding blocks and column (c,f) refers to upstream blocks.

ERA5 reanalysis and an ensemble of CMIP6 models.

First, we examined the geographical distribution, trajectories and characteristics of GB events. We found that GB can originate through both anticyclonic and cyclonic Rossby wave breaking. This distinction if found to be associated with two main categories of GB: retrograding blocks, typically linked to cyclonic wave breaking and propagating from northern Europe, and upstream blocks, associated with anticyclonic wave breaking and originating in northeastern Canada. The geographical separation between these two categories is especially clear when using an anomaly-based blocking index, such as GHA, which better captures the earlier stages of the blocking life cycle and diagnoses events with larger spatial extent. A similar separation has been previously adopted by Hauser *et al.* [26], who first introduced the term 'upstream' and 'retrograding' blocks. However, while Hauser *et al.* [26] separate events based on the geometric center of mass position prior to onset, here this classification naturally emerges from the mean WBI value during the blocking life cycle.

To further investigate the nature of these blocks, we constructed Lagrangian composites of 2-meter temperature, Z500, and IVT for both retrograding and upstream blocks. Regardless of the blocking index used, we find that upstream blocks are typically associated with stronger temperature anomalies and enhanced meridional moisture transport compared to retrograding blocks. Notably, these thermodynamic anomalies begin developing up to three days before the blocking onset, suggesting a critical preconditioning role of moisture advection. Moreover, composite plots of the total precipitation during and before blocking onset show similar anomalies (see Appendix), implying latent heat release by the advected moist air masses. These results agree with previous studies by Pfahl *et al.* [28] and Hauser *et al.* [26], which highlighted the influence of latent heat and moist processes on blocking formation and persistence. Specifically, Pfahl *et al.* [28] argue that latent heat release associated with the upward transport of air from low levels contributes significantly to the upper-troposphere blocking anticyclone. Consequently, changes in atmospheric moisture content of the atmosphere in a warmer climate are crucial for assessing future blocking trends. Similarly, Hauser *et al.* [26] found that the amplification of Greenland blocking through moist processes occurs earlier in upstream blocks than in retrograding blocks, suggesting a more dominant role of moisture in upstream blocks development. Our composite analysis confirms these findings, revealing that thermodynamic anomalies and high-latitude moisture advection develop several days prior to the onset of upstream blocking events.

Importantly, our analysis shows that the observed increase in Greenland blocking frequency during the early 21st century is primarily driven by an increase in upstream blocks. This is a novel result, although recent literature has increasingly emphasized the importance of processes occurring west of Greenland. For instance, Preece *et al.* [17] identified North American snow cover spring anomalies and Arctic Amplification as key drivers of early summer Greenland blocking anomalies, while Beckmann *et al.* [20] noted that the Atlantic Multidecadal Variability and Arctic Amplification can alter the Labrador sea surface temperature,

thereby affecting local atmospheric circulation. Moreover, Beckmann *et al.* [20] confirmed the findings of Preece *et al.* [17] regarding the crucial role of spring snow cover in Northern Canada. These phenomena can induce warm temperature anomalies west of Greenland, triggering a stationary Rossby wave that favors the anchoring of eastward propagating ridges over Greenland, consistent with our findings.

Upstream blocks occur predominantly in summer, whereas retrograding blocks are more common in winter. During winter, the eddy-driven jet stream sits at relatively low latitudes and solar radiation reaches Greenland for only a few hours per day; in summer, insolation is stronger and the eddy-driven jet stream is weaker and displaced further north, extending to Greenland's latitude. These two fundamental differences may influence blocking development over Greenland through at least two distinct mechanisms. (i) The Greenland ice dome, reaching elevations of up to 3200 meters [45], can interact with upper-level winds to generate a stationary Rossby wave response, thereby shifting the preferred regions of blocking onset [35, 47–49]; (ii) stronger solar radiation, higher atmospheric temperatures, and reduced sea ice cover over the Labrador Sea and the Baffin Bay may collectively increase water vapor content to the west of Greenland. As shown in Figure S3.7, the synoptic circulation associated with upstream blocks acts to tilt the eddy-driven jet stream northeastward, advecting moist air from the Labrador Sea and the Baffin Bay further north and up Greenland's orography. This configuration may trigger a stau-foehn effect, enhancing precipitation on the northwestern flank of the block (as depicted in Figure S7 in the Supplementary Material) and further amplifying low-level warming within the blocking center. The contribution of foehn winds to heat extremes over northeast Greenland has been established by Mattingly *et al.* [24], who demonstrated that the a high percentage of exceptional ice-melt events from the last decades were linked to anomalously high atmospheric river activity over western Greenland and associated foehn conditions in the northeast. This orographically forced circulation provides a plausible mechanism for both the enhanced moisture transport and the stronger 2-meter temperature anomalies evident for the upstream blocks in Figure S3.7. While these results strongly support a diabatic influence on blocking, a more granular analysis of local circulations would be required to confirm this causal link, a task left for future work.

If global warming were to alter the position of upper-level winds, increasing the likelihood of summer-like jet stream positioning with respect to Greenland orography, we might expect a corresponding change in the relative frequency of upstream versus retrograding blocks, especially in early summer. While the future response of the North Atlantic jet stream remains a subject of debate, many studies suggest a poleward shift in summer [50–53], a mechanism consistent with our hypothesis. Moreover, warmer sea surface temperatures and sea-ice free conditions in the Labrador sea and the Baffin Bay may enhance the advection of moist air over Greenland, further amplifying the blocks. The link between moisture and blocking connects our findings to broader research on extremes. For example, Barrett *et al.* [23] demonstrated the role of moisture transport over the Labrador Sea in amplify-

ing extreme blocking events, such as the ones that occurred in the years 2012 and 2019 [6]. Similarly, Scholz & Lora [54] found a strong correlation between major atmospheric river events and high-latitude heatwaves, particularly over northeast Canada. Our finding that upstream blocks are intrinsically linked to high-latitude moisture advection supports the hypothesis that the impact of such atmospheric rivers may increase in a warmer, moister atmosphere. Ultimately, confirming this causal chain would require targeted numerical experiments designed to separate thermodynamic and dynamical effects.

Lastly, we evaluated future trends in Greenland blocking using CMIP6 projections under the SSP3-7.0 warming scenario. While retrograding blocks are projected to decrease significantly–explaining the declining total blocking frequency reported by Delhasse *et al.* [46] and Hanna *et al.* [15]–upstream blocks show an increasing trend, particularly when assessed through the GHA index. Given that CMIP6 models underestimate both the historical magnitude and trend of GB frequency [18], our findings suggest that models point to, or at least do not rule out, a modest future increase in upstream blocking. This projected rise may be linked to jet stream position shifts, sea-ice reduction over the Labrador sea and the Baffin Bay, reduced spring snow cover in North America, and intensified moisture transport and atmospheric rivers over the North Atlantic. Our Lagrangian analysis offers a new lens for understanding these phenomena, indicating that future trends in Greenland blocking may hinge on the behavior of its upstream component.

3.6 APPENDIX

3.6.1 Seasonal cycle of Greenland blocking frequency and WBI

Figure A3.1 compares the annual cycle of blocking frequency—expressed as the number of blocked days per month—with the monthly distribution of WBI.

Both the DAV and GHA indices exhibit a peak of atmospheric blocking frequency during the summer months, with the DAV index capturing this peak slightly earlier than the GHA index. The number of blocked days per month is comparable between the two indices, suggesting that the detection thresholds are well calibrated.

For both indices, the WBI boxplots shift toward negative values during summer. When using the GHA index, the WBI distribution also becomes narrower in these months, indicating reduced variability. A similar, though less pronounced, narrowing is observed with the DAV index.

From a dynamical perspective, the shift of the WBI toward negative values in summer reflects an increase in anticyclonic wave breaking (i.e., upstream blocking trajectories), which accounts for nearly half of all events in July. In contrast, during winter, most blocking events are retrograding. As discussed in the Conclusions, this seasonal behavior of the WBI distribution, as well as the varying number of monthly blocked days, may be linked to the latitudinal migration of the polar jet stream, which shifts poleward in summer and equatorward in winter, interacting

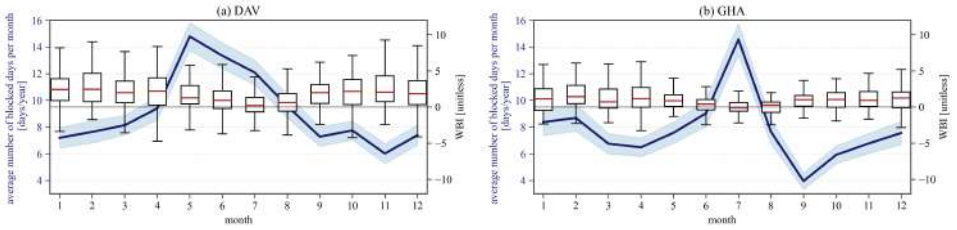

Figure A3.1: ERA5 annual cycle of WBI compared to blocking frequency expressed as number of blocked days per month. Panel a refers to the analysis conducted through the DAV index, while panel b refers to the GHA index. In each panel the blue line expresses the number of blocked days per month averaged over the 1940-2024 reanalysis dataset [days/year]. The blue shadings represent the inter-annual standard deviation of the number of blocked days. The boxplots showcase the WBI [unitless] distribution for each month.

differently with surface orography and surface thermal gradients.

3.6.2 CMIP6 models description

Table 3.1 reports the list of climate models that are part of the Coupled Model Intercomparison Project Phase 6 and that we employ in our analysis. We chose the model for which we could retrieve daily data for both the historical and future projections runs. For each model, we use the main physics configuration (p1), while incorporating some members with varying forcing configurations (f2,f3) to increase ensemble size. Detailed forcing specifications are not described in more detail here as model dependent. Comparing the number of historical and ssp370 runs it is evident how the number of runs analyzed varies considerably between models and investigated period. For most of the models we analyzed more historical runs than future projections runs in order to have a good estimate of Greenland blocking variability. Moreover, the model for which we have the largest number of runs is UKESM1-0-LL. Since the results have a greater dependence on the models that provide a larger amount of simulations, we evaluated the impact of excluding UKESM1-0-LL from our analysis. No appreciable differences were found, meaning that UKESM1-0-LL behave similarly to the average of the other models.

model	historical runs	ssp370 runs
ACCESS-CM2	3	1
CNRM-ESM2-1	3	3
CanESM5	8	2
IITM-ESM	1	1
INM-CM5-0	9	1
KACE-1-0-G	3	1
MIROC6	8	1
MPI-ESM1-2-LR	8	1
MRI-ESM2-0	9	1
NorESM2-LM	2	1
NorESM2-MM	2	1
UKESM1-0-LL	13	14

Table 3.1: Number of historical and ssp370 runs per model

3.7 Supplementary Material

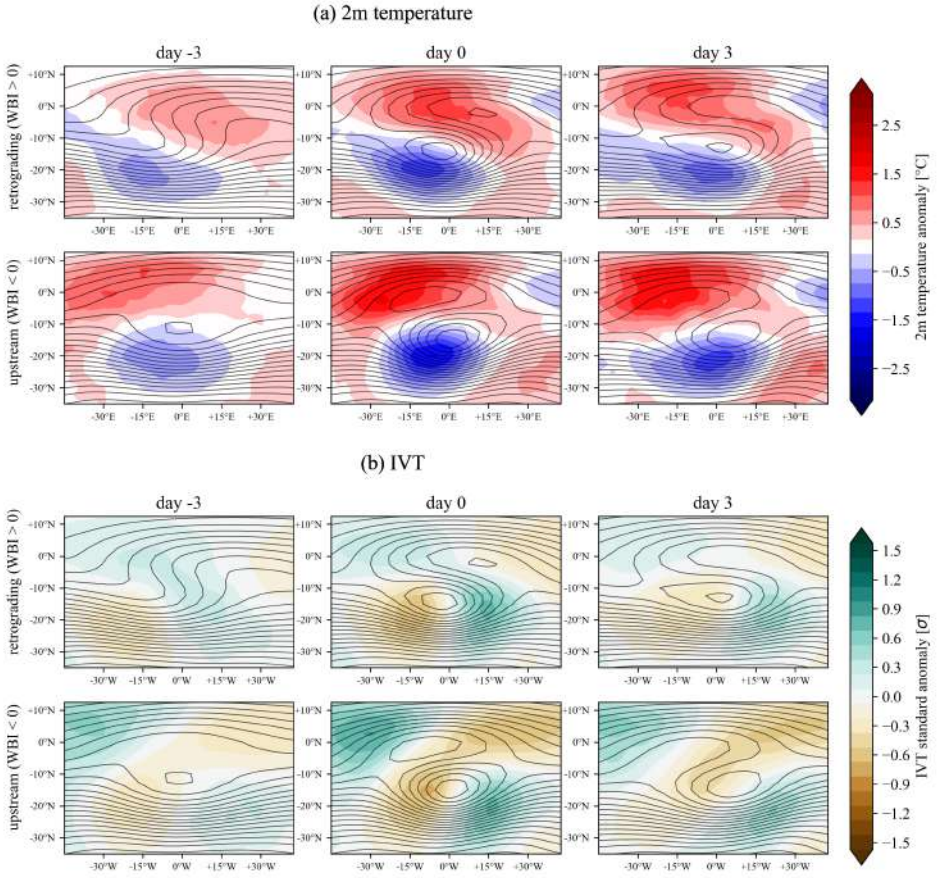

Figure S3.1: Composites of the time evolution of retrograding and upstream blocking events over Greenland from ERA5 reanalysis (JJA) detected through the DAV index. Composite plots are shown in the reference system of the block's center of mass. Black contours represent the 500 hPa geopotential height composite (Z500), plotted every 40 m. Shading refers to the composite anomaly of near-surface temperature (2 m temperature, K; panel A) and to the composite standardized anomaly of IVT (panel B). Anomalies are computed with respect to the seasonal mean. A Student's t-test was used to assess significance; all shaded regions are significant at the 95% confidence level.

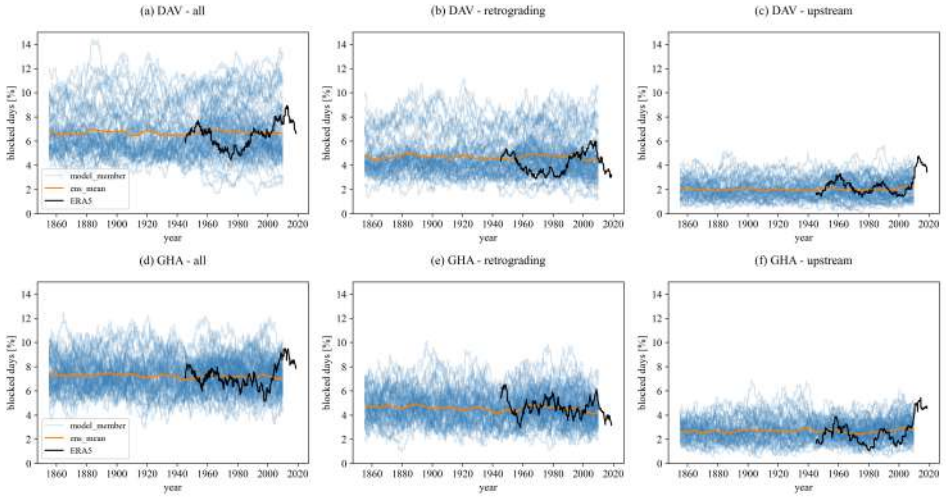

Figure S3.2: Summer (JJA) monthly blocking frequency time series. Black lines indicate ERA5 reanalysis, blue lines indicate individual CMIP6 ensemble members, and orange lines indicate the ensemble mean. The top row (a–c) shows blocking frequency detected using the DAV index, while the bottom row (d–f) shows frequency detected using the GHA index. The left column (a,d) refers to all blocking events crossing Greenland, the center column (b,e) to retrograding blocks, and the right column (c,f) to upstream blocks.

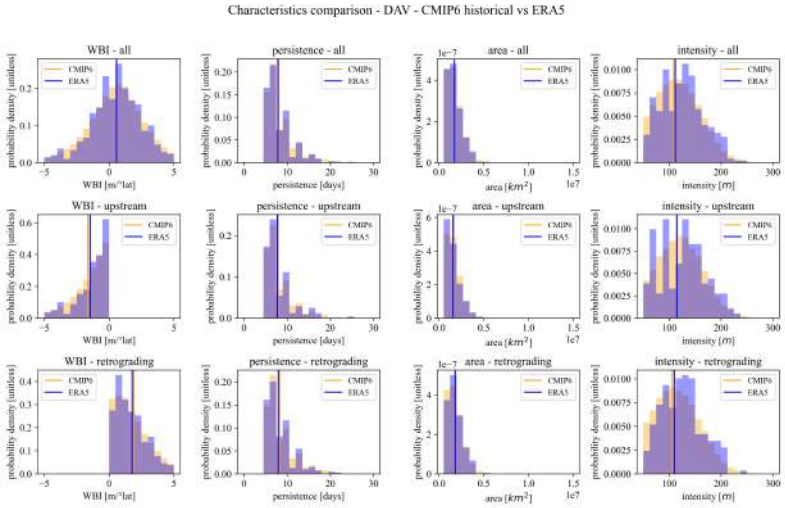

Figure S3.3: Comparison of blocking characteristics in ERA5 reanalysis and CMIP6 historical simulations detected using the DAV index. Rows correspond to different blocking types (top to bottom: all, upstream, and retrograding blocking events). Columns correspond to different characteristics (left to right: Wave Breaking Index, WBI, m/°lat; persistence, days; area, km^2; and intensity, m). Purple indicates ERA5 and gold indicates the CMIP6 historical ensemble. Vertical lines denote distribution means.

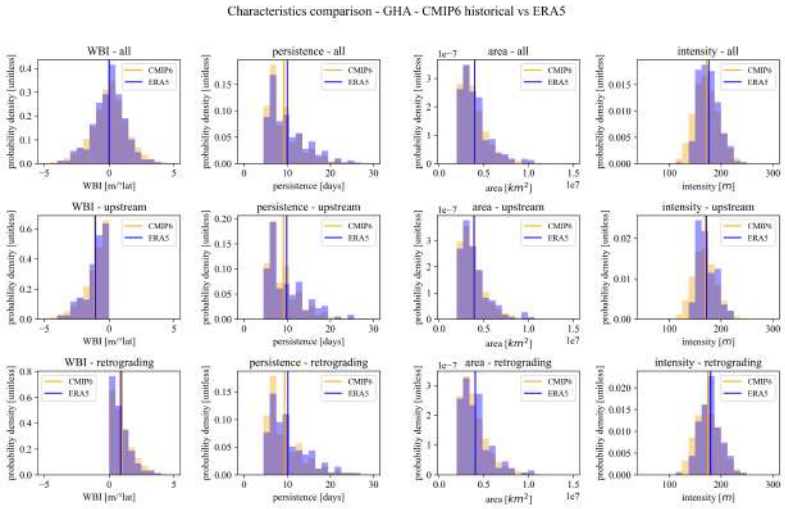

Figure S3.4: Same as Figure S3.3, but for blocking characteristics detected using the GHA index.

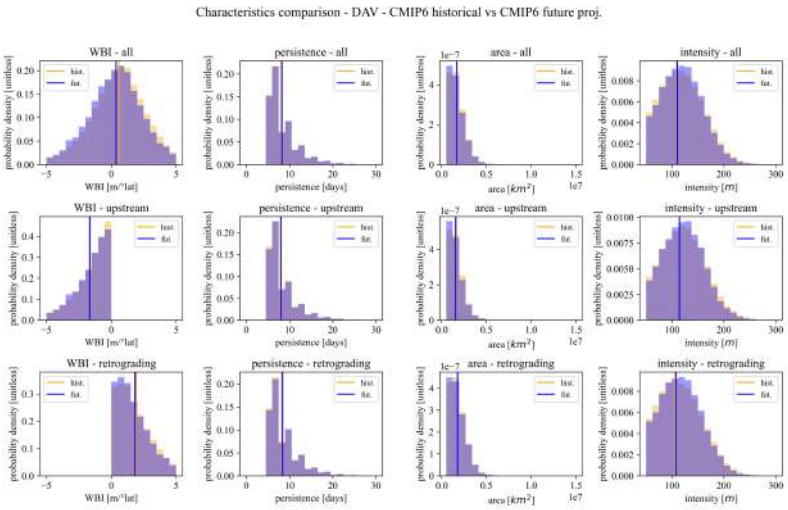

Figure S3.5: Comparison of blocking characteristics in CMIP6 historical simulations and CMIP6 future projections detected using the DAV index. Purple indicates the CMIP6 future ensemble and gold indicates the CMIP6 historical ensemble. Vertical lines denote distribution means.

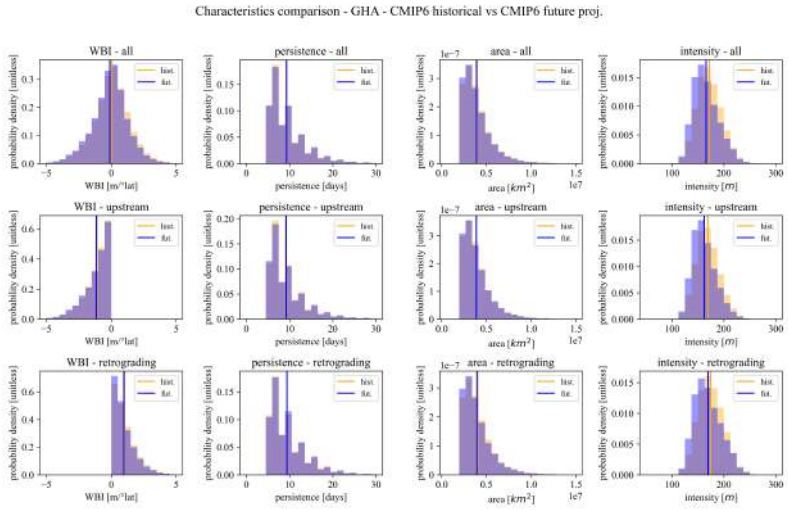

Figure S3.6: Same as Figure S3.5, but for blocking characteristics detected using the GHA index.

REFERENCES

1. Gregory, J. M. *et al.* Threatened loss of the Greenland ice-sheet. *Nature* **428,** 616–616 (2004).

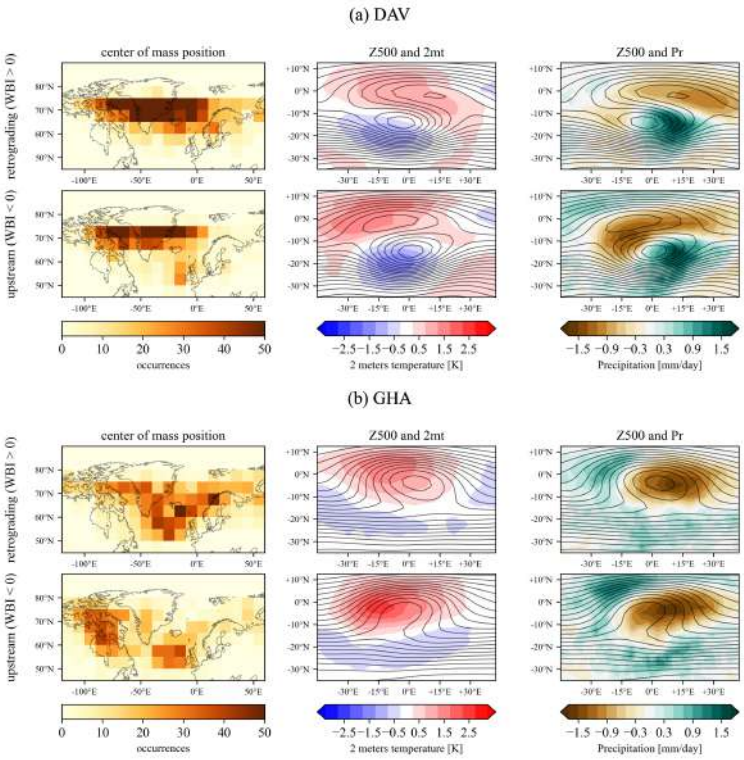

Figure S3.7: Composites and center of mass positions of retrograding and upstream blocking events over Greenland from ERA5 reanalysis (JJA). The center-of-mass position plots are 2D histograms with 10°lon × 5°lat bins, showing how often the center of mass of an upstream or retrograding block falls within each bin. Composite plots are plotted in the reference system of the block's center of mass (e.g. x axis represents relative longitude). Black contours represent the 500hPa geopotential height composite (Z500). Contours are plotted every $40m$***. Shadings refer to the composite anomaly of temperature above the surface (2 meters temperature - or 2mt [K]) and to the composite total precipitation. Anomalies have been computed with respect to the seasonal mean. A Student's t-test was performed to assess the significance of the plotted anomalies, with all shaded contours significant at the 95% confidence level. Panel a) showcases blocking events detected through the DAV index and panel b) showcases blocking events detected through the GHA index.***

2. Driesschaert, E. *et al.* Modeling the influence of Greenland ice sheet melting on the Atlantic meridional overturning circulation during the next millennia. *Geophysical Research Letters* **34.** doi:https://doi.org/10.1029/2007GL029516 (2007).

3. Buckley, M. W. & Marshall, J. Observations, inferences, and mechanisms of the Atlantic Meridional Overturning Circulation: A review. *Reviews of Geophysics* **54,** 5–63. doi:https://doi.org/10.1002/2015RG000493 (2016).

4. Bellomo, K. *et al.* Future climate change shaped by inter-model differences in Atlantic meridional overturning circulation response. *Nature Communications* **12,** 3659. doi:https://doi.org/10.1038/s41467-021-24015-w (2021).

5. Vacca, A. V. *et al.* On the role of AMOC weakening in shaping wintertime Euro-Atlantic atmospheric circulation. *Climate Dynamics* **63,** 1–16. doi:https://doi.org/10.1007/s00382-025-07747-z (2025).

6. Tedesco, M. & Fettweis, X. Unprecedented atmospheric conditions (1948–2019) drive the 2019 exceptional melting season over the Greenland ice sheet. *The Cryosphere* **14,** 1209–1223. doi:https://doi.org/10.5194/tc-14-1209-2020 (2020).

7. Hanna, E. *et al.* The influence of North Atlantic atmospheric and oceanic forcing effects on 1900–2010 Greenland summer climate and ice melt/runoff. *Int. J. Climatol* **33,** 862–880. doi:DOI:10.1002/joc.3475 (2013).

8. Charney, J. G. & DeVore, J. G. Multiple flow equilibria in the atmosphere and blocking. *Journal of the atmospheric sciences* **36,** 1205–1216 (1979).

9. Hoskins, B. J. *et al.* On the use and significance of isentropic potential vorticity maps. *Quarterly Journal of the Royal Meteorological Society* **111,** 877–946 (1985).

10. Vautard, R. Multiple weather regimes over the North Atlantic: Analysis of precursors and successors. *Monthly weather review* **118,** 2056–2081. doi:https://doi.org/10.1175/1520-0493(1990)118<2056:MWROTN>2.0.CO;2 (1990).

11. Benedict, J. J. *et al.* Synoptic view of the North Atlantic oscillation. *Journal of the Atmospheric Sciences* **61,** 121–144. doi:https://doi.org/10.1175/1520-0469(2004)061<0121:SVOTNA>2.0.CO;2 (2004).

12. Woollings, T. *et al.* A new Rossby wave–breaking interpretation of the North Atlantic Oscillation. *Journal of the Atmospheric Sciences* **65,** 609–626. doi:https://doi.org/10.1175/2007JAS2347.1 (2008).

13. Davini, P. *et al.* Coupling between Greenland blocking and the North Atlantic Oscillation pattern. *Geophysical Research Letters* **39.** doi:https://doi.org/10.1029/2012GL052315 (2012).

14. Tedesco, M. *et al.* Evidence and analysis of 2012 Greenland records from spaceborne observations, a regional climate model and reanalysis data. *The Cryosphere* **7,** 615–630. doi:https://doi.org/10.5194/tc-7-615-2013 (2013).

15. Hanna, E. *et al.* Greenland Blocking Index 1851–2015: a regional climate change signal. *International Journal of Climatology* **36,** 4847–4861. doi:https://doi.org/10.1002/joc.4673 (2016).

16. McLeod, J. T. & Mote, T. L. Linking interannual variability in extreme Greenland blocking episodes to the recent increase in summer melting across the Greenland ice sheet. *International Journal of Climatology* **36.** doi:DOI:10.1002/joc.4440 (2016).

17. Preece, J. R. *et al.* Summer atmospheric circulation over Greenland in response to Arctic amplification and diminished spring snow cover. *Nature Communications* **14,** 3759. doi:https://doi.org/10.1038/s41467-023-39466-6 (2023).

18. Maddison, J. *et al.* Missing increase in summer Greenland blocking in climate models. *Geophysical Research Letters* **51,** e2024GL108505. doi:10.1029/2024GL108505 (2024).

19. Teng, H. *et al.* Warming pattern over the Northern Hemisphere midlatitudes in boreal summer 1979–2020. *Journal of Climate* **35,** 3479–3494. doi:https://doi.org/10.1175/JCLI-D-21-0437.1 (2022).

20. Beckmann, J. *et al.* Summer Greenland Blocking in observations and in SEAS5. 1 seasonal forecasts: robust trend or natural variability? *EGUsphere* **2025,** 1–34. doi:https://doi.org/10.5194/egusphere-2024-3998 (2025).

21. McLeod, J. T. & Mote, T. L. Assessing the role of precursor cyclones on the formation of extreme Greenland blocking episodes and their impact on summer melting across the Greenland ice sheet. *Journal of Geophysical Research: Atmospheres* **120,** 12357–12377. doi:https://doi.org/10.1002/2015JD023945 (2015).

22. Liu, C. & Barnes, E. A. Extreme moisture transport into the Arctic linked to Rossby wave breaking. *Journal of Geophysical Research: Atmospheres* **120,** 3774–3788. doi:https://doi.org/10.1002/2014JD022796 (2015).

23. Barrett, B. S. *et al.* Extreme Greenland blocking and high-latitude moisture transport. *Atmospheric Science Letters* **21,** e1002. doi:10.1002/asl.1002 (2020).

24. Mattingly, K. S. *et al.* Increasing extreme melt in northeast Greenland linked to foehn winds and atmospheric rivers. *Nature Communications* **14,** 1743. doi:https://doi.org/10.1038/s41467-023-37434-8 (2023).

25. Luu, L. N. *et al.* Greenland Teubler2023drysummer blocking characteristics: an evaluation of a high-resolution multi-model ensemble. *Climate Dynamics* **62,** 10503–10523. doi:https://doi.org/10.1007/s00382-024-07453-2 (2024).

26. Hauser, S. *et al.* Life cycle dynamics of Greenland blocking from a potential vorticity perspective. *Weather and Climate Dynamics* **5,** 633–658. doi:10.5194/wcd-5-633-2024 (2024).

27. Wallace, J. M. & Gutzler, D. S. Teleconnections in the Geopotential Height Field during the Northern Hemisphere Winter. *Monthly Weather Review* **109,** 784–812. doi:10.1175/1520-0493(1981)109<0784:TITGHF>2.0.CO;2 (1981).

28. Pfahl, S. *et al.* Importance of latent heat release in ascending air streams for atmospheric blocking. *Nature Geoscience* **8,** 610–614. doi:https://doi.org/10.1038/ngeo2487 (2015).

29. Teubler, F. *et al.* Similarity and variability of blocked weather-regime dynamics in the Atlantic–European region. *Weather and Climate Dynamics* **4,** 265–285. doi:10.5194/wcd-4-265-2023 (2023).

30. Filippucci, M. *et al.* Impact of stochastic physics on the representation of atmospheric blocking in EC-Earth3. *Weather and Climate Dynamics* **5,** 1207–1222. doi:10.5194/wcd-5-1207-2024 (2024).

31. Hersbach, H. *et al.* The ERA5 global reanalysis. *Quarterly journal of the royal meteorological society* **146,** 1999–2049. doi:https://doi.org/10.1002/qj.3803 (2020).

32. Eyring, V. *et al.* Overview of the Coupled Model Intercomparison Project Phase 6 (CMIP6) experimental design and organization. *Geoscientific Model Development* **9,** 1937–1958. doi:https://doi.org/10.5194/gmd-9-1937-2016 (2016).

33. Filippucci, M. *Blocktrack* 2024. doi:10.5281/zenodo.13837897.

34. Davini, P. *et al.* Bidimensional diagnostics, variability, and trends of Northern Hemisphere blocking. *Journal of Climate* **25,** 6496–6509 (2012).

35. Woollings, T. *et al.* Blocking and its response to climate change. *Current climate change reports* **4,** 287–300. doi:https://doi.org/10.1007/s40641-018-0108-z (2018).

36. Dole, R. M. & Gordon, N. D. Persistent anomalies of the extratropical Northern Hemisphere wintertime circulation: Geographical distribution and regional persistence characteristics. *Monthly Weather Review* **111,** 1567–1586. doi:https://doi.org/10.1175/1520-0493(1983)111<1567:PAOTEN>2.0.CO;2 (1983).

37. Tyrlis, E. *et al.* Reconciling different methods of high-latitude blocking detection. *Quarterly Journal of the Royal Meteorological Society* **147,** 1070–1096. doi:10.1002/qj.3960 (2021).

38. Davini, P. & d'Andrea, F. From CMIP3 to CMIP6: Northern Hemisphere atmospheric blocking simulation in present and future climate. *Journal of Climate* **33,** 10021–10038. doi:https://doi.org/10.1175/JCLI-D-19-0862.1 (2020).

39. Sousa, P. M. *et al.* European temperature responses to blocking and ridge regional patterns. *Climate Dynamics* **50,** 457–477. doi:https://doi.org/10.1007/s00382-017-3620-2 (2018).

40. Dolores-Tesillos, E. *et al.* On the role of moist and dry processes in atmospheric blocking biases in the Euro-Atlantic region in CMIP6. *Weather and Climate Dynamics* **6,** 471–487. doi:https://doi.org/10.5194/wcd-6-471-2025 (2025).

41. Woollings, T. *et al. Variability of the North Atlantic eddy-driven jet stream, QJ Roy. Meteor. Soc., 136, 856–868* 2010. doi:https://doi.org/10.1002/qj.625.

42. Ji, L. & Tibaldi, S. Numerical simulations of a case of blocking: The effects of orography and land–sea contrast. *Monthly weather review* **111,** 2068–2086. doi:https://doi.org/10.1175/1520-0493(1983)111<2068:NSOACO>2.0.CO;2 (1983).

43. Berckmans, J. *et al.* Atmospheric blocking in a high resolution climate model: influences of mean state, orography and eddy forcing. *Atmospheric Science Letters* **14,** 34–40. doi:https://doi.org/10.1002/asl2.412 (2013).

44. Davini, P. *et al.* Orographic resolution driving the improvements associated with horizontal resolution increase in the Northern Hemisphere winter mid-latitudes. *Weather and Climate Dynamics Discussions* **2021,** 1–25. doi:https://doi.org/10.5194/wcd-3-535-2022 (2021).

45. Hawley, R. L. *et al.* Greenland Ice Sheet elevation change: Direct observation of process and attribution at summit. *Geophysical Research Letters* **47,** e2020GL088864. doi:https://doi.org/10.1029/2020GL088864 (2020).

46. Delhasse, A. *et al.* Brief communication: CMIP6 does not suggest any atmospheric blocking increase in summer over Greenland by 2100. *International Journal of Climatology* **41,** 2589–2596. doi:https://doi.org/10.1002/joc.6977 (2021).

47. Held, I. M. & Ting, M. Orographic versus thermal forcing of stationary waves: The importance of the mean low-level wind. *Journal of Atmospheric Sciences* **47,** 495–500. doi:https://doi.org/10.1175/1520-0469(1990)047<0495:OVTFOS>2.0.CO;2 (1990).

48. Held, I. M. *et al.* Northern winter stationary waves: Theory and modeling. *Journal of climate* **15,** 2125–2144. doi:https://doi.org/10.1175/1520-0442(2002)015<2125:NWSWTA>2.0.CO;2 (2002).

49. Nakamura, N. & Huang, C. S. Atmospheric blocking as a traffic jam in the jet stream. *Science* **361,** 42–47. doi:10.1126/science.aat0721 (2018).

50. Simpson, I. R. *et al.* A diagnosis of the seasonally and longitudinally varying midlatitude circulation response to global warming. *Journal of the Atmospheric Sciences* **71,** 2489–2515. doi:https://doi.org/10.1175/JAS-D-13-0325.1 (2014).

51. Shaw, T. *et al.* Storm track processes and the opposing influences of climate change. *Nature Geoscience* **9,** 656–664. doi:https://doi.org/10.1038/ngeo2783 (2016).

52. Chen, G. *et al.* Sensitivity of the latitude of the westerly jet stream to climate forcing. *Geophysical Research Letters* **47,** e2019GL086563. doi:https://doi.org/10.1029/2019GL086563 (2020).

53. Zhou, W. *et al.* Seasonally and regionally dependent shifts of the atmospheric westerly jets under global warming. *Journal of Climate* **35,** 5433–5447. doi:https://doi.org/10.1175/JCLI-D-21-0723.1 (2022).

54. Scholz, S. R. & Lora, J. M. Atmospheric rivers cause warm winters and extreme heat events. *Nature* **636,** 640–646. doi:https://doi.org/10.1038/s41586-024-08238-7 (2024).

Chapter 4

Mean circulation zonal asymmetries control the response of atmospheric blocking to Arctic warming in an aquaplanet experiment

This research article will be soon submitted to a peer-reviewed journal. The work has been conducted with the help and supervision of Neil Lewis (University of Exeter), Stephen Thomson (University of Exeter) and Simona Bordoni (University of Trento).

4 MEAN CIRCULATION ZONAL ASYMMETRIES CONTROL THE RESPONSE OF ATMOSPHERIC BLOCKING TO ARCTIC WARMING IN AN AQUAPLANET EXPERIMENT

ABSTRACT

This study investigates how Arctic amplification (AA) influences midlatitude temperature extremes through the lens of the Traffic Jam theory. We perform idealized aquaplanet simulations in two configurations: a zonally symmetric setup and a zonally asymmetric experiment featuring a localized midlatitude storm track. For each of this configuration, an additional simulation is performed where AA is imposed through anomalous surface heating in the polar region, allowing us to study the response of atmospheric blocking under Arctic warming and isolate the role of zonal asymmetries.

In the symmetric configuration, atmospheric blocking—identified as persistent Local Wave Activity (LWA) events—is zonally uniform, whereas the asymmetric configuration exhibits a blocking maximum downstream of the localized storm track. Under AA, the zonally averaged blocking frequency increases in both configurations. However, the regional response differs: in the asymmetric case, the maximum in blocking frequency shifts upstream.

We interpret these changes by diagnosing the carrying capacity of the midlatitude flow. In both configurations, the zonally averaged increase in blocking is primarily driven by a weakening of the zonal winds, which reduces the Doppler-shifted Rossby wave group velocity and, in turn, decreases the flow carrying capacity. While the reduction in carrying capacity has similar characteristics in the two configurations, in the asymmetric case it leads to an upstream shift of blocking frequency as a direct consequence of the threshold behavior of blocking onset that lies at the core of the Traffic Jam theory. This mechanism, which has received limited attention so far, highlights the importance of mean circulation characteristics in shaping the blocking response to external forcing such as Arctic warming. Our results may therefore help to understand blocking responses to AA in more comprehensive models by linking differences in modeled responses to biases in the mean circulation state.

4.1 INTRODUCTION

The Arctic is warming at an accelerated pace compared to the rest of the globe. This phenomenon, known as Arctic Amplification (AA), is a robust feature of anthropogenic climate change that has emerged from present-day observations and that climate models project to further increase by the end of the century [1]. Both local and remote feedbacks contribute to the accelerated warming of the polar region, which mainly affects the lower levels of the atmosphere. These include surface albedo and temperature feedbacks—related to lapse-rate and radiative processes—as well as changes in the meridional transport of energy [2–4].

A warmer Arctic leads to a reduced meridional temperature gradient near the surface, potentially modifying the characteristics of the midlatitude atmospheric circulation, with important impacts on densely populated regions. This mechanism, together with an apparent increase in cold-spell frequency in the midlatitudes during the early 21st century, motivated numerous studies on the response of midlatitude atmospheric variability to Arctic warming, leading to contrasting results over the past decades. In particular, Francis & Vavrus [5] proposed a mechanism by which a weaker meridional temperature gradient leads to a slower and wavier jet, more prone to atmospheric blocking onset. However, similar analyses by Barnes [6] and Screen & Simmonds [7] found no significant increase in midlatitude waviness during the early 21st century.

Subsequent studies highlighted several sources of uncertainty that hinder a robust assessment of the midlatitude circulation response to AA. These include the limited length of the available observational record [8, 9], the use of different metrics to assess changes in waviness [7, 10], and the wide spread of AA magnitudes simulated by climate models [11]. More recent observational studies have shown that the previously reported increase in cold-spell occurrence disappears when the last 15 years of reanalysis data are included, indicating that the earlier trends were strongly influenced by internal atmospheric variability [9, 12].

To investigate circulation changes expected by the end of the century, several modeling studies have been conducted following the Polar Amplification Model Intercomparison Project (PAMIP) protocol [13]. These studies identified a weak but statistically significant response to AA, consisting of a weakening and an equatorward shift of the midlatitude jet stream [14, 15]. Using the same PAMIP experiments, an increase in Scandinavian blocking frequency was reported [16, 17], together with a small increase in blocking over northeast Asia [18] and contrasting changes over the North Pacific [19].

The hierarchy of climate models has proven to be a useful tool to study circulation changes following AA. Idealized models have been used to investigate the competition between upper-tropospheric tropical heating and AA [20], the response of the stratospheric circulation to AA [21, 22], the effect of ice-constraining methods on the atmospheric circulation response [23, 24], the role of lapse-rate feedbacks [25, 26], changes to the polar radiative-advective equilibrium [4] , barotropic eddy–mean flow feedbacks [23], and the role of Rossby wave breaking location

[27]. Earlier literature also showed that atmospheric blocking can occur in aquaplanet simulations despite the absence of zonal asymmetries [28]. In this context, Hassanzadeh *et al.* [29] studied the response of atmospheric blocking to AA using a blocking index based on geopotential height, finding a decrease in blocking frequency. However, Hassanzadeh *et al.* [29] results may be affected by the experimental setup, which produces an unrealistic Arctic warming pattern extending far into the midlatitudes and influencing the circulation response through changes in static stability [26].

The use of diverse methods and metrics to quantify circulation changes across the extensive literature on AA impacts on midlatitude circulation has resulted in apparently contrasting assessed responses. Early studies focused on jet-stream waviness [5–7], while later work examined cold-spell trends [e.g. 30, 31], Rossby wave phase speed [32], transient kinetic energy [23], and several waviness metrics [29, 33–35]. These different metrics capture distinct aspects of eddy variability and can therefore lead to diverging responses. For example, Geen *et al.* [10] showed that different waviness metrics applied to idealized AA experiments can lead to opposite trends. Moreover, the relationship between the climatology of these waviness metrics and persistent temperature extremes, or atmospheric blocking, is non-trivial [36, 37]. As a result, a physically consistent description of how AA, jet-stream waviness, mean circulation changes, and storm-track position and intensity combine to affect atmospheric blocking occurrence is still lacking.

Moreover, most idealized modeling studies assume zonally symmetric background conditions [e.g. 20, 22, 23, 25, 26, 29], despite previous studies that have shown that circulation responses to AA depend on longitude, differing, for example, between the Atlantic and Pacific basins [e.g. 13, 18, 19, 27, 38]. In this context, localized midlatitude storm tracks have been shown to be an important factor in determining regions of blocking onset [36, 37] and should therefore be included when assessing links between changes in waviness and changes in blocking frequency relevant for Earth's atmospheric circulation.

In this study, we aim to clarify how changes in the mean circulation affect jet-stream waviness and blocking occurrence in a physically consistent framework, in which differences in transient kinetic energy, waviness, and Rossby wave group velocity play different but complementary roles in shaping the atmospheric blocking response to AA. This is done by using idealized simulations with two configurations: a zonally symmetric aquaplanet, and a zonally asymmetric one where we investigate the effect of a localized storm track on the blocking response. The idealized experiments are conducted using the ISCA intermediate-complexity modeling framework, described in more detail in Section 4.2.1. To provide a physically consistent interpretation of changes in waviness and temperature extremes, we adopt the Traffic Jam theory framework introduced by Nakamura & Huang [36] to explain atmospheric blocking onset. In this framework, blocking occurs when local wave activity (LWA)—a measure of midlatitude jet waviness [34]—exceeds a critical threshold referred to as the jet's carrying capacity. This threshold can be computed from the quasi-geostrophic potential vorticity field, stationary wave ampli-

tude, LWA, and the midlatitude wind field, thereby quantitatively linking changes in the mean atmospheric circulation to changes in blocking frequency [37, 39].

The paper is structured as follows. Section 4.2 presents the methods, including the experimental setup, a description of local wave activity and Traffic Jam theory, and the diagnostics used for blocking detection, carrying capacity, and transient kinetic energy. Section 4.3 presents the results, starting with the unperturbed atmospheric circulation of the symmetric and asymmetric setup, followed by the zonal-mean and local zonal responses, and concluding with an interpretation of the circulation changes in terms of carrying capacity. Section 4.4 provides a summary and the conclusions of the study.

4.2 METHODS

4.2.1 Experimental setup

We perform four simulations using the Isca intermediate-complexity model [40]. Isca is a flexible framework for idealized simulations of planetary atmospheres at varying levels of complexity and realism, built upon the modeling infrastructure of the Flexible Modeling System (FMS) developed at the Geophysical Fluid Dynamics Laboratory (GFDL).

Our model configuration closely follows Kaspi & Schneider [41], itself based on Frierson *et al.* [42]. The experimental setup is an aquaplanet with no land–sea contrast or orography and the insolation is constant, with neither a diurnal or seasonal cycle. The surface is represented by a 1.5m mixed-layer ocean, with a prescribed analytical observation-based meridional heat flux adapted from Merlis *et al.* [43]. Radiation is represented with a two-stream gray scheme that distinguishes only between shortwave and longwave components, while moist convection is parameterized using a simplified Betts-Miller scheme [44] configured as in O'Gorman & Schneider [45]. Further details can be found in Kaspi & Schneider [41].

We conduct four experiments: two represent our control, baseline experiments (BASE runs) and two include a simple AA-like forcing (hereafter AA). Each pair consists of a zonally symmetric aquaplanet (symmetric run, SYM) and a simulation where a triangular heating is prescribed in the ocean mixed layer (asymmetric run, ASYM), mimicking a western boundary current and breaking the zonal symmetry of the storm track. More details are provided below. The four simulations analyzed are therefore BASE SYM, AA SYM, BASE ASYM, and AA ASYM. Each experiment is integrated for 50 years at T85 resolution, with daily output saved at $1.5^\circ \times 1.5^\circ$ horizontal resolution and 30 vertical sigma levels. Because our configuration is hemispherically symmetric, we analyze both hemispheres by mirroring Southern Hemisphere data onto positive latitudes and appending the resulting fields, obtaining a 100-year time series defined for the Northern Hemisphere only.

The forcing in the ASYM experiments is designed to mimic the effect of a western boundary current, such as that at the entrance of the Atlantic and Pacific

storm tracks [41], by imposing a localized heating. This forcing enhances localized eddy generation and produces a midlatitudes storm track comparable to those observed in reanalysis. The heat flux is prescribed uniformly over a triangular region with vertices $(25°\mathrm{N}, 75°\mathrm{W})$, $(25°\mathrm{N}, 100°\mathrm{W})$, and $(50°\mathrm{N}, 75°\mathrm{W})$, with a magnitude of $850\ \mathrm{W\,m^{-2}}$. Unlike Kaspi & Schneider [41], who apply the triangular heating only in the Northern Hemisphere, we impose it symmetrically in both hemispheres. To prevent the introduction of a net global energy source, we compute the heat added along each latitude circle and subtract an equal amount distributed uniformly across all longitudes. For instance, at $25°\mathrm{N}$ we integrate the heating between $100°\mathrm{W}$ and $75°\mathrm{W}$ and subtract the same total amount along the full latitude circle from $180°\mathrm{W}$ to $180°\mathrm{E}$.

To emulate the effects of AA, we further prescribe a uniform surface heat flux of $30\ \mathrm{W\,m^{-2}}$ poleward of $72°\mathrm{N}$ and $72°\mathrm{S}$. Similarly to the asymmetric forcing, we integrate the imposed heat flux over the polar area and we remove the same amount of heat uniformly from the global surface, to avoid global warming. The chosen heat flux produces a polar warming slightly stronger than end-of-century projections under high-emission scenarios, which helps amplify the circulation response and facilitates the study of blocking changes. Sensitivity tests with alternative forcing magnitudes produced qualitatively similar results (not shown). The latitudinal boundary of this heating is chosen by matching the climatological Northern Hemisphere winter sea-ice extent (retrieved from NASA datasets): from the observed sea-ice area, we derive the latitude of a zonally symmetric circle with equal area. Although the surface energy balance produced by this method is not physically realistic [4], the resulting warming pattern closely resembles that of more comprehensive models, giving us confidence that its influence on the mean circulation is sufficiently realistic for the purposes of this study.

4.2.2 Local wave activity definition

A key quantity analyzed in this study is the local wave activity (A or LWA), defined as in Huang & Nakamura [34]. Intuitively, A measures the amplitude of the Rossby wave as the meridional displacement of Quasi-Geostrophic Potential Vorticity (QGPV) from a zonally symmetric wave-free state.

To compute this, we first define a zonally symmetric reference state $q_{ref}(\phi, z, t)$, where ϕ is the latitude, z is the pseudo-height coordinate and t is the temporal coordinate. The goal is to find a unique PV value, q_{ref}, for every latitude ϕ_i such that the meridional integral of PV poleward of the q_{ref} contour is exactly equal to the meridional integral of the actual PV field poleward of the latitude ϕ_i. Taking an array of equally spaced latitudes ϕ_i, for each element of the array we evaluate the integral $C(\phi_i, z, t)$

$$C(\phi_i, z, t) \equiv \int_{-180}^{+180} \int_{\phi_i}^{90} q(\lambda, \hat{\phi}, z, t) d\hat{\phi} d\lambda, \tag{4.1}$$

where λ is the longitudinal coordinate, $\hat{\phi}$ is the latitudinal coordinate used for the

integration and $q(\lambda, \hat{\phi}, z, t)$ is the QGPV field. We then determine the reference PV values associated to ϕ_i, $q_{ref,i}$ (or $q_{ref}(\phi_i, z, t)$) by evaluating the integral $I(q_{ref,i})$,

$$I(q_{ref,i}) \equiv \int_{-180}^{+180} \int_{\Phi(q_{ref,i})}^{90} q(\lambda, \hat{\phi}, z, t) d\hat{\phi} d\lambda, \tag{4.2}$$

where $\Phi(q_{ref,i})$ is the latitude of the contour of $q_{ref,i}$ at a longitude λ—and imposing the equivalence

$$C(\phi_i, z, t) = I(q_{ref,i}). \tag{4.3}$$

Note that if at a given longitude, more than one contour is found, the area in the enclosed contour is removed from the integral defined in Eq. 4.2. A graphical representation of variables and of the integrals $C(\phi_i, z, t)$ and $I(q_{ref,i})$ is shown in Fig. 4.1. Repeating this process for each element of the array ϕ_i yields a one-to-one map $q_{ref}(\phi, z, t)$. Finally, once q_{ref} is known, it is possible to invert the QGPV equation to define a reference state $(u_{ref}, v_{ref}, \theta_{ref})$.

The procedure may be better understood by describing the algorithm used to compute it on a gridded dataset. First, for each element of the latitude array, ϕ_i, the integral in Eq. 4.1, $C(\phi_i, z, t)$, is evaluated. To find the corresponding q_{ref}, a GQPV threshold is initialized starting from the minimum GQPV value found at the analyzed time t, and the integral is computed over all grid cells with GQPV values less than or equal to the current threshold. This procedure is repeated while progressively increasing the threshold until the evaluated integral equals or exceeds $C(\phi_i, z, t)$. The final threshold value is denoted $q_{\rm ref}$, and the corresponding integral is $I(q_{\rm ref}, z, t)$.

In spherical coordinates, A is therefore expressed as:

$$\mathcal{A}(\lambda, \phi, z, t) \cos\phi = -a \int_{\phi}^{\phi(q_{ref})} \left[q(\lambda, \hat{\phi}, z, t) - q_{\rm ref}(\phi, z, t) \right] \cos(\hat{\phi})\, d\hat{\phi}, \tag{4.4}$$

where a is the radius of Earth. The Schematic 4.1 depicts the integral domain, represented by a blue solid line. We drop the subscript i in Eq. 4.4 as the map $q_{ref}(\phi, z, t)$ is approximated to be continuous. The higher the number of elements of the array ϕ_i used to compute $I(q_{\rm ref})$, the smaller the approximation. Here, we chose a number of array elements twice as large as the resolution of the input dataset. For further details and a comprehensive description of the equivalent latitude and LWA computation see Huang & Nakamura [34] and Nakamura & Zhu [46].

In the present paper, LWA, the associated LWA fluxes, the reference-state q_{ref} and $(u_{ref}, v_{ref}, \theta_{ref})$ are computed through the *falwa* package (`https://github.com/csyhuang/hn2016_falwa`), a Github repository recently published as an open-source tool for LWA computation. For details about the numerical integrations needed for the analysis we redirect the reader to the falwa paper, Huang *et al.* [47]. The rest of the analysis is carried under the assumption of a

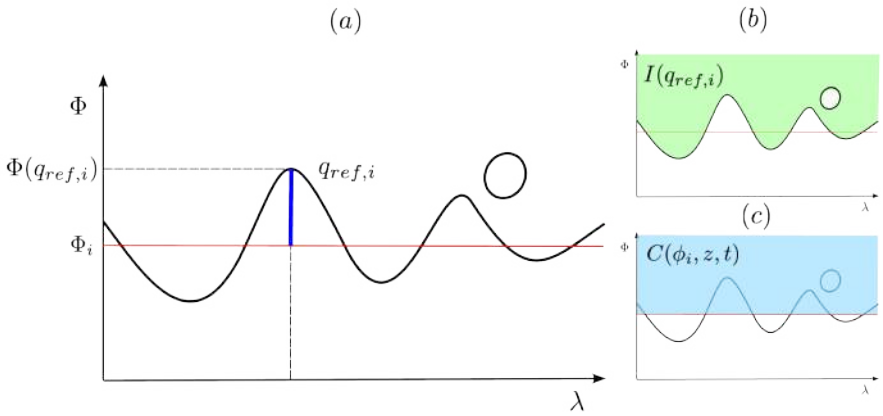

Figure 4.1: Schematic diagram showing (on a longitude-latitude plane) the variables and integration domains used in the LWA calculation. In panel a, the horizontal red line represent the i-th investigated latitude, ϕ_i. The solid black contour represents the contour associated to the reference QGPV, $q_{ref,i}$. The solid blue meridional segment represents the domain over which the QGPV anomaly is integrated in Eq. 4.4. In panel b, the green area represents the integral $I(q_{ref,i})$, delimited by the wavy reference contour. In panel c, the blue area represents the integral $C(\phi_i, z, t)$, defined as the area poleward of the fixed latitude ϕ_i. By construction, the areas in (b) and (c) are equal.

shallow atmosphere and hereafter we refer to LWA as the density weighted vertical average of the 3D quantity (dropping the vertical coordinate dependence). Moreover, while the cosine factor explicitly written in eq. 4.4 is important for correctly scaling LWA with latitude, we drop it to improve the readability of the following computations. Hereafter, when referring to LWA, we intend the mass-weighted vertically averaged local wave activity multiplied by the cosine of latitude.

4.2.3 Traffic Jam Theory

First introduced by Nakamura & Huang [36], the Traffic Jam theory interprets blocking as a local wave activity increase resulting from nonlinear interactions between waves and the mean flow. The mathematical framework adopted by the authors to interpret blocking onset and maintenance is analogous to the model of Richards [48] for a traffic jam on a highway. In this analogy, LWA represents the density of cars, the LWA zonal flux represents the cars density flux, and stationary waves crests act as traffic bottlenecks, such maintenance works or speed limit decreases. Blocking emerges when an accumulation of LWA (car density) leads to a decrease in local wave activity flux (cars slow down because of the proximity to other vehicles), triggering a nonlinear mechanism that blocks the flow. Just like a highway traffic jam, blocking occurs more likely in proximity to stationary waves crests, which in the Northern Hemisphere winter are typically located at the exit of the Pacific and Northern Atlantic storm tracks.

This analogy becomes quantitative because of the relationship between local wave activity and zonal winds, which follows from the non-acceleration theorem [49], valid within the WKB condition of a slowly varying medium [34]. The relationship is expressed as:

$$u_e = -\alpha A, \qquad \alpha > 0, \tag{4.5}$$

where u_e is the eddy component of the mass-weighted vertical average of the zonal component of the wind, A is the local wave activity and α is a positive correlation parameter typically smaller than 1. Note that u_e in Eq. 4.5 is the local departure of the zonal wind from the reference-state ($u - u_{ref}$), and it is different from the usual Eulerian definition of an eddy quantity, which is computed as the departure from the climatological temporal mean ($u - \overline{u}_{ref}$), and will be hereafter denoted u'.

Eq. 4.5 describes an anti-correlation between local wave activity and zonal winds, attributing to Rossby waves the same characteristic as vehicles: where traffic increases, drivers decelerate. The physical meaning of α can be better understood through a geometrical argument: where LWA increases, the flow acquires a meridional component, at the expense of the zonal component, hence locally and temporarily decreasing the zonal winds. In a baroclinic atmosphere, the torque associated with eddies is not entirely used in deflecting the jet stream, but is partially dissipated in diabatic processes, causing a reduction in α. On the contrary, a more barotropic atmosphere is generally associated with a higher α, reaching the limit

$\alpha = 1$ for an idealized barotropic flow. The climatology reported by Barpanda & Nakamura [37] in reanalysis supports this arguments, showing higher values of α in the tropical latitudes and lower values of α in the storm track region.

The second fundamental assumption required to create this analogy concerns the generalized Eliassen-Palm flux relation. Consider its general formulation:

$$\frac{\partial A}{\partial t} = -\nabla \cdot \mathbf{F} + \dot{A} \tag{4.6}$$

where F is the 3D Eliassen-Palm flux and $\dot{A}$ is the non-conservative sources and sinks of A. Assuming that the zonal convergence of LWA dominates the tendency of LWA at synoptic time scales over the meridional or vertical LWA components, one can rewrite Eq. 4.6 as:

$$\frac{\partial A}{\partial t} = -\frac{\partial F_\lambda}{\partial x} + S - \frac{A}{\tau}, \tag{4.7}$$

with zonal flux F_λ. The remaining, smaller terms are grouped into S, which represents sources and sinks of local wave activity, and A/τ, which accounts for linear damping due to dissipation. This approximation is well supported in the midlatitudes and in storm-track regions, as shown by Barpanda & Nakamura [37]. The zonal flux F_λ is further decomposed into three contributions:

$$F_\lambda = F_1 + F_2 + F_3, \tag{4.8}$$

Here, F_1 represents the zonal advective flux of LWA due to the reference-state winds. F_2 denotes the zonal nonlinear advective flux of LWA, which is associated with the parameter α introduced in Eq. 4.5, and represents the effeect of waves slowing down the background flow. F_3 represents the zonal transport of local wave activity associated with wave dispersion. These fluxes can be written explicitly following Nakamura & Huang [36] or approximated through semi-empirical relations that make the analogy with the Traffic Jam model possible. Both the explicit forms and the approximations are reported in Table 4.1.

By making use of the flux approximation, Eq. 4.7 can thus be rewritten as

$$\frac{\partial A}{\partial t} = -\frac{\partial}{\partial x}\left[\left(u_0 + c_{xg} - \alpha A\right) A\right] + S - \frac{A}{\tau}, \tag{4.9}$$

where $u_0 + c_{xg}$ is hereafter referred to as the Doppler-shifted Rossby-wave group velocity and represents the linear contribution to LWA advection, while $-\alpha A$ represents the nonlinear contribution.

The LWA, A, in Eq. 4.9 is subsequently decomposed into a slowly varying component A_0, associated with the stationary Rossby-wave amplitude (discussed in detail in Section 4.2.4) and a transient eddy component A'. Substituing $A(x,t) = A_0(x,t) + A'(x,t)$ into the budget, we obtain a new expression for the transient local wave activity tendency:

$$\frac{\partial A'}{\partial t} = -\frac{\partial}{\partial x}\underbrace{\left[\left(C(x) - \alpha A'\right)A'\right]}_{\text{(i)}} + S - \frac{A'}{\tau}, \tag{4.10}$$

Flux	Exact expression	Approx relation with A	Description
F_λ	$F_1 + F_2 + F_3$	$(u_0 - \alpha A + c_{xg})A$	Total zonal flux
F_1	$u_{\text{ref}} A$	$u_0 A$	Zonal advective flux of LWA due to reference state wind
F_2	$-\frac{a}{\cos\hat{\phi}} \int_{\hat{\phi}}^{\hat{\phi}(q_{ref})} u_e q_e \cos(\hat{\phi})\, d\hat{\phi}$	$-\alpha A^2$	Zonal nonlinear advective flux of LWA
F_3	$\frac{1}{2}\left(v_e^2 - u_e^2 - \frac{\theta_s^2 \text{Re}^{-z/H}}{H S_\theta}\right)$	$c_{xg} A$	Zonal advective flux of LWA associated with wave dispersion.

Table 4.1: Wave activity fluxes and their approximate relations with A. In these relations, θ is potential temperature, v is the meridional component of the wind, $H \equiv 7km$ is the assumed scale height, R is the ideal gas constant, S_θ is the hemispheric-mean static stability given by $\partial_z \tilde{\theta}$—where the superscript $\tilde{}$ refers to the hemispheric mean—c_{xg} is the zonal component of the group velocity of Rossby waves, the variable u_0 is time and vertically averaged u_{ref}. Moreover, as for Eq. 4.5 in the main text, the subscript $(\,\cdot\,)_e$ refers to the anomaly with respect to the reference state. All quantities are density weighted and vertically averaged.

where $C(x)$ is defined as:

$$C(x) \equiv u_0 + c_{xg} - 2\alpha A_0(x). \tag{4.11}$$

Term (i) is an expression for the eddy zonal advective flux $F'(A')$ and it is a downward-opening parabola with an absolute maximum, as shown in Fig. 4.2. $F'(A')$ attains a maximum when $\partial F'/\partial A' = 0$, i.e. at the threshold amplitude

$$A_c(x) = \frac{C(x)}{2\alpha}, \tag{4.12}$$

and the corresponding maximum flux, or carrying capacity $F_c(x)$ defined as

$$F_c(x) = \frac{C(x)^2}{4\alpha}. \tag{4.13}$$

The carrying capacity $F_c(x)$ provides a useful framework to understand blocking formation. The behavior of the system results from the competition between linear wave propagation and nonlinear wave-mean flow interaction, leading to two distinct dynamical regimes. For $A'(x,t) < A_c$, the linear term $C(x)A'$ dominates the flux $F'(A')$. As the wave amplitude increases, so does the flux. In this state, Rossby waves behave like cars on an open highway: adding more vehicles simply increases the total traffic volume. This corresponds to the normal eastward progression of synoptic storms.

Once the wave amplitude $A'(x,t)$ grows past the threshold amplitude $A_c(x)$, the nonlinear term $-\alpha A'^2$ becomes dominant. As A' grows, the waves exert a powerful torque that locally decelerates the eddy zonal velocity u_e. In this regime, even as the wave amplitude keeps increasing ($\frac{\partial A'}{\partial t}$ >0), the flux decreases, leading to an upstream accumulation of local wave activity and ultimately to blocking onset. This behavior is formally analogous to a traffic jam: beyond a critical density, any further increase in the number of vehicles leads to a reduction in the total

flow rate due to localized deceleration. The carrying capacity therefore represents the boundary between two different regimes: a "free-flow" regime in which higher LWA is associated with a larger flux and a "congested" regime in which higher LWA opposes the flux and leads to a local accumulation of LWA. These two different regimes are more clearly depicted in Schematic 4.2.

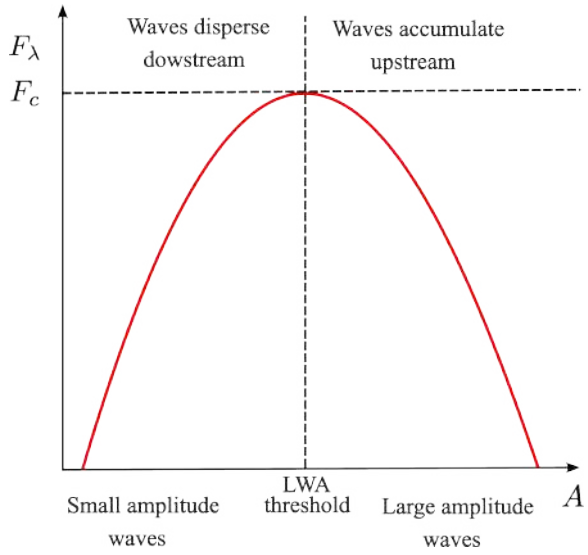

Figure 4.2: Schematic of the relationship between LWA and the zonal LWA flux. For small-amplitude waves $(LWA << threshold)$***, the zonal flux increases with LWA due to linear, Doppler-shifted eastward propagation, whereas for large-amplitude waves*** $(LWA >> threshold)$ ***the flux decreases as nonlinear, eddy-induced zonal flow becomes dominant.***

Lastly, we underscore how regions where $C(x)$ is smaller are more prone to blocking formation. These are areas where the stationary Rossby wave amplitude A_0 is larger and/or the Doppler-shifted Rossby waves velocity $u_0 + c_{xg}$ is smaller. In this sense, the Traffic Jam theory provides a robust framework to quantitatively estimate the contribution of changes in the background flow to observed or projected changes in atmospheric blocking frequency.

4.2.4 Estimation of the carrying capacity

In the following analysis, we compare the carrying capacity F_c with the climatological frequency of atmospheric blocking and its response to different forcings. This approach allows us to quantify the individual contribution of changes in the background zonal winds, stationary wave amplitude and the parameter α to changes in blocking frequency. In order to estimate the value of F_c in our experiments we follow the methodology of Barpanda & Nakamura [37]. We provide a brief overview here and refer interested readers to their work for a comprehensive derivation.

In brief, in order to compute F_c we need to estimate three quantities: the parameter α, the Doppler-shifted Rossby waves group velocity $u_0 + c_{xg}$, and the stationary local wave activity A_0. The α parameter is derived from Eq. 4.5 as the linear regression coefficient between the eddy zonal wind and the local wave activity. This can be expressed as:

$$\alpha = -\frac{u_e A^T}{AA^T}, \tag{4.14}$$

where the subscript ^{T} identifies the transpose of the matrix and the other variables have already been defined. The Doppler shifted Rossby wave group velocity is computed through the explicit forms of the zonal LWA fluxes (reported in Table 4.1), which are computed by the falwa package. In particular, by combining the zonal advective flux of LWA (F_1) and the Rossby wave flux (F_3), we can determine $u_0 + c_{xg}$ as:

$$F_1 + F_3 = (u_0 + c_{gx})Acos\phi. \tag{4.15}$$

As for the parameter α, the velocity is computed from the slope of the linear regression. For both estimates, the regression is performed point-wise, with the temporal dimension as the free coordinate.

The stationary component A_0 is computed as the local wave activity associated with the time averaged QGPV field. This can be expressed mathematically as:

$$\mathcal{A}_0(\lambda, \phi, z, t)\cos\phi = -a\overline{\int_{\phi}^{\phi+\phi_C} \left(\overline{q}(\lambda, \hat{\phi}, z, t) - q_{\mathrm{REF}}(\phi, z, t)\right)\cos(\phi + \hat{\phi})\, d\hat{\phi}}\,, \tag{4.16}$$

where the overbar denotes a temporal average computed over the full available period.

Prior to these computations (Eqs. 4.14, 4.15, 4.16) we apply a Fourier low-pass filter to the LWA field, filtering out variability associated with time scales shorter than 4 days. Moreover, we apply a zonal smoothing a using a 15° moving window. In this way we select only weather systems with blocking timescales and synoptic spatial scales as in Barpanda & Nakamura [37].

4.2.5 Blocking detection and tracking

We detect atmospheric blocking using a recent release of the *blocktrack* algorithm, an open source tool designed to detect atmospheric blocking from gridded datasets (`https://github.com/michele-filippucci/blocktrack`), that includes a new blocking index based on LWA. This new LWA-based index works similarly to widely adopted 500-hPa geopotential height anomaly-based indices, such as the one introduced by Dole & Gordon [50], but it is based on LWA. Specifically, for each day, we compute LWA anomalies A' in the 40–80° latitudinal band. We then compute the standard deviation of these anomalies ($\sigma_{A'}$) identifying a single value for the whole time series and spatial domain. This approach is appropriate

because our simulations do not feature a seasonal cycle or a time-varying external forcing. Finally, grid points where LWA anomalies A' satisfy the criterion:

$$A' > 1.26\sigma_{A'} \tag{4.17}$$

are identified as blocked. The threshold value corresponds to the 90th percentile of a Gaussian distribution and is calculated separately for each experiment.

The LWA anomalies are then tracked in time using the blocktrack Lagrangian tracking. A detailed description of the tracking algorithm is provided in Filippucci *et al.* [51]. We then filter the events selecting only those with area larger than $3 \cdot 10^6$ km^2 and duration longer than 4 days. The persistence filter was chosen following established literature on the topic, as reviewed by Woollings *et al.* [52], while the area threshold was determined through sensitivity tests to match the climatological frequency of blocking identified by alternative indices (not shown).

The composites shown in Section 4.3.1 are computed in the reference system of the blocking event's center of mass to characterize the average properties of blocking events in the baseline simulation. More specifically, we analyze each blocking event separately, computing its center-of-mass trajectory and selecting an area of 70° longitude × 40° latitude centered over a grid point 10° latitude south of its daily center of mass. The southward offset is introduced to better highlight the equatorward features of the blocking system that would otherwise be excluded from the composite. We repeat this procedure for all blocking events and we average the mass-weighted vertically averaged QGPV (hereafter just QGPV, unless otherwise stated) and the 850-hPa temperature anomaly over the inspected areas.

4.2.6 Transient kinetic energy

We use the 250-hPa transient kinetic energy (TKE) to quantify the impact of the imposed asymmetric ocean heat flux relative to the zonally symmetric control. TKE is computed by applying a Fast Fourier Transform (FFT) to the zonal and meridional wind fields at 250 hPa and then applying a 2–6 days band-pass filter to isolate the high-frequency variability associated with transient eddies. Finally we transform back the fields to the physical space. After applying the filter, TKE is computed as:

$$TKE = \frac{u_{bp}^2 + v_{bp}^2}{2} \tag{4.18}$$

where u_{bp} and v_{bp} are the band-passed zonal and meridional winds, respectively. Compared to LWA, TKE typically measures the energy associated with short-lived eddies, such as those forming the storm track, whereas LWA does not distinguish between temporal scales of variability. Moreover, while TKE is computed at an upper-tropospheric level (250 hPa), LWA is a mass-weighted vertically averaged quantity.

4.2.7 Statistical significance

Statistical significance is assessed using a Student's t-test. The variance of the variables presented in the Results section is calculated through a bootstrap technique. The significance of the anomalies (both between ASYM and SYM simulations, and between AA and BASE simulations) is computed as:

$$T_s = \frac{< x_1 > - < x_2 >}{\sqrt{\sigma_1^2 + \sigma_2^2}} \tag{4.19}$$

where T_s is the Student's t-value, x_1 and x_2 are the temporal means of the analyzed fields and σ_1^2 and σ_2^2 are their variances. The T_s value is then compared with a reference value for the 95% confidence interval. Since our experimental setup is computationally efficient, the number of simulated years was chosen to ensure that all anomalies shown below are significant at this confidence level.

4.3 RESULTS

4.3.1 Baseline experiments: atmospheric circulation and blocking climatology

We begin by analyzing TKE and LWA for the baseline experiments to assess the ability of our experimental setup to represent the atmospheric circulation features we are interested in. We begin with the representation of the storm track features and in Fig. 4.3a, we compare TKE climatology in the BASE SYM and BASE ASYM simulations. The BASE SYM simulation exhibits a zonally symmetric TKE distribution with a maximum extending from 20°N to 60°N. In contrast, in the BASE ASYM simulation, the imposed heat flux locally enhances transient eddies and their associated energy, producing a localized storm track.

A comparison of the symmetric and asymmetric (Fig. 4.3a) setups reveals a spatially heterogeneous TKE response: TKE increases downstream of the prescribed heating but decreases elsewhere. Nevertheless, the zonal mean shows an overall increase in TKE in the ASYM run. The localized enhancement is likely driven by increased baroclinicity, whereas the reduction elsewhere possibly results from the cooling applied along the same latitude band as the heating (see Section 4.2.1). However, a similar TKE decrease was reported by Kaspi & Schneider [41] even in the absence of such cooling, and was instead attributed to a stationary wave response to the localized heating. Overall, the TKE distribution of our experiments is in line with expectations, with the asymmetric setup showing good similarities to Earth's circulation over the Northern Hemisphere oceanic basins [53] despite the idealized lower-boundary condition.

Given that our idealized setups produce reasonable TKE climatologies, we now shift our focus to LWA (Fig. 4.3b). We find that differences between the symmetric and asymmetric simulations are more intricate than those for TKE, even if a general increase in zonally averaged LWA is observed. In the BASE SYM simulation, LWA

maximizes within a latitudinal band between 40°N and 60°N. In the BASE ASYM simulation, however, LWA exhibits multiple maxima downstream of the prescribed heating. The largest maximum, located at the south-east corner of the heat flux region (60°E, 25°N), likely arises from the sharp temperature gradient generated by the surface heat flux, which strongly influences low-level waviness. A similar interpretation applies to the maximum just downstream of the northern vertex of the triangular forcing (20°W, 50°N). The maximum at (50°E, 30°N) lies within the storm-track region identified in Fig. 4.3a and may reflect enhanced transient eddy activity in that area. Finally, the maximum near (120°E, 50°N) appears at the exit of the localized storm track and corresponds to the crest of a stationary wave induced by the zonal asymmetry. The correspondence was verified by plotting the zonal anomaly of the 500-hPa geopotential height with respect to the long-term mean (not shown), which shows a wave-number 1 stationary wave pattern, with its crest over (120°E, 50°N). This feature is analogous to the stationary wave crests observed over Northern Europe or the western coast of North America in reanalysis data. In this case, however, the stationary wave arises solely from the imposed localized heating, rather than from land–sea contrasts or Earth's topography [54]. This final LWA maximum is the most relevant for the purpose of this study, as it corresponds to the region of blocking onset, as discussed below.

Having investigated the LWA and TKE climatology, we evaluate the representation of blocking in the two baseline simulations (Fig. 4.4a,b), discussing its relationship with the previously described features of the atmospheric circulation. In addition, the blocking climatology is compared with the carrying capacity to evaluate the applicability of the Traffic Jam theory to our experimental setup.

We start by analyzing Figure 4.4a, showing the zonal mean blocking frequency and carrying capacity for the BASE SYM simulation. The climatological maximum of blocking frequency occurs at 55°N, reaching approximately 2.5 blocked days per 100 days. As a reference, blocking frequency over Northern Europe in reanalysis data is typically assessed at 10 to 15% of days, depending on the detection method used [52], while in other regions, such as the Central Pacific, the blocking frequency is close to zero. Other analyses based on idealized aquaplanet simulations show blocking frequency similar to those found here [55, 56]. Moving our focus to the carrying capacity in Fig. 4.4a, we find that it attains its maximum around 40°N. A comparison between Fig. 4.4a and Fig. 4.3b reveals that the spatial distribution of blocking frequency closely resembles that of LWA, although it is shifted northward by about 5–10°N. This displacement is consistent with the higher carrying capacity values observed near 40°N, which makes blocking onset less likely on the southern flank of the LWA distribution.

Figure 4.4b illustrates the two-dimensional distribution of blocking frequency and carrying capacity for the BASE ASYM simulation. In this case, the blocking frequency maximum is located near (120°E, 55°N), reaching about 5 % of blocked days over the simulated period. Notably, the latitude of this maximum remains the same as in the BASE SYM simulation. Furthermore, the blocking frequency increases downstream and along the northern flank of the carrying capacity

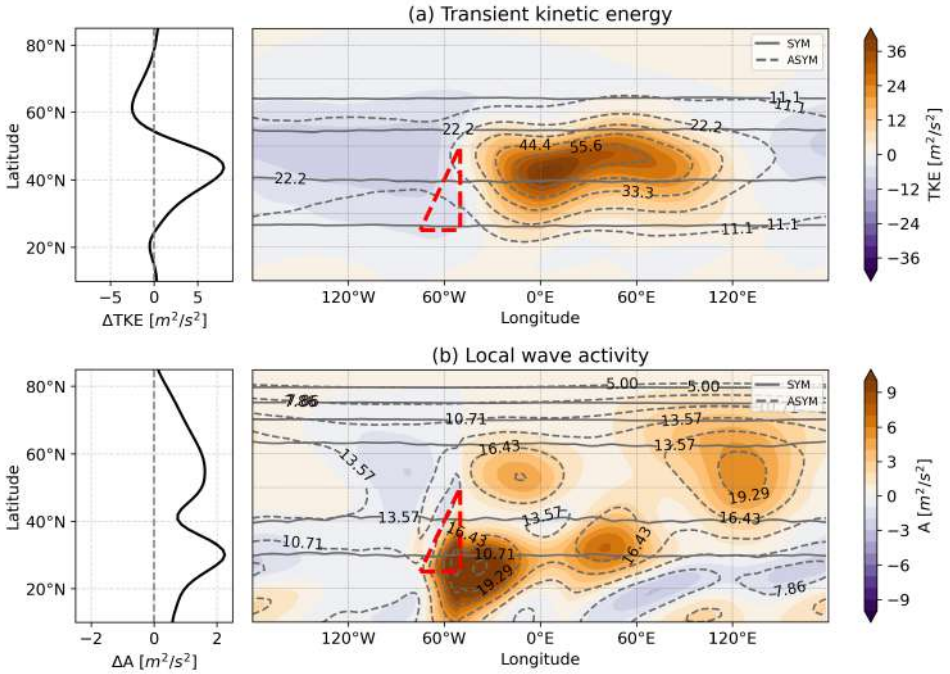

Figure 4.3: Climatology of TKE at 250hPa (panel a) and local wave activity (panel b). In each panel dashed contours represent the BASE ASYM simulation, while solid contours represent the BASE SYM simulation. The shadings depict the differences between the two (BASE ASYM - BASE SYM). The red triangle identifies the region where the triangular ocean heat flux has been applied in the ASYM simulations. On the left of each panel, the zonally averaged differences between the two (BASE ASYM - BASE SYM) are reported.

distribution, reflecting the threshold mechanism underlying blocking onset in the Traffic Jam theory framework. The climatological blocking frequency maximum also coincides with the LWA maximum at (120°E, 50°N) identified in Fig. 4.3b, supporting our hypothesis that this region corresponds to the crest of a stationary wave induced by asymmetric heating–an area whose characteristics resemble the exit of the Northern Atlantic storm track in ERA5 reanalysis, where blocking preferentially occurs [52]. Moreover, blocking frequency is rather low between longitudes 180°W and 70°W, despite the reduced carrying capacity. This reduction likely results from the low climatological LWA in the region (see Fig. 4.3b), owing to the scarcity of LWA sources. Finally, both the carrying capacity and atmospheric blocking frequency drop below 30°N. This feature is due to the fact that climatological zonal winds are significantly weaker over that region, reducing the carrying capacity, and LWA sources are induced by tropical baroclinic dynamics, rather than the barotropic dynamics responsible for blocking onset. Overall, the distribution of atmospheric blocking frequency is in line with what described by Barpanda & Nakamura [37] for ERA5 reanalysis: blocking onset occurs preferentially at the exit of the localized storm track, where carrying capacity values drop.

Fig. 4.4c,d shows composite plots of blocking events occurring in the BASE SYM and BASE ASYM simulations. To examine the characteristics of these events, we compute the 850-hPa temperature and QGPV, averaged over the lifecycle of each blocking event. As described in the Methods section (see Section 4.2.5), the composites are presented in the reference frame of the blocking events' center of mass. In both the BASE SYM and BASE ASYM cases, the tracking algorithm identifies a prominent ridge causing temperature anomalies as high as 9°K. Temperature anomalies are considerably larger in the BASE SYM simulation. Such large differences can be due to two different factors: (i) since the carrying capacity in Fig. 4.4b in the blocking frequency maximum region of the ASYM case is significantly lower than the zonally averaged SYM case, the LWA needed for blocking onset is smaller, which also translates in a less intense ridge. (ii) In the BASE ASYM simulation, atmospheric blocking occurs over a stationary wave crest, where the average 850-hPa temperature is higher. For the same LWA value, the temperature anomaly observed is therefore lower.

Moreover, temperature anomalies are considerably larger in our idealized simulations than for ERA5 blocking events [57, e.g.]. Such differences must be interpreted in light of the surface heat capacity, which in our idealized simulations is uniform and equal to a 1.5-m deep water column. Such an idealized surface may have a thermal inertia considerably lower than that of the regions of Earth where atmospheric blocking normally occurs (e.g. Scandinavia, where the blocking center region is partially covered by the Nordic and Baltic seas), allowing temperature anomalies associated with the events to be significantly higher.

By inspecting the climatological LWA, TKE, carrying capacity and atmospheric blocking frequency we gain confidence that our model is able to reproduce the mechanism of blocking onset coherently with the Traffic Jam theory. In the next sections we will therefore assess the response of atmospheric blocking to AA, in-

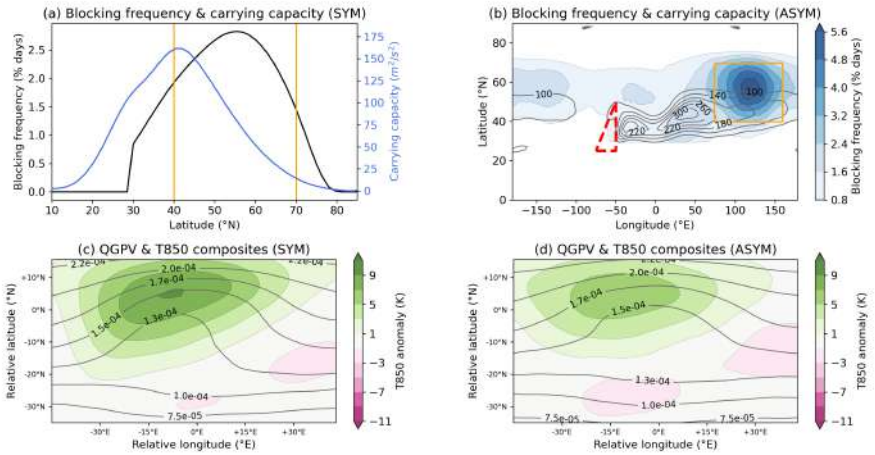

***Figure 4.4:** Panel (a) and (b) compare the atmospheric blocking frequency of the BASE ASYM and BASE SYM simulations with the corresponding carrying capacity. In panel (a) the zonal average of these two quantities for the BASE SYM experiment is plotted. The blue line refers to the zonally averaged carrying capacity and the black line to the zonally averaged blocking frequency. In panel (b) the black contour represents the carrying capacity, while the shadings represent the blocking frequency. The red triangle identifies the region where the triangular ocean heat flux has been applied in the ASYM simulations. In both panel (a) and (b) the ocher boundaries delimit the area for which the composites of panel (c) and (d) respectively were computed. Panel (c) showcases the PV composite (black contours) and the 850 hPa temperature anomaly composite (colored shadings) for the BASE SYM simulation. Panel (d) showcases the same quantities for the BASE ASYM simulation.*

terpreting the changes in light of this theoretical framework (Section 4.2.3).

4.3.2 Forced local and zonally symmetric response

We begin by analyzing the zonally average zonal wind and temperature anomalies in the meridional plane to examine the response of the atmospheric circulation to AA (Fig. 4.5). The wind and temperature response show similar features across the symmetric and asymmetric experiments. As shown in Fig. 4.5a-b, for both the SYM and ASYM simulations, the temperature response exhibits a pronounced low-level warming beginning around 60°N and increasing toward the pole, reaching values of 5.5–6K over the Arctic. As anticipated in Sec. 4.2.1, this warming is slightly higher than the AA projected by many current climate models under business-as-usual scenarios [11] at the end of the 21st century, as well as the Arctic warming projected by PAMIP experiments [14]. The warming extends vertically up to about 700 hPa, decreases aloft, and then intensifies again near the top of the troposphere, producing a double-maxima structure. Such a heating profile suggests changes in the meridional heat transport mediated by the atmosphere. In fact, the polar atmosphere is usually characterized by static conditions and hardly redistributes the heat vertically [4]. Finally, the Arctic warming is slightly stronger in the SYM simulations.

Moving to panels c-d, we show the response of the zonally averaged zonal winds to AA. We find that in both the symmetric and asymmetric setups zonal winds are displaced equatorward, with the weakening on the poleward side generally larger than the strengthening on the equatorial side; in the ASYM simulations, both effects are further amplified. The jet displacement is consistent with what observed in PAMIP [14, 38], even though the poleward weakening is more pronounced, likely because of the stronger Arctic heating and because of the stronger annular mode arising from the absence of topography [58]. Earlier studies attributed changes in zonal-wind intensity to eddy-mediated feedbacks. In fact, a less baroclinic atmosphere generates fewer midlatitude eddies, which account for a substantial fraction of the meridional transport of zonal momentum in the global circulation [59]. This reduction in eddy activity leads to an equatorward displacement of the jet.

We now examine the response to AA of the more complex diagnostics presented in Section 4.3.1, needed to assess changes in jet stream waviness and heat extremes in the midlatitudes. Figure 4.6 presents the behavior of TKE, LWA, and blocking frequency in both the SYM and ASYM experiments.

In the SYM simulations, TKE (first column; panel a) decreases by roughly 15–20% along the northern edge of its climatological distribution, likely reflecting reduced baroclinicity. The LWA response (panel c) exhibits a meridional displacement, showing an opposite behavior to the zonal wind field, consistent with the negative correlation between LWA and eddy zonal winds arising from the non-acceleration theorem (see Section 4.2.3). A secondary explanation for this shift is the jet stream acting as a waveguide that advects synoptic eddies [60–63]; accord-

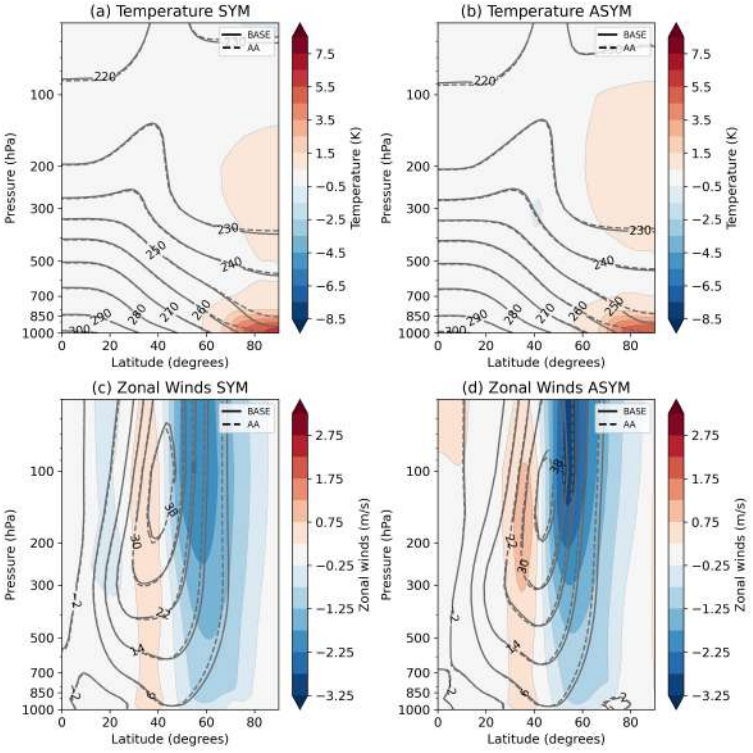

***Figure 4.5:** Panel a and b report the zonally averaged temperature response to AA, in the SYM and ASYM simulations respectively. Panel c and d depict the zonally averaged zonal winds response to AA, in the SYM and ASYM simulations respectively. In all plots, black solid (dashed) contours show the represented field as simulated by the BASE (AA) simulation. Moreover, shadings represent the difference between the AA runs and the BASE runs.*

ing to this interpretation, a displacement of the jet stream is inevitably followed by a displacement of the eddies distribution, which in turn influences the climatological LWA. Lastly, moving our attention to blocking frequency, panel e shows a spatially uniform but modest increase under AA, with maxima of about 0.3 % - 0.5 % of blocked days (about 10% - 15% of the original frequency).

Examining the right-hand column of Figure 4.6, which shows the ASYM simulations, we note that the zonally averaged response of LWA and TKE to AA closely resembles that of the SYM case, indicating that asymmetric surface heating does not substantially alter the zonal mean signal. The TKE response (panel b) again shows a weakening, which is more pronounced downstream of the imposed triangular heat flux anomaly. The LWA pattern (panel d) remains broadly similar to the SYM response, featuring decreases at low latitudes and increases at higher latitudes. In contrast, the blocking response (panel f) diverges markedly from the SYM behavior: instead of a uniform increase, AA induces a shift in the location of the blocking maximum. This produces regions with substantial blocking enhancement (up to 1.2 % of blocked days, representing a relative increase of up to 20%) and others with slight decreases. After zonal averaging, the net effect is a small increase in blocking frequency and a slight decrease at high latitudes.

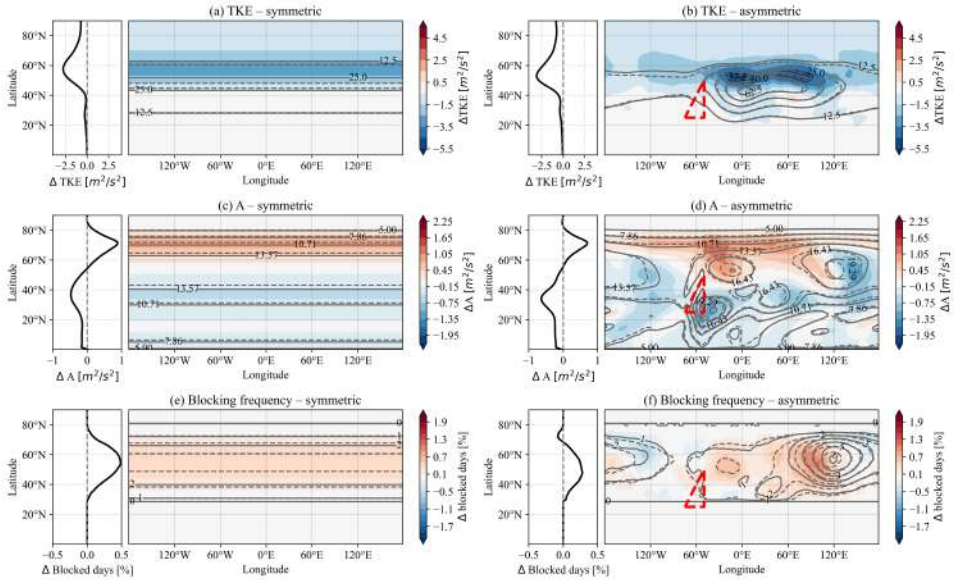

Figure 4.6: Panel a and b depict the response of TKE to AA, in the SYM and ASYM setups respectively. Panel c and d report the response of LWA, while panel c and f report the response of atmospheric blocking frequency. The shadings and the contours refer to the same experiments as in Fig. 4.5. On the left of each panel, the zonally averaged differences between the two (BASE ASYM - BASE SYM) are reported.

To summarize, while changes in LWA and TKE show comparable features in

the SYM and ASYM simulations, the response of atmospheric blocking to AA exhibits important differences; while the SYM case exhibits a uniform increase, the ASYM response is better described as an upstream displacement of the blocking maximum and a modest increase in the zonal average.

4.3.3 Interpretation of atmospheric blocking frequency changes

To understand the mechanism behind the changes in blocking frequency described above, we analyze the physical quantities within the context of the Traffic Jam theory discussed in Section 4.2.3. We start by analyzing the response to AA of the parameter α, the Doppler-shifted Rossby wave zonal group velocity, and the quasi-stationary component of LWA (i.e., stationary waves). We then analyze the carrying capacity, decomposing its response to AA into contributions arising from these variables.

Fig. 4.7 shows the sensitivity of the key dynamical parameters across both experimental setups. In both the SYM and ASYM simulations, AA induces a consistent reduction in the α parameter (panels a,b), with a slightly more pronounced zonally averaged decrease in SYM. According to the theoretical framework discussed in Section 4.2.3, variations in α are expected to arise from baroclinicity changes [37, 64], whereby a more baroclinic atmosphere features smaller α values, while more barotropic conditions lead to an increase. However, our results deviate from these expectations: despite the clear signals of reduced baroclinicity, manifested as diminished transient kinetic energy and a weakened meridional temperature gradient, the parameter α decreases.

To identify the responsible mechanisms, we use the definition of α given in Section 4.2.4 (Eq. 4.14) to decompose its change into contributions from changes in LWA variance and changes in covariance between LWA and zonal winds. In the Supplementary Material, we demonstrate that changes in the meridional wind shear may act to narrow the jet stream, concentrating the local wave activity variability in a narrower region and facilitating Rossby wave breaking on its northern and southern flanks, similarly to what reported by Ronalds & Barnes [27]. These circulation shifts modify both the variance and covariance terms, ultimately resulting in a significant reduction of α. Changes in the meridional wind shear are therefore expected to be of primary importance to assess the response of α to AA, while baroclinicity changes exert only a secondary effect. While a more detailed analysis of this mechanism is left for future work, a more comprehensive discussion and a series of supporting plots are provided in the Supplementary Material.

Moving to Fig. 4.7c and d, we observe a weakening of the Doppler-shifted zonal Rossby wave group velocity following AA. Such behavior is expected, as the group velocity is tightly connected to the zonal wind anomalies seen in Fig. 4.5. This weakening is followed by a modest strengthening at lower latitudes. In the asymmetric case, the zonal group velocity increases markedly within the storm track region, downstream of the triangular surface heat flux. After zonal averaging, differences are almost identical in the SYM and ASYM setup, consistent with the

zonal wind response shown in Fig. 4.5.

To conclude, panels e and f show the stationary LWA response. In the SYM case, we do not display stationary wave anomalies, as these simulations do not feature zonal asymmetries. In the ASYM case, stationary LWA maxima move upstream following AA. This shift again follows the modification of the zonal winds: according to the linear Rossby wave dispersion relation, the wavenumber of stationary Rossby waves increases for stronger zonal winds. Conversely, slower winds imply shorter stationary Rossby wave wavelength. This translates into an upstream displacement of the stationary Rossby wave crest with respect to the imposed heating, as clearly evident in panel f.

Having characterized the individual responses of the underlying physical parameters, we now evaluate how their collective changes shape the carrying capacity and, consequently, atmospheric blocking frequency. To this aim, we decompose the total change of the carrying capacity in response to AA into contributions from α, the Doppler-shifted Rossby wave zonal group velocity and the stationary LWA. This decomposition is expressed as:

$$\Delta F_c = \Delta F_{c,\alpha} + \Delta F_{c,u_0+c_{gx}} + \Delta F_{c,A_0} + residual\ . \tag{4.20}$$

where each term on the right-hand side quantifies the specific contribution of a different physical quantity. For instance, the response of the carrying capacity $\Delta F_{c,\alpha}$ due to changes in α is computed as:

$$\Delta F_{c,\alpha} = F_c(\alpha_f, (u_0 + c_{gx})_b, A_{0,b}) - F_c(\alpha_b, (u_0 + c_{gx})_b, A_{0,b})\ , \tag{4.21}$$

where the subscripts *b* and *f* denote 'baseline' and 'forced', respectively. The residual in Eq. 4.20 is estimated by computing the total response of F_c directly from the simulation output and then subtracting the other terms of the decomposition. For all simulations shown here, the residual is negligible and, hence, not shown in the following analyses. The results of this decomposition are shown in Fig. 4.8, with the bottom row showing the total response. Focusing on the SYM simulation (panels a–c–e–g), we find that the decrease in α (panel a) leads to an increase in carrying capacity centered around 50°N. However, this effect is counterbalanced by a decrease in Doppler-shifted Rossby wave group velocity, which in turn leads to a decrease of LWA at high latitudes (panel c). Conversely, the increase at lower latitudes (panel b) induces a modest carrying capacity increase. As expected stationary waves (panel e) do not arise in SYM, and therefore do not contribute to the response.

The combined effect of these competing factors (panels a-c-e) is a dipole-like response: a decrease (increase) north (south) of 45°N (panel g). An inspection of the magnitudes reveals that the group velocity term dominates the response, overriding the influence of α. Nevertheless, the decrease in α remains an important component, as it acts as a negative feedback that buffers the overall reduction of the carrying capacity under AA. Importantly, these shifts are spatially consistent with the blocking increase observed north of 45°N (see Fig. 4.6): a smaller carrying

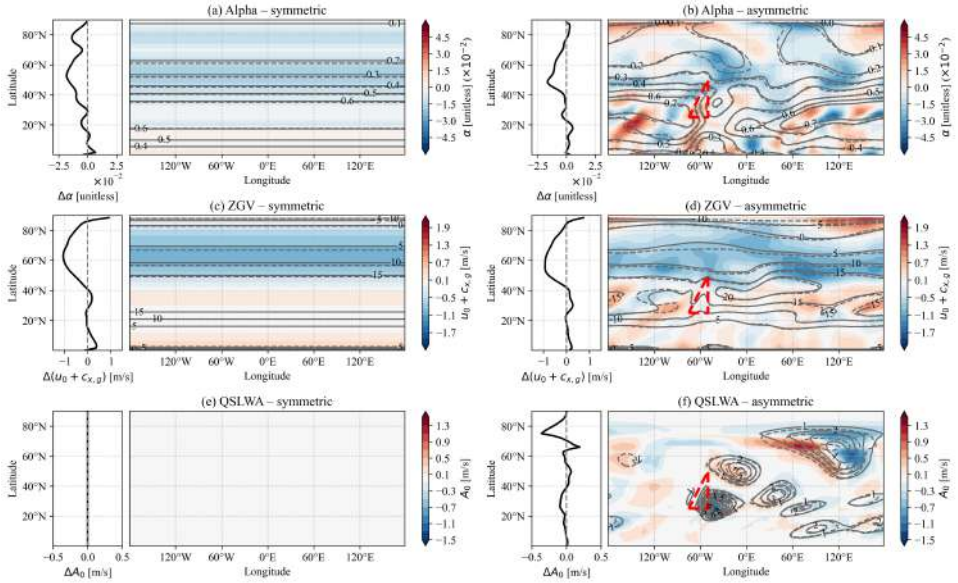

Figure 4.7: The Figure depicts the response of α (panels a,d), of the zonal Rossby wave group velocity (panels b,e) and of the quasi stationary local wave activity (panels c,f) to an AA-like forcing, in the SYM and ASYM simulations. Panels a-c-e-g refer to the SYM simulation, while panels b-d-f-h refer to the ASYM simulation. The shadings and the contours refer to the same experiments as in Fig. 4.5

capacity effectively lowers the threshold for blocking onset, allowing smaller LWA anomalies to trigger an event. On the contrary, the carrying capacity increase at lower latitudes has no impact on blocking frequency, as the absolute LWA remains well below the threshold required for onset in both the BASE SYM and AA SYM simulations.

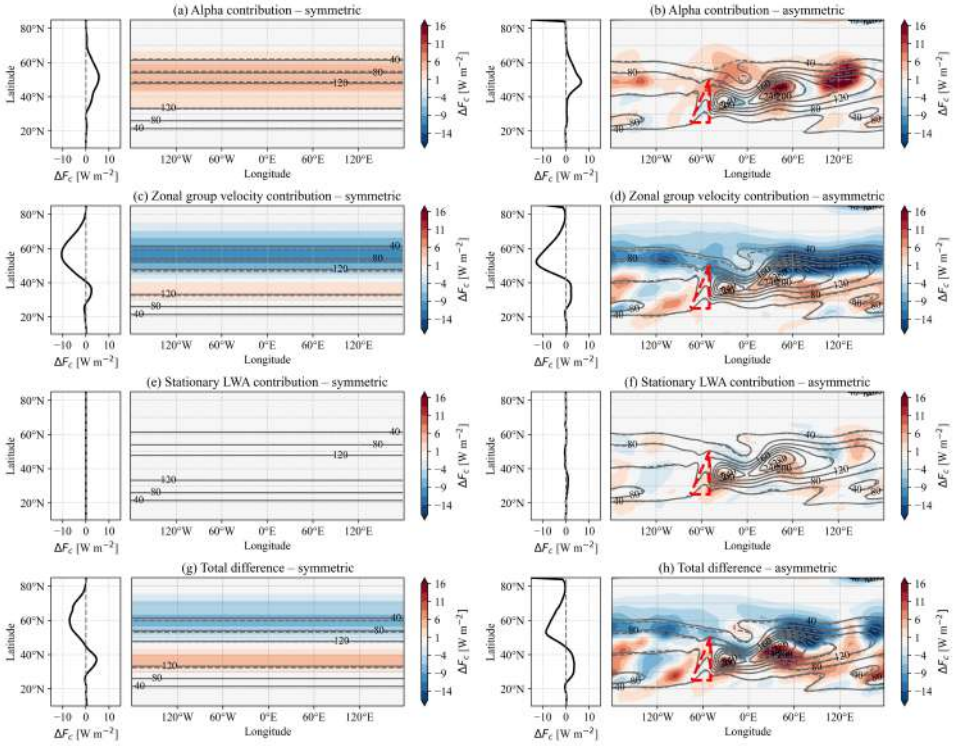

Figure 4.8: The Figure depicts the response of the carrying capacity to an AA-like forcing, in the SYM and ASYM simulations. Panels a-c-e-g refer to the SYM simulation, while panels b-d-f-h refer to the ASYM simulation. The response of carrying capacity is decomposed in various components: panel a and b show the contribution of the α parameter, panel c and d show the contribution of the doppler-shifted rossby waves group velocity, panel e and f show the contribution of stationary LWA and panel g and h show the total difference. For further explanations about the computation of these contributions see Section 4.2.4 . The shadings and the contours refer to the same experiments as in Fig. 4.5

Moving to the ASYM simulations (panels b–d–f–h), we find responses that are qualitatively consistent with those in the SYM simulations when zonally averaged. Once again, the midlatitudes exhibit a localized enhancement in carrying capacity associated with changes of α, while a reduction in carrying capacity emerges where the Doppler-shifted Rossby wave group velocity decreases. Notably, while the sign of the carrying capacity response due to α and the group velocity is approximately zonally symmetric,its magnitude varies with longitude. By comparison, the contri-

bution from stationary wave changes is relatively minor (panel f), especially when compared to the other components. The total response (panel h) closely resembles the symmetric case, characterized by an increase at lower latitudes and a decrease at higher latitudes. As in SYM, the dominant contribution comes from changes in zonal Rossby wave group velocity, in turn driven by changes in the mean zonal winds. Noticeable zonal asymmetries still emerge in the total carrying capacity response, mainly due to the asymmetries in the α contribution and the weak contribution from the stationary wave term. However, these asymmetries are not as pronounced as those found for the atmospheric blocking frequency response in Fig. 4.6f and are therefore not sufficient alone to explain the displacement of the blocking maximum.

In summary, despite the qualitative similarities between the carrying capacity responses in the two simulations, the resulting impact on atmospheric blocking is considerably different. In the SYM configuration, the reduction in carrying capacity leads to a uniform increase in blocking frequency. In contrast, the reduction seen in the ASYM simulations results in a longitudinal shift of the blocking frequency maximum. This behavior can be understood by considering the spatial structure of the carrying capacity in the ASYM experiments: blocking onset preferentially occurs downstream and poleward of the carrying capacity maximum. Therefore, when the maximum weakens—even in the hypothetical case of a zonally symmetric carrying capacity response—the region where blocking can develop is displaced upstream, shifting the blocking frequency maximum accordingly. In this way, qualitatively similar circulation changes can produce distinct blocking responses depending on the underlying symmetries of the model.

4.4 CONCLUSIONS

In this study, we investigate the response of atmospheric blocking to Arctic Amplification (AA) within the framework of the Traffic Jam Theory. The use of idealized aquaplanet simulations in both zonally symmetric and asymmetric configurations, allows us to isolate the role of zonal asymmetries and baseline circulation features in shaping the blocking response to AA.

We first show that experimental setup realistically reproduces key ingredients of midlatitude dynamics, namely storm tracks, LWA, and atmospheric blocking. Consistent with previous studies, blocking-like circulations emerge even in the absence of zonal asymmetries in the SYM simulations [28, 56]. The introduction of a localized storm track in the ASYM case leads to a spatial distribution of blocking that resembles observations in the Atlantic basin, validating the model's ability to capture essential processes governing blocking onset.

An important finding of this study is that despite similar large-scale circulation responses, manifest in comparable shits in zonally averaged LWA and TKE in both configurations, the resulting blocking response differs markedly. In the SYM configuration, AA leads to a relatively uniform increase in blocking frequency at high latitudes. In contrast, the ASYM configuration is characterized by a longitudi-

nal reorganization, where the dominant signal is an upstream shift of the blocking maximum.

We interpret these divergent changes in terms of changes in the carrying capacity. Under AA, the carrying capacity decreases at high latitudes and increases at mid-to-low latitudes, primarily as a consequence of changes in Rossby wave group velocity. While these carrying-capacity changes have similar characteristics in both configurations, their impact on blocking is dictated by the baseline climatological carrying capacity. In particular, in the ASYM case, the pre-existing spatial structure of the carrying capacity implies that a high-latitude decrease shifts the location where the conditions for blocking onset are met. This results in an upstream displacement, rather than a simple increase in frequency.

A key contribution of this study is the application of the Traffic Jam theory of blocking onset to the response of midlatitude circulation to AA. This framework is particularly useful for explaining how changes in the mean atmospheric circulation, local wave activity, stationary waves, and transient kinetic energy combine to shape the blocking response in a physically consistent manner. In particular, we find that the decrease in zonal winds is the primary driver of the high-latitude increase in atmospheric blocking, with the stationary wave playing a secondary role. Furthermore, we identify a novel negative feedback associated with a reduction in α, the correlation parameter between zonal winds and LWA. This reductions effectively buffers the decrease in carrying capacity, limiting the potential increase in blocking under AA. This mechanistic perspective, which accounts for several competing processes influencing blocking frequency under AA, provides a useful and unifying framework to contextualize and interpret previous studies that focus on different metrics related to Rossby wave characteristics, jet waviness, and midlatitude temperature extremes.

Furthemore, our results offer a physical explanation for the persistent intermodel spread in blocking projections. Specifically, our finding that the presence of a localized storm track fundamentally alters the response suggests that model biases in the mean-state carrying capacity can lead to considerably different blocking trends, even when the external forced changes in zonal winds, TKE and LWA are similar. This perspective provides further support to earlier arguments emphasizing the need to correct mean-state biases to improve the representation of blocking in climate models [65]. Our study provides a physical explanation for this sensitivity, demonstrating that the unperturbed position and structure of the carrying-capacity play a central role in determining how blocking responds to external forcings such as AA.

While our study focuses on how mean-state changes impact blocking occurrence, previous research has investigated the role of Rossby wave breaking in the circulation response to AA [27]. The relationship between mean atmospheric circulation and blocking is in fact twofold: the strength and position of the jet stream influence the location, frequency, and persistence of blocking events, while an increase in Rossby wave breaking—often associated with blocking occurrence [66–68, e.g.]—can decelerate the high-latitude flow. This creates a “chicken-and-egg”

problem, complicating the distinction between whether mean circulation changes drive blocking frequency modifications or vice versa. Sensitivity tests we have conducted by excluding blocked grid points in carrying capacity circulation changes show that our results remain qualitatively unchanged (not shown), supporting the conclusion that it is primarily the mean circulation that affects blocking frequency. Nevertheless, blocking changes can act as positive or negative feedback mechanisms on the mean wind response.

In conclusion, this study addresses several critical research gaps while simultaneously outlining promising directions for future work. For example, extending the carrying capacity framework to the ensemble of comprehensive climate model simulations contributing to PAMIP [13] would facilitate a more robust interpretation of model responses to Arctic warming in future projections. A similar analysis could be applied to the CMIP6 [69] archive to understand the broader effect of greenhouse gas forcing on blocking through our novel carrying capacity decomposition. However, these tasks pose significant challenges, primarily due to the difficulty of computing QGPV from datasets with relatively low vertical resolution, such as those available in the PAMIP and CMIP6 ensembles.

In addition, the sensitivity of the parameter α to external forcings deserves further investigation. In our simulations, α acts as a negative feedback that buffers the response of the carrying capacity under Arctic amplification; therefore, accurately quantifying its sensitivity is of primary importance for predicting future blocking frequency changes. In the Supplementary Material we show how this change may be related to changes in the midlatitude wave-guide and meridional wind shear. Yet, the response of α to Arctic amplification remains underexplored, particularly when compared with the extensive literature on changes in mean zonal winds or stationary waves. Addressing this gap is essential to improve our understanding of the nonlinear response of temperature extremes to Arctic amplification and, more broadly, to anthropogenic global warming.

4.5 SUPPLEMENTARY MATERIAL

We analyze the mechanisms responsible for the decrease of

$$\alpha = -\frac{u_e A^T}{AA^T}, \tag{4.22}$$

in the SYM simulations by decomposing its response to the Arctic forcing into two distinct contributions: (i) changes in the variance of LWA, AA^T (hereafter just 'variance') , and (ii) changes in the covariance between LWA and the zonal wind with reversed sign, $-u_e A^T$ (hereafter just 'negative covariance'). Let the subscript 'r' denote the reference (unforced) value and the subscript 'p' its response to the forcing. Writing

$$\alpha = \frac{C}{V}, \quad \text{with} \quad C \equiv -u_e A^T, \quad V \equiv AA^T,$$

the variation of α can be rewritten as:

$$\Delta\alpha = \left(\underbrace{\frac{C_p - C_r}{V_p}}_{\text{negative covariance contribution}} + \underbrace{C_r \left(\frac{1}{V_p} - \frac{1}{V_r} \right)}_{\text{variance contribution}} \right), \tag{4.23}$$

This decomposition allows us to isolate whether the weakening of α is primarily driven by modifications in the amplitude of LWA fluctuations or by changes in their dynamical coupling with the mean flow.

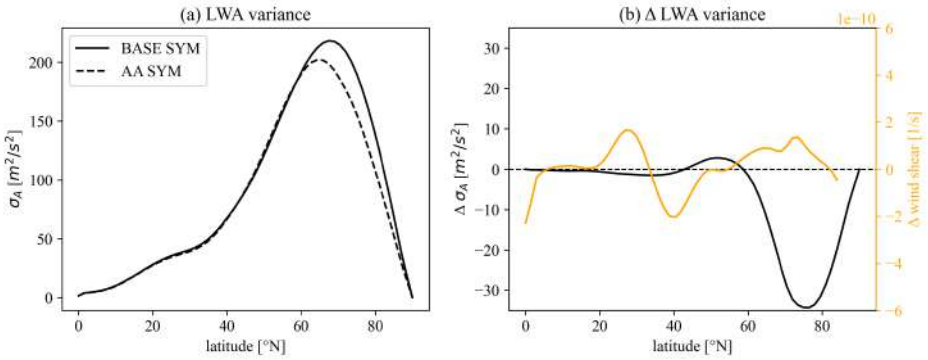

Figure S4.1: (a) LWA variance as a function of latitude for the reference and Arctic-amplified simulations. (b) Response of LWA variance (black) and zonal wind shear (orange) to Arctic warming.

We start by analyzing separately changes of variance and negative covariance. The response of variance exhibits a meridional dependence (Fig. S4.1). At high latitudes, the variance decreases, while at mid latitudes it slightly increases. We propose an interpretation of these differences based on changes of the meridional wind shear. Earlier literature highlighted how the jet stream can act as a wave guide [60–63]: waves propagate preferentially in regions of low wind shear, near the jet core, while in regions of strong shear, poleward and equatorward of the jet, they tend to break because of the wave straining mechanism and the growing importance of non-linear terms of the vorticity equation [70, 71]. We therefore expect changes of wind shear to affect the variance, which depends strongly on the presence and propagation of synoptic eddies. Fig. S4.1b shows changes in both wind shear and variance, highlighting how they are negatively correlated. An offset exists between the two, which may be linked to the general decrease of baroclinicity found from mid to high latitudes, depicted by Figure 4.6 in the main text, or to the overall wind speed decrease at mid-to-high latitudes that decreases the zonal flux of LWA. On a final note, we underscore how the wind shear characteristics and the wave-guide modifications mostly affect the variance, rather than the mean LWA. In fact, the variance is strongly related to the zonal advection of Rossby waves, showing

similar features to the LWA zonal flux (not shown), while the LWA mean embeds several scales of temporal variability.

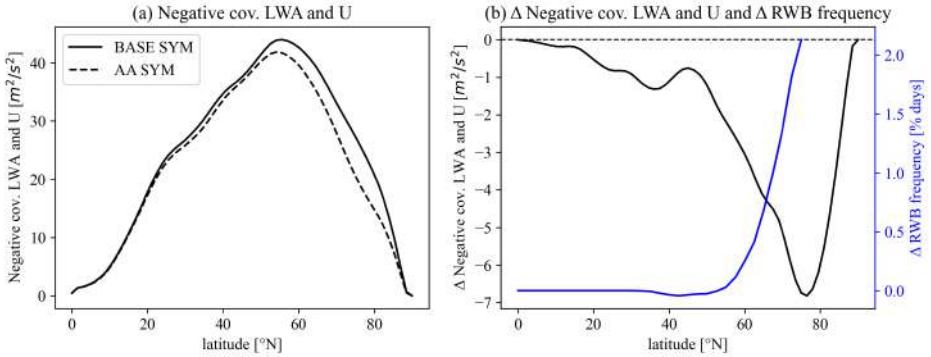

Figure S4.2: (a) Negative covariance between LWA and zonal wind in the BASE SYM and AA SYM simulations. (b) Latitudinal changes in negative covariance (black) and Rossby wave breaking (RWB) frequency (blue) under Arctic warming.

Moving to changes of negative covariance (Figure S4.2), we find differences concentrated at high latitudes, where a substantial reduction is observed. We speculate that this decrease is again linked wind shear differences, which act to increase the frequency of Rossby wave breaking (RWB) at high latitudes. As described in the main text, when the LWA flux surpasses the maximum carrying capacity—which at high latitudes is rather low—RWB occurs and zonal winds are deflected, while LWA keeps accumulating. In this regime, the relationship between zonal winds and LWA changes and the negative covariance decreases. Figure S4.2b compares changes of negative covariance with changes of RWB frequency under Arctic warming, computed thanks to the index introduced by Davini *et al.* [68], which looks for the reversal of the meridional gradient of geopotential height at 500 hPa (refer to the original manuscript for additional details). We underscore that RWB events detected by the Davini index are quite different from the blocking events detected through our method based on LWA anomalies, adopted in the main text. The reversal of the geopotential height gradient does not necessarily lead to LWA anomalies large enough to be detected as blocking events by our method. In fact, events detected by the Davini index are concentrated at high latitudes and their frequency distribution is considerably different from that of our LWA anomaly-based index, with almost no overlaps (not shown). As already reported by Ronalds & Barnes [27], RWB at highlatitudes increases following Arctic warming. While these results support our interpretation, they do not prove a causal relationship between changes of RWB frequency and LWA and eddy wind negative covariance. A more thorough assessment of causal relationships is left for future work.

Fig. S4.3 therefore shows the decomposition terms described in Eq. 4.23. At midlatitudes, the increase of variance and changes of negative covariance act in

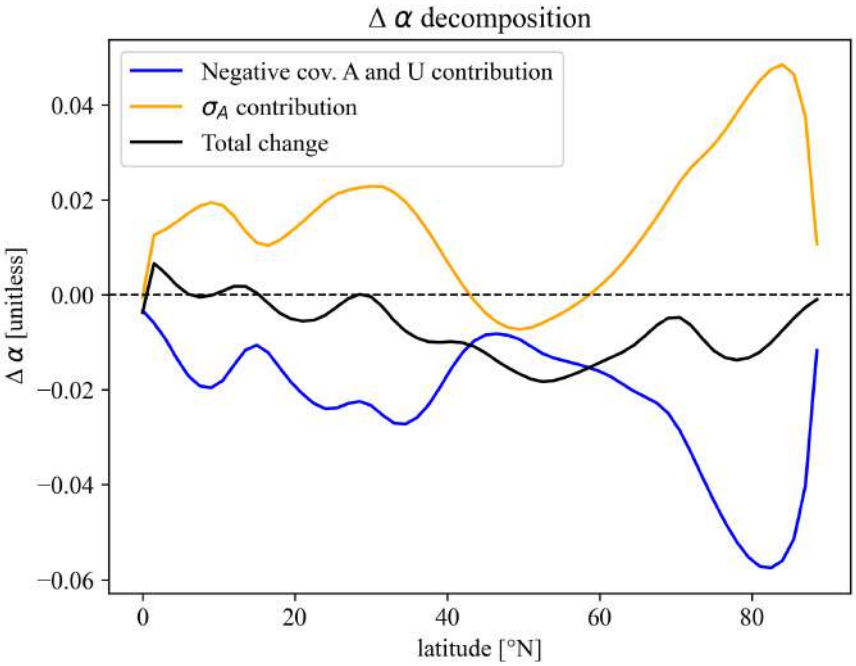

Figure S4.3: Decomposition of the response of α to Arctic warming in the SYM simulations. The physical meaning of each line is reported in the legend and additional information on each term of the decomposition is found in the text.

the same direction, leading to a decrease of α. On the contrary, at high latitudes the reduction of variance and the strong decrease of negative covariance act in opposite directions, resulting in a small decrease of α. The same happens at low latitudes. This compensation means that the impact of changes of Rossby wave breaking occurrence at high-latitudes is reduced, while the narrowing of the mid-latitude wave-guide acquire a greater relative importance.

Summarizing, we conclude that changes in the meridional shear of zonal winds lead to a small but significant decrease of alpha, slightly increasing the carrying capacity of the flow, as shown in the main text. These differences most likely arise from changes of the meridional shear of zonal winds, which act to narrow the mid-latitudes wave guide and to increase the probability of Rossby wave breaking at high latitudes. The same analysis has been performed for the ASYM simulations, showing qualitatively similar results (not shown).

REFERENCES

1. IPCC. *Climate Change 2023: Synthesis Report. Contribution of Working Groups I, II and III to the Sixth Assessment Report of the Intergovernmental Panel on Climate Change* (eds Lee, H. & Romero, J.) 35–115. doi:10.59327/IPCC/AR6-9789291691647 (IPCC, Geneva, Switzerland, 2023).

2. Screen, J. A. & Simmonds, I. The central role of diminishing sea ice in recent Arctic temperature amplification. *Nature* **464,** 1334–1337. doi:https://doi.org/10.1038/nature09051 (2010).

3. Previdi, M. *et al.* Arctic amplification of climate change: a review of underlying mechanisms. *Environmental Research Letters* **16,** 093003. doi:10.1088/1748-9326/ac1c29 (2021).

4. Caballero, R. & Merlis, T. M. Polar Feedbacks in Clear-Sky Radiative–Advective Equilibrium from an Airmass Transformation Perspective. *Journal of Climate* **38,** 3399–3416. doi:https://doi.org/10.1175/JCLI-D-24-0031.1 (2025).

5. Francis, J. A. & Vavrus, S. J. Evidence linking Arctic amplification to extreme weather in mid-latitudes. *Geophysical research letters* **39.** doi:https://doi.org/10.1029/2012GL051000 (2012).

6. Barnes, E. A. Revisiting the evidence linking Arctic amplification to extreme weather in midlatitudes. *Geophysical research letters* **40,** 4734–4739. doi:https://doi.org/10.1002/grl.50880 (2013).

7. Screen, J. A. & Simmonds, I. Exploring links between Arctic amplification and mid-latitude weather. *Geophysical Research Letters* **40,** 959–964. doi:https://doi.org/10.1002/grl.50174 (2013).

8. Overland, J. E. A difficult Arctic science issue: Midlatitude weather linkages. *Polar Science* **10,** 210–216 (2016).

9. Blackport, R. & Screen, J. A. Insignificant effect of Arctic amplification on the amplitude of midlatitude atmospheric waves. *Science Advances* **6,** eaay2880. doi:10.1126/sciadv.aay2880 (2020).

10. Geen, R. *et al.* An explanation for the metric dependence of the midlatitude jet-waviness change in response to polar warming. *Geophysical Research Letters* **50,** e2023GL105132. doi:https://doi.org/10.1029/2023GL105132 (2023).

11. Cohen, J. *et al.* Divergent consensuses on Arctic amplification influence on midlatitude severe winter weather. *Nature Climate Change* **10,** 20–29. doi:https://doi.org/10.1038/s41558-019-0662-y (2020).

12. Blackport, R. *et al.* Models and observations agree on fewer and milder midlatitude cold extremes even over recent decades of rapid Arctic warming. *Science Advances* **10,** eadp1346. doi:DOI:10.1126/sciadv.adp1346 (2024).

13. Smith, D. M. *et al.* The Polar Amplification Model Intercomparison Project (PAMIP) contribution to CMIP6: investigating the causes and consequences of polar amplification. *Geoscientific Model Development* **12,** 1139–1163. doi:10.5194/gmd-12-1139-2019 (2019).

14. Smith, D. M. *et al.* Robust but weak winter atmospheric circulation response to future Arctic sea ice loss. *Nature communications* **13,** 727. doi:https://doi.org/10.1038/s41467-022-28283-y (2022).

15. Screen, J. A., Smith, D., *et al.* Net equatorward shift of the jet streams when the contribution from sea-ice loss is constrained by observed eddy feedback. *Geophysical Research Letters* **49,** e2022GL100523. doi:10.1029/2022GL100523 (2022).

16. Riebold, J. *et al.* On the linkage between future Arctic sea ice retreat, Euro-Atlantic circulation regimes and temperature extremes over Europe. *Weather and Climate Dynamics* **4,** 663–682. doi:https://doi.org/10.5194/wcd-4-663-2023 (2023).

17. Hay, S. *et al.* The impact of Arctic sea-ice loss on winter weather in the British Isles. *Quarterly Journal of the Royal Meteorological Society,* e70012. doi:https://doi.org/10.1002/qj.70012 (2025).

18. Zhuo, W. *et al.* The response of atmospheric blocking and East Asian cold extremes to future Arctic Sea ice loss. *Atmospheric Research* **304,** 107355. doi:https://doi.org/10.1016/j.atmosres.2024.107355 (2024).

19. Streffing, J. *et al.* Response of Northern Hemisphere weather and climate to Arctic sea ice decline: Resolution independence in Polar Amplification Model Intercomparison Project (PAMIP) simulations. *Journal of Climate* **34,** 8445–8457. doi:https://doi.org/10.1175/JCLI-D-19-1005.1 (2021).

20. Butler, A. H. *et al.* The steady-state atmospheric circulation response to climate change–like thermal forcings in a simple general circulation model. *Journal of Climate* **23,** 3474–3496. doi:https://doi.org/10.1175/2010JCLI3228.1 (2010).

21. Wu, Y. & Smith, K. L. Response of Northern Hemisphere midlatitude circulation to Arctic amplification in a simple atmospheric general circulation model. *Journal of Climate* **29,** 2041–2058. doi:https://doi.org/10.1175/JCLI-D-15-0602.1 (2016).

22. Mudhar, R. *et al.* Exploring mechanisms for model-dependency of the stratospheric response to Arctic warming. *Journal of Geophysical Research: Atmospheres* **129,** e2023JD040416. doi:https://doi.org/10.1029/2023JD040416 (2024).

23. Shaw, T. A. & Smith, Z. The midlatitude response to polar sea ice loss: Idealized slab-ocean aquaplanet experiments with thermodynamic sea ice. *Journal of Climate* **35,** 2633–2649. doi:https://doi.org/10.1175/JCLI-D-21-0508.1 (2022).

24. Lewis, N. T. *et al.* Assessing the Spurious Impacts of Ice-Constraining Methods on the Climate Response to Sea Ice Loss Using an Idealized Aquaplanet GCM. *Journal of Climate* **37,** 6729–6750. doi:https://doi.org/10.1175/JCLI-D-24-0153.1 (2024).

25. Feldl, N. *et al.* Atmospheric eddies mediate lapse rate feedback and Arctic amplification. *Journal of Climate* **30,** 9213–9224. doi:https://doi.org/10.1175/JCLI-D-16-0706.1 (2017).

26. Yuval, J. & Kaspi, Y. Eddy activity response to global warming–like temperature changes. *Journal of Climate* **33,** 1381–1404. doi:https://doi.org/10.1175/JCLI-D-19-0190.1 (2020).

27. Ronalds, B. & Barnes, E. A. A role for barotropic Eddy–Mean flow feedbacks in the zonal wind response to sea ice loss and arctic amplification. *Journal of Climate* **32,** 7469–7481 (2019).

28. Hu, Y. *et al.* Blocking systems over an aqua planet. *Geophysical Research Letters* **35.** doi:https://doi.org/10.1029/2008GL035351 (2008).

29. Hassanzadeh, P. *et al.* Responses of midlatitude blocks and wave amplitude to changes in the meridional temperature gradient in an idealized dry GCM. *Geophysical Research Letters* **41,** 5223–5232. doi:https://doi.org/10.1002/2014GL060764 (2014).

30. Screen, J. A. *et al.* Reduced risk of North American cold extremes due to continued Arctic sea ice loss. *Bulletin of the American Meteorological Society* **96,** 1489–1503. doi:https://doi.org/10.1175/BAMS-D-14-00185.1 (2015).

31. Schneider, T. *et al.* Physics of changes in synoptic midlatitude temperature variability. *Journal of Climate* **28,** 2312–2331. doi:https://doi.org/10.1175/JCLI-D-14-00632.1 (2015).

32. Riboldi, J. *et al.* On the linkage between Rossby wave phase speed, atmospheric blocking, and Arctic amplification. *Geophysical Research Letters* **47,** e2020GL087796. doi:https://doi.org/10.1029/2020GL087796 (2020).

33. Cattiaux, J. *et al.* Sinuosity of midlatitude atmospheric flow in a warming world. *Geophysical Research Letters* **43,** 8259–8268. doi:https://doi.org/10.1002/2016GL070309 (2016).

34. Huang, C. S. & Nakamura, N. Local finite-amplitude wave activity as a diagnostic of anomalous weather events. *Journal of the Atmospheric Sciences* **73,** 211–229. doi:https://doi.org/10.1175/JAS-D-15-0194.1 (2016).

35. Francis, J. A. & Vavrus, S. J. Evidence for a wavier jet stream in response to rapid Arctic warming. *Environmental Research Letters* **10,** 014005. doi:10.1088/1748-9326/10/1/014005 (2015).

36. Nakamura, N. & Huang, C. S. Atmospheric blocking as a traffic jam in the jet stream. *Science* **361,** 42–47. doi:10.1126/science.aat0721 (2018).

37. Barpanda, P. & Nakamura, N. Local wave-activity analysis of atmospheric blocks in the Northern Hemisphere winter. *Journal of Climate.* doi:https://doi.org/10.1175/JCLI-D-24-0232.1 (2025).

38. Screen, J. A. *et al.* Causes and consequences of Arctic amplification elucidated by coordinated multimodel experiments. *Communications Earth & Environment.* doi:https://doi.org/10.1038/s43247-025-03052-z (2025).

39. Yan, X. *et al.* Traffic bottlenecks: Predicting atmospheric blocking with a diminishing flow capacity. *Geophysical Research Letters* **51,** e2024GL111035. doi:https://doi.org/10.1029/2024GL111035 (2024).

40. Vallis, G. K. *et al.* Isca, v1. 0: A framework for the global modelling of the atmospheres of Earth and other planets at varying levels of complexity. *Geoscientific Model Development* **11,** 843–859. doi:https://doi.org/10.5194/gmd-11-843-2018 (2018).

41. Kaspi, Y. & Schneider, T. The role of stationary eddies in shaping midlatitude storm tracks. *Journal of the atmospheric sciences* **70,** 2596–2613. doi:https://doi.org/10.1175/JAS-D-12-082.1 (2013).

42. Frierson, D. M. *et al.* A gray-radiation aquaplanet moist GCM. Part I: Static stability and eddy scale. *Journal of the atmospheric sciences* **63,** 2548–2566 (2006).

43. Merlis, T. M. *et al.* Hadley circulation response to orbital precession. Part I: Aquaplanets. *Journal of Climate* **26,** 740–753 (2013).

44. Betts, A. K. & Miller, M. J. in *The representation of cumulus convection in numerical models* 107–121 (Springer, 1993).

45. O'Gorman, P. A. & Schneider, T. The hydrological cycle over a wide range of climates simulated with an idealized GCM. *Journal of Climate* **21,** 3815–3832 (2008).

46. Nakamura, N. & Zhu, D. Finite-amplitude wave activity and diffusive flux of potential vorticity in eddy–mean flow interaction. *Journal of the atmospheric sciences* **67,** 2701–2716. doi:https://doi.org/10.1175/2010JAS3432.1 (2010).

47. Huang, C. S. *et al.* Falwa: Python Package to Implement Finite-Amplitude Local Wave Activity Diagnostics on Climate Data. *Geoscience Data Journal* **12,** e70006. doi:https://doi.org/10.1002/gdj3.70006 (2025).

48. Richards, P. I. Shock waves on the highway. *Operations research* **4,** 42–51. doi:https://doi.org/10.1287/opre.4.1.42 (1956).

49. Charney, J. G. & Drazin, P. G. Propagation of planetary-scale disturbances from the lower into the upper atmosphere. *Journal of Geophysical Research* **66,** 83–109. doi:https://doi.org/10.1029/JZ066i001p00083 (1961).

50. Dole, R. M. & Gordon, N. D. Persistent anomalies of the extratropical Northern Hemisphere wintertime circulation: Geographical distribution and regional persistence characteristics. *Monthly Weather Review* **111,** 1567–1586. doi:https://doi.org/10.1175/1520-0493(1983)111<1567:PAOTEN>2.0.CO;2 (1983).

51. Filippucci, M. *et al.* Impact of stochastic physics on the representation of atmospheric blocking in EC-Earth3. *Weather and Climate Dynamics* **5,** 1207–1222. doi:10.5194/wcd-5-1207-2024 (2024).

52. Woollings, T. *et al.* Blocking and its response to climate change. *Current climate change reports* **4,** 287–300. doi:https://doi.org/10.1007/s40641-018-0108-z (2018).

53. Shaw, T. *et al.* Storm track processes and the opposing influences of climate change. *Nature Geoscience* **9,** 656–664. doi:https://doi.org/10.1038/ngeo2783 (2016).

54. Held, I. M. *et al.* Northern winter stationary waves: Theory and modeling. *Journal of climate* **15,** 2125–2144. doi:https://doi.org/10.1175/1520-0442(2002)015<2125:NWSWTA>2.0.CO;2 (2002).

55. Narinesingh, V. *et al.* Atmospheric blocking: The impact of topography in an idealized general circulation model. *Weather and Climate Dynamics Discussions* **2020,** 1–39. doi:https://doi.org/10.5194/wcd-1-293-2020 (2020).

56. Jiménez-Esteve, B. & Domeisen, D. I. The role of atmospheric dynamics and large-scale topography in driving heatwaves. *Quarterly Journal of the Royal Meteorological Society* **148,** 2344–2367. doi:https://doi.org/10.1002/qj.4306 (2022).

57. Sousa, P. M. *et al.* European temperature responses to blocking and ridge regional patterns. *Climate Dynamics* **50,** 457–477. doi:https://doi.org/10.1007/s00382-017-3620-2 (2018).

58. Lorenz, D. J. & Hartmann, D. L. Eddy–zonal flow feedback in the Southern Hemisphere. *Journal of the atmospheric sciences* **58,** 3312–3327. doi:https://doi.org/10.1175/1520-0469(2001)058<3312:EZFFIT>2.0.CO;2 (2001).

59. Andrews, D. G. *et al. Middle atmosphere dynamics* (Academic press, 1987).

60. Platzman, G. W. The Rossby wave. *Quarterly Journal of the Royal Meteorological Society* **94,** 225–248 (1968).

61. Swanson, K. L. *et al.* Dynamics of barotropic storm tracks. *Journal of the atmospheric sciences* **54,** 791–810 (1997).

62. Schwierz, C. *et al.* Forced waves on a zonally aligned jet stream. *Journal of the atmospheric sciences* **61,** 73–87 (2004).

63. Martius, O. *et al.* Tropopause-level waveguides. *Journal of the Atmospheric Sciences* **67,** 866–879 (2010).

64. Nakamura, N. Large-Scale Eddy-Mean Flow Interaction in the Earth's Extratropical Atmosphere. *Annual Review of Fluid Mechanics* **56,** 349–377. doi:https://doi.org/10.1146/annurev-fluid-121021-035602 (2024).

65. Scaife, A. A. *et al.* Atmospheric blocking and mean biases in climate models. *Journal of Climate* **23,** 6143–6152. doi:https://doi.org/10.1175/2010JCLI3728.1 (2010).

66. Tibaldi, S. & Molteni, F. On the operational predictability of blocking. *Tellus A* **42,** 343–365. doi:https://doi.org/10.1034/j.1600-0870.1990.t01-2-00003.x (1990).

67. Scherrer, S. C. *et al.* Two-dimensional indices of atmospheric blocking and their statistical relationship with winter climate patterns in the Euro-Atlantic region. *International journal of climatology* **26,** 233–250. doi:10.1002/joc.1250 (2006).

68. Davini, P. *et al.* Bidimensional diagnostics, variability, and trends of Northern Hemisphere blocking. *Journal of Climate* **25,** 6496–6509 (2012).

69. Eyring, V. *et al.* Overview of the Coupled Model Intercomparison Project Phase 6 (CMIP6) experimental design and organization. *Geoscientific Model Development* **9,** 1937–1958. doi:https://doi.org/10.5194/gmd-9-1937-2016 (2016).

70. Andrews, D. & McIntyre, M. Planetary waves in horizontal and vertical shear. *J. Atmos. Sci.* **33,** 2031–2048 (1976).

71. McIntyre, M. & Palmer, T. The surf zone in the stratosphere. *J. Atmos. Sci.* **40,** 189–208 (1983).

Chapter 5

Results summary and final discussion

5 RESULTS SUMMARY AND FINAL DISCUSSION

The three scientific papers presented here address the study of atmospheric blocking from different perspectives, ranging from the analysis of observations, to comprehensive climate model simulations, and to idealized experiments. For a clearer and more effective summary, in Section 1.5 we divided the research gaps identified in the literature review and addressed in the articles into three main categories, namely: (i) improving the representation of blocking in state-of-the-art climate models, (ii) adopting an effective theoretical framework for the analysis and interpretation of blocking, and (iii) identifying regional and global atmospheric blocking trends under anthropogenic global warming. In the next sections, we focus on each of these points, specifying how we contributed to addressing these research gaps.

5.1 IMPROVING BLOCKING REPRESENTATION IN STATE-OF-THE-ART CLIMATE MODELS

Although the modeling of blocking is a core element of all three publications presented here, it is in Chapter 2 that we attempt to provide guidance for improving the representation of blocking in a comprehensive climate model. Specifically, we investigate whether the implementation of two stochastic schemes can improve blocking representation by better capturing small-scale variability and its impact on the large-scale flow, at a low computational cost. Contrary to what hypothesized, we find that the two stochastic schemes, and in particular the SPPT scheme, have a small but detrimental effect on blocking representation, leading to moderately increased biases over Europe and the North Pacific.

By examining the details of this detrimental effect, we find that changes in blocking representation arise from changes in the mean midlatitude circulation, in particular from a strengthening of the eddy-driven jet stream. We decompose the meridional momentum transport into contributions from stationary eddies, transient eddies, and the meridional circulation to understand the causes of the modified momentum budget. We find that changes in the zonal momentum transport by equatorial stationary waves alter the strength of the midlatitude eddy-driven jet stream. This anomalous equatorial circulation arises from a Gill–Matsuno mechanism linked to increased cloud liquid water content in tropical clouds, which in turn results from an asymmetric effect of the SPPT scheme on water condensation. This process-based understanding of changes in blocking frequency therefore

provides useful information, pointing to tropical–midlatitude teleconnections and to the importance of water condensation processes for future developments of the SPPT parameterization.

Despite the other two research project were not specifically designed to improve the representation of blocking in a climate model, they still offer valuable insights for future model development. In Chapter 3, we analyze for the first time the representation of summer Greenland blocking from a Lagrangian perspective in a CMIP6 ensemble. Through this analysis, we reach the same conclusion as Maddison *et al.* [1], who highlighted that the CMIP6 ensemble underestimates summer Greenland blocking variability and fails to represent the recent increase observed in reanalyses. Moreover, we go beyond this perspective by separately analyzing blocking events originating east and west of Greenland, namely retrograding and upstream blocks, following an approach similar to that of Hauser *et al.* [2] for the ERA5 reanalysis. We find that models fail to represent the variability of upstream blocking and that such blocks are characterized by a stronger meridional transport of moisture. These results point to the importance of an accurate representation of moist processes for blocking amplification.

Finally, in Chapter 4, we highlight the importance of the mean atmospheric circulation in shaping the climatological frequency of atmospheric blocking. In contrast to Chapter 2, where we showed that a strengthened eddy-driven jet leads to decreased blocking frequency, here we show that a weaker and equatorward-displaced jet leads to increased blocking frequency, especially at mid-to-high latitudes. In doing so, we provide a solid theoretical interpretation of the mechanisms underlying these changes, using physically based arguments to show that an accurate representation of the time-averaged jet strength and position is fundamental for correctly modeling both the climatology of blocking and its response to external forcing.

5.2 Adopting effective theoretical frameworks in the analysis and interpretation of atmospheric blocking

Throughout the literature review, the Traffic Jam theory—introduced in recent years by Nakamura & Huang [3]—has been identified as a promising new theory for blocking onset. This theory explains how mean circulation characteristics interact nonlinearly with eddies, creating favorable conditions for blocking onset in specific regions of the Northern Hemisphere. The theory has been tested using reanalysis data by Barpanda & Nakamura [4] and Yan *et al.* [5], who showed that the carrying capacity is negatively correlated with atmospheric blocking frequency. Their results demonstrate that regions with smaller carrying capacity, such as the exit regions of the North Pacific and North Atlantic storm tracks, are more favorable for blocking onset. To our knowledge, no previous study has analyzed the response of the carrying capacity to external forcing in a moist general circulation model.

In Chapter 4, we therefore analyze the response of the flow carrying capacity to Arctic warming using a set of idealized moist aquaplanet experiments with a $1.5m$ deep mixed-layer ocean and diabatic surface heating applied in the polar region. We propose a novel decomposition of the carrying capacity response under external forcing, quantifying the contributions from changes in the Doppler-shifted Rossby wave group velocity, stationary wave phase and amplitude, and nonlinear eddy–mean flow interactions (parameterized by the parameter α). As discussed in the previous Section, we find that zonal winds play a primary role in shaping the carrying capacity and the blocking response by modifying the Rossby wave group velocity. In addition, we show that the parameter α decreases, acting as a negative feedback that limits the increase in blocking frequency under Arctic warming.

This approach proves useful by providing a clear mechanistic understanding of the link between changes in the mean circulation and changes in atmospheric blocking. It therefore supports a broader adoption of the Traffic Jam formalism in future blocking-related studies and in more comprehensive climate models.

5.3 IDENTIFYING REGIONAL AND GLOBAL ATMOSPHERIC BLOCKING TRENDS UNDER ANTHROPOGENIC GLOBAL WARMING

Regional and global future trends in atmospheric blocking constitute the third main focus of this collection of articles and are addressed in particular in Chapters 3 and 4.

Chapter 4 contributes to a broader understanding of hemispheric-scale trends. A central question in the study of anthropogenic global warming concerns the impact of changes in the meridional temperature gradient on midlatitude atmospheric circulation. On the one hand, lapse-rate feedback leads to enhanced warming in the upper tropical troposphere, strengthening the hemispheric meridional temperature gradient. On the other hand, Arctic amplification (AA)—the enhanced warming of polar regions primarily driven by sea-ice–albedo feedbacks—acts to weaken this gradient [6, 7, e.g.]. Recent modeling studies suggest a dominant role of tropospheric warming, although Arctic amplification may still contribute significantly [7]. For this reason, it remains important to assess the impact of Arctic amplification on midlatitude circulation, as its effects may still be present in the projected response to global warming, even if partially masked by tropospheric warming. As discussed in previous sections, Chapter 4 focuses specifically on this issue. Coordinated climate model experiments indicate that Arctic amplification weakens the jet stream by reducing the meridional temperature gradient [8]. Using idealized experiments, we further show that this jet weakening and its associated displacement increase blocking frequency by reducing the Doppler-shifted zonal group velocity of Rossby waves. Although our study is conducted in an idealized framework that may underestimate feedbacks arising from the complexity of the climate system, the theoretical framework adopted provides useful interpretations and methodologies that may be applied to more comprehensive models.

While hemispheric-scale projections generally indicate a decrease in Northern Hemisphere atmospheric blocking under anthropogenic global warming—especially in winter—[9–11] regional blocking trends may show opposite behavior. Greenland blocking provides a clear example, having increased at an unprecedented rate over the past decade [1, 12, 13], as discussed in Chapter 3. By decomposing the contributions of upstream and retrograding blocks to the recent trend, we show not only that the internal variability of upstream blocks is underestimated—as also discussed in Section 5.1—but also that projected trends differ substantially between the two blocking families. Specifically, retrograding blocks are projected to decrease, in line with hemispheric-scale trends, while upstream blocks are projected to remain unchanged or even increase, depending on the blocking index used.

5.4 Final discussion and open research questions

Although we have separated our results into three main categories, it is evident that these research topics are strongly interconnected. Without an effective and comprehensive theory of blocking onset, it remains difficult to improve blocking representation in state-of-the-art climate models. At the same time, new generations of climate models are the primary tools for assessing future changes in atmospheric circulation features such as blocking, and limited model skill hinders robust trend assessments. Moreover, climate models serve as numerical laboratories for testing theories of blocking onset, maintenance, and decay, while the validation of these theories also relies on model evidence. Finally, understanding how atmospheric blocking—an important driver of regional extremes—changes under global warming is a central goal of current research and provides motivation to further explore theories, observations, and model outputs, thereby closing the circle of interdependence among these research questions. It follows that studies of atmospheric blocking must consider all these aspects, if not to address broad research questions, then at least to place specific findings within the broader research context. In this Thesis, the investigation of different research questions naturally expanded toward related topics, leading to the use of a wide range of modeling and analysis tools. This diversity represents a clear strength of the work, allowing atmospheric blocking to be examined from multiple perspectives.

At the same time, by addressing many different topics, this work leaves several open questions that motivate future research. Idealized modeling could, for example, provide a valuable framework for better understanding the origin of upstream and retrograding Greenland blocks identified in Chapter 3. Carefully designed experiments could isolate the key dynamical ingredients of these two blocking types and test how different forcings affect their relative frequency. This could be achieved by designing experiments in which an idealized ice dome representing Greenland interacts with a jet stream that is artificially shifted poleward and equatorward. Such experiments could be conducted in both dry and moist atmospheres to assess the role of latent heat release in blocking amplification and trajectory.

Still within the context of idealized modeling, it would be interesting to extend

the experiments presented in Chapter 4 to explicitly impose tropospheric warming rather than Arctic warming. This would allow a direct comparison between the effects of upper-tropospheric warming and Arctic amplification and help determine whether their impacts combine linearly or nonlinearly. In the same framework, a deeper understanding of the role of nonlinear processes—particularly the parameter α involved in the carrying capacity computation—in modulating the blocking response to Arctic amplification remains an important and relatively understudied challenge.

Turning to more comprehensive models, it would be valuable to estimate the carrying capacity of the flow in CMIP6 simulations, compare it with that derived from ERA5 reanalysis, and assess the strengths and limitations of current model representations. Although this may be challenging due to the limited vertical resolution of many CMIP6 models, which make it difficult to reliably compute potential vorticity, such an analysis could provide useful insights into model biases in blocking representation.

Finally, with regard to the development of the EC-Earth climate model, as discussed in Chapter 2, a systematic investigation of the impact of the SPPT scheme on blocking representation—through targeted model retuning aimed at improving tropical precipitation—would be a valuable next step.

Overall, many questions remain open, and the study of atmospheric blocking continues to be an active and rapidly evolving field of research.

5.4.1 Note on the contribution to the United Nations Sustainable Development Goals—SDGs

The work presented in this thesis contributes to the objectives of the National PhD Programme in "Sustainable Development and Climate Change," which align with the United Nations Sustainable Development Goals (SDGs). By enhancing our understanding of how regional and global temporal extremes respond to anthropogenic global warming, this research supports SDG 13 (Climate Action) by informing policymakers and the public, raising awareness of climate change impacts, and fostering the development of effective adaptation strategies. Accurate projections of extremes are also critical for building resilient food supply chains, contributing to SDG 2 (Zero Hunger), and for designing strategies to protect public health in regions vulnerable to heat extremes, thereby supporting SDG 3 (Good Health and Well-Being). Furthermore, this work aims to advance the fundamental understanding of atmospheric circulation under anthropogenic forcing, providing essential boundary conditions for research and the development of adaptation strategies that can address additional SDGs.

REFERENCES

1. Maddison, J. *et al.* Missing increase in summer Greenland blocking in climate models. *Geophysical Research Letters* **51,** e2024GL108505. doi:10.1029/2024GL108505 (2024).
2. Hauser, S. *et al.* Life cycle dynamics of Greenland blocking from a potential vorticity perspective. *Weather and Climate Dynamics* **5,** 633–658. doi:10.5194/wcd-5-633-2024 (2024).
3. Nakamura, N. & Huang, C. S. Atmospheric blocking as a traffic jam in the jet stream. *Science* **361,** 42–47. doi:10.1126/science.aat0721 (2018).
4. Barpanda, P. & Nakamura, N. Local wave-activity analysis of atmospheric blocks in the Northern Hemisphere winter. *Journal of Climate.* doi:https://doi.org/10.1175/JCLI-D-24-0232.1 (2025).
5. Yan, X. *et al.* Traffic bottlenecks: Predicting atmospheric blocking with a diminishing flow capacity. *Geophysical Research Letters* **51,** e2024GL111035. doi:https://doi.org/10.1029/2024GL111035 (2024).
6. Cohen, J. *et al.* Divergent consensuses on Arctic amplification influence on midlatitude severe winter weather. *Nature Climate Change* **10,** 20–29. doi:https://doi.org/10.1038/s41558-019-0662-y (2020).
7. Shaw, T. A. *et al.* Emerging climate change signals in atmospheric circulation. *AGU Advances* **5,** e2024AV001297. doi:https://doi.org/10.1029/2024AV001297 (2024).
8. Smith, D. M. *et al.* Robust but weak winter atmospheric circulation response to future Arctic sea ice loss. *Nature communications* **13,** 727. doi:https://doi.org/10.1038/s41467-022-28283-y (2022).
9. Davini, P. & d'Andrea, F. From CMIP3 to CMIP6: Northern Hemisphere atmospheric blocking simulation in present and future climate. *Journal of Climate* **33,** 10021–10038. doi:https://doi.org/10.1175/JCLI-D-19-0862.1 (2020).
10. Dorrington, J. *et al.* CMIP6 models trend toward less persistent European blocking regimes in a warming climate. *Geophysical Research Letters* **49,** e2022GL100811. doi:https://doi.org/10.1029/2022GL100811 (2022).
11. Lohmann, R. *et al.* Northern Hemisphere atmospheric blocking in CMIP6 climate projections using a hybrid index. *Journal of Climate* **37,** 6605–6625. doi:https://doi.org/10.1175/JCLI-D-23-0589.1 (2024).
12. Hanna, E. *et al.* The influence of North Atlantic atmospheric and oceanic forcing effects on 1900–2010 Greenland summer climate and ice melt/runoff. *Int. J. Climatol* **33,** 862–880. doi:DOI:10.1002/joc.3475 (2013).

13. Hanna, E. *et al.* Greenland Blocking Index 1851–2015: a regional climate change signal. *International Journal of Climatology* **36,** 4847–4861. doi:https://doi.org/10.1002/joc.4673 (2016).